Exploring magicity around N = 32 & 34 in Z $\geq$ 20 isotopes via precision mass measurements and developments with the TITAN MR-TOF mass spectrometer

Eleanor Dunling

Doctor of Philosophy

University of York

Physics

February 2021

Abstract

The Nuclear Shell Model provided the first coherent description of the nucleus which accounted for a wide range of nuclear properties. The model originated from observations of particularly stable isotopes with certain numbers, known as 'magic numbers', of protons and neutrons. At the time it was developed, in the 1960s, observations were limited to naturally occurring, and therefore stable, isotopes. With the advent of radioactive beam facilities, new studies indicate that the magic numbers seem to evolve and model corrections are required.

In this thesis, the TITAN Multiple-Reflection Time-Of-Flight Mass Spectrometer (MR-TOF-MS) was employed to study 'new' magic numbers N=32,34 across a range of isotopic chains about the traditionally magic Z=20. This work includes a characterisation of the TITAN MR-TOF-MS and high-precision mass measurements of ^{54}Ca, ^{54,55}Sc, $^{54-56}$Ti, and $^{54-58}$V. Isotopes of neutron-rich Ca, Sc, Ti and V were produced at the TRIUMF-ISAC facility and transported to the TITAN facility for measurement.

The results show magicity at N=32 is at a maximum in ^{52}Ca, and the effects decrease with increasing Z across the isotopes measured, the effects are slightly weaker in ^{53}Sc, and cease between ^{54}Ti and ^{55}V. This evolution is dramatically different due to the new measurements of ^{54,55}Sc. The precision on the masses of all isotopes measured in the study is improved in comparison to the AME2016, and results include the first ever direct mass measurement of ^{58}V. The evolution of N=32,34 magicity is explored via these new high-precision mass measurements.

Contents

List of Tables

List of Figures

Acknowledgements

The work presented in this thesis is the result of a collaboration of many people: the TITAN Collaboration, TRIUMF's Target and Ion Source Operation Team, the Beam Delivery Group, and many other members of the TRIUMF team. Many of the techniques and technologies discussed in this thesis were developed by others, which are referenced as much as possible. Many discussions with collaborators has contributed to my understanding and has aided me in writing this thesis.

I did not anticipate that I would be spending the final year of my PhD writing my thesis during a global pandemic. This is been a very strange experience. I have found silver linings (mostly that everyone else is also miserable at home not having any fun, just like me), but the lack of human contact on which I thrive has been extremely isolating. I am thankful for everyone in my life who has made an effort to keep in regular contact during this time. It is impossible to express adequate thanks to each person who has helped me to get to this point, but here are a few mentions.

My greatest thanks to Alison Laird, Ania Kwiatkowski, Christian Diget, and Jens Dilling for their supervision. I was lucky enough to have several supervisors over the course of my PhD, all of whom helped me a generous amount. I am extremely grateful to all of you for your time and energy, especially for giving me feedback on my thesis. Thank you for your unwavering support and encouragement.

My warmest thanks to all the TITANs I have had the pleasure of working with, past and present. You are truly the most fun, lovely, and, of course, hard-working team. The data collection would not have been possible without the support of Abhilash Javaji, Andrew Jacobs, Ania Kwiatkowski, Brian Koote, Chris Izzo, Erich Leistenschneider, Ish Mukul, Ivan Miskun, Jens Lassen, Jon Ringuette, Keerthi Jayamanna, Kilian Dietrich, Marilena Lykiardopoulou, Mel Good, Pascal Reiter, Peter Kunz, Rane Simpson, Rio Weil, Roshani Silwal, Sam Porter, Stefan Paul, Tobias Murboeck, Yang Lan and Zach Hockenbery. I cannot express enough gratitude to Pascal for all of your guidance, encouragement and mentorship. Specific thanks for your help in forming Chapter 4. Thanks to the other members of the MR-TOF team: Andrew and Tobias, for being wonderful people to work with, and for sharing the 12 hour shifts! Thanks to Erich for your camaraderie. Thank you Bruno for your generosity and kindness. Brian and Roshani - thank you for providing (in equal parts) physics conversation and comic relief.

Thank you to each person who has supported me academically during my PhD and prior, especially Stephanie Lyons Blyth my inspiration and mentor, Stuart Lyon my high school physics teacher, and my parents. To my family across the ocean: thank you for your encouragement, support and love. I will never forget the generosity and kindness given by Duncan & Katherine Ross, and Wayne & Julie Johnson, thank you for making it possible for me to do this PhD. Thank you to the most wonderful group of women for your never-ending reas-

surance, love, and hilarity for the past 20 years, and for the next 20, and the 20 after that... Extra thanks to Em and Jordanna for being the best friends I could wish for - always on the end of the phone for any kind of celebration or meltdown. Thanks a million to my gang of pals in Vancouver for making sure I spend enough time in the mountains, and for filling the past 4 years with so much fun, adventure and laughter. Thanks to all of the wonderful housemates I have had the pleasure of living with in the blue house. Finally, to Simone: I am proud of you, and I hope you are proud too.

Declaration

I declare that the work presented in this thesis, except contributions made clear by references or in the acknowledgements, is based on my own research. This work has not previously been presented for an award at this, or any other, University. Some of the data from Chapter 5 of this thesis has already been published as part of the following publications:

- M. P. Reiter, S. Ayet San Andrés, E. Dunling *et al.*, *"Quenching of the N=32 neutron shell closure studied via precision mass measurements of neutron-rich vanadium isotopes"*, Phys. Rev. C 98 (2018) 024310.
- E. Leistenschneider, E. Dunling *et al.*, *"Precision mass measurements of neutron-rich scandium isotopes refine the evolution of $N = 32$ and $N = 34$ shell closures"*, Phys. Rev. Lett. 126, (2021) 042501.

Chapter 1

Introduction

The nucleus of an atom is formed of protons and neutrons, collectively known as nucleons. All isotopes can be classified on the chart of nuclides, shown in figure 1.1, according to their proton number (Z) and neutron number (N). Z defines the different chemical elements, and N defines the different isotopes for a given element. The isotopes in figure 1.1 in darker grey squares are 'stable' isotopes (they do not spontaneously radioactively decay or their determined nuclear half-life exceeds the Earth's age) which form what is known as the 'valley of stability'. The valley of stability follows Z=N until approximately Z=20, after which point it veers towards heavier N (more neutrons in the nucleus), referred to as more 'neutron-rich' nuclei. At this point more neutral nucleons are required to keep the nucleus bound by buffering the repelling effects due to the Coulomb force between the positively charged protons in the nucleus. The Coulomb force repulses protons from one another, and has infinite range. The strong (nuclear) force binds the nucleus and is stronger than the repulsive Coulomb force, but has an effective range only within the nucleus ($\sim$1 fm).

Within the nucleus there is an internal nuclear structure of protons and neutrons, similar to the electron structure in an atom. The atomic shell model is used to describe the structure of orbital electrons about the nucleus where electrons fill discrete energy levels to form closed shells. At specific numbers of electrons the ionisation energy is particularly high. A similar hypothesis can be applied to the nucleus of the atom: the nuclear shell model [2]. The closed shells form at empirical 'magic numbers': 2, 8, 20, 28, 50, 82 and 126. At magic numbers of protons and neutrons closed nuclear shells form where the energy required to separate a proton or neutron from the nucleus is particularly high. These magic numbers are true for isotopes which are in and close to the valley of stability. However, in isotopes located far from the valley of stability (known as 'exotic', and defined by a large N/Z asymmetry) these magic numbers have been observed to disappear [3] and 'new' magic numbers to appear [4] which has stimulated investigations to understand the evolution from the original shell behaviour. Magic numbers become fickle far from stability due to the large imbalance between the protons and neutrons and the complex interactions between the nucleons within the nucleus, as discussed in [5]. Figure 1.1 shows the empirical magic numbers marked at 2, 8, 20, 28, 50, 82, and 126, and also indicates where shell features have been observed outside these traditional magic numbers.

The nucleons outside the closed shells (valence nucleons) govern the properties of the nucleus, much the same as valence electrons govern the properties of the atom. These properties include the energy of the excited states of the nucleus, nuclear charge radii, half-life

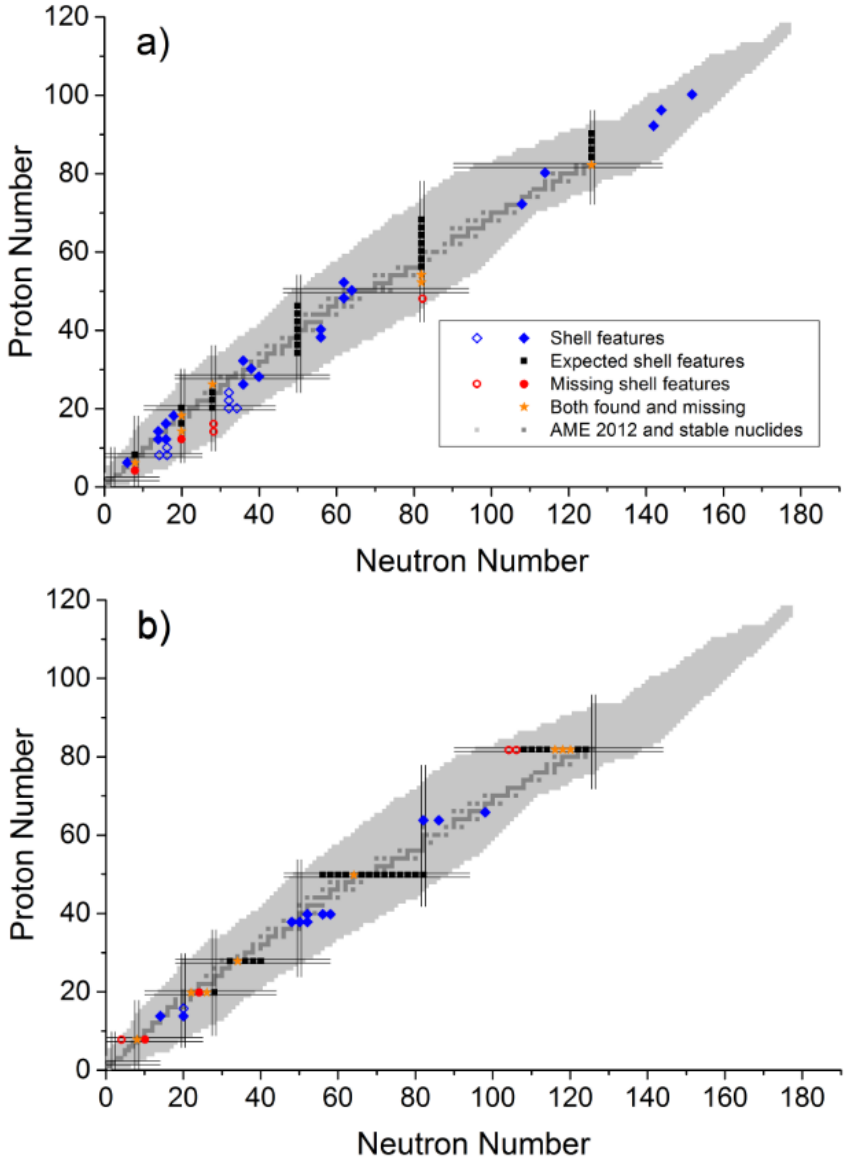

Figure 1.1: Features in the neutron (a) and proton (b) shells derived from nuclear properties. Blue diamonds label unexpected shell effects, black squares label expected shell effects, red circles indicate a lack of shell features. Orange stars indicate mixed findings. More details are found in the original figure, taken from [1].

in radioactive nuclei and the energy required to separate a nucleon from the nucleus. From measuring these properties, evidence for nuclear shell effects can be studied, thus revealing the nuclear structure related to the shells of the nucleus.

The energy of the first excited state in an even-even nucleus (even Z and N) is typically high at a magic number [1]; a greater energy is required to promote a magic nucleus (nucleus with a magic number of protons or neutrons) to an excited state. Figure 1.2 from [5] shows the classic magic numbers (top) and 'new' magic numbers (bottom) from studies of the first excitation energy. Energies of excited nuclear states can be measured via γ-ray spectroscopy.

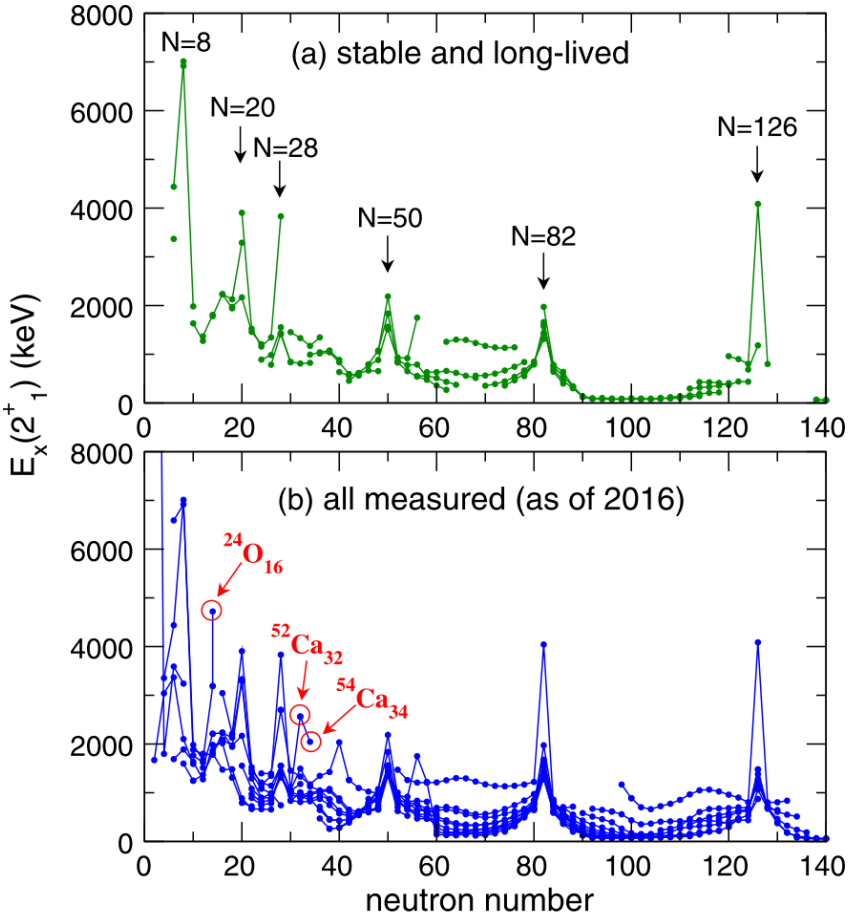

Figure 1.2: Excitation energy of the first 2+ state in even-even nuclei for stable and long-lived species (a) and of all nuclei as of 2016 (b), as a function of neutron number for many isotopic chains. Empirical magic numbers are demonstrated in (a), but more features are seen in (b) around 'new' magic numbers. Figure taken from [5].

Nuclear charge radii can be explored via the 'mean-square charge radius' (which is not a direct observable, but can be extracted from experimental findings) due to the charge density distribution in the nucleus. Closed shell effects are observed by a sharp rise in the mean-square charge radius when one additional nucleon is added beyond the closed shell [1]. The nucleon binding at a closed shell is particularly 'strong' and this leads to the assumption of a tightly arranged spherical configuration, where the protons are close together. This in turn would be reflected in a smaller charge radius. With an additional nucleon added beyond the magic number, the charge (and matter) radius increases as the valence nucleon is less bound outside the closed shell. Nuclear charge radii can be studied via laser spectroscopy [6].

Exotic nuclei are often referred to as 'short-lived' due to their short half-lives. Magic nuclei are more bound than their neighbours and this can manifest in an increased half-life. The half-life of an isotope can be measured via decay spectroscopy.

At closed shells, the nucleus can be described as more bound; it requires more energy to separate a proton or neutron from the nucleus than in neighbouring isotopes, thus allowing

identification of where nuclear magic numbers exist. As nucleons are added to the nucleus, the separation energy decreases as a trend overall, however there are deviations within the trend. For example, after a closed shell the separation energy has a more significant drop. This is evidence of closed shell behaviour and indicative of magic nuclei being more stable in comparison to neighbouring isotopes. High-precision mass measurements enable the measurement of the proton or neutron separation energy [7] and, when coupled to a source of radioactive ions for example a RIB facility, is a direct method to study these nuclear phenomena in exotic species.

The binding energy of a nucleus is the cumulation of all interactions between the nucleons. From $E = mc^2$ it is known that energy can be equated to mass. The binding energy is calculated from the difference in mass from the nucleus as a whole and its protons and neutrons. Thus, it is the energy required to break the nucleus into individual nucleons. The single nucleon separation energy, the energy required to remove a single nucleon from the nucleus, oscillates with odd and even Z and N, where nuclei with an even number of protons or neutrons have a higher separation energy (and are more bound). Even–even nuclei are more stable than odd–odd due to their unpaired nucleon. By studying the two-neutron (or two-proton) separation energy (S_{2N}), that is the energy required to release two neutrons from the nucleus, this disparity is avoided. S_{2N} is defined by equation 1.1 where $M(Z, N)$ is a nucleus with Z protons and N neutrons, m_n is the mass of a neutron and c is the speed of light.

$$S_{2N} = [M(Z, N-2) - M(Z, N) + 2m_n]c^2 \tag{1.1}$$

This gives a quantifiable measurement to interpret nuclear stability while avoiding odd-even pairing effects. Figure 1.3 from [8] shows the S_{2N} with increasing neutron number for many isotopic chains. Particular features can be seen to demonstrate nuclear shell closures, for example, beyond N=28 the S_{2N} decreases rapidly in many isotope chains indicating a global reduction in binding energy after the well-known shell closure. A similar but local effect can be seen around N=32 in Ca and Sc.

The evolution of the traditional magic numbers is of particular interest around N=32,34, between the N=28 and 50 shells, around magic Z=20. 'New' subshells at N=32,34 have been most prominently observed in Ca isotopes with magic proton number Z=20. Studies have extended into neighbouring isotope chains in order to map the progression of these shells in this region. Evidence for magicity has been seen in decay-spectroscopy data and mass measurement data, but curiously this is not reflected in charge radii data.

First descriptions of the N=32 subshell arose from β-decay studies of ^{53}K, ^{52}Ca, and ^{53}Sc [9]. This was followed by TOFI mass measurements observing increased binding at N=32 [10–12]. Decay-spectroscopy studies at NSCL expanded into Sc, Ti, V, and Cr isotopes, and provided further evidence for a subshell at N=32, and suggested a subshell at N=34 in ^{54}Ca [13–16]. Alongside these experimental results, theorists predicted shell closures in Ca at N=32 and N=34, explained due to the increasing N-Z imbalance causing the pf-shell interactions in this region [17]. Penning trap mass measurements, to complement the decay-spectroscopy studies, were performed on Cr isotopes which indicated a sub-shell closure at N=32 [18]. Systematic studies of the half-lives of neutron-rich Ca isotopes contributed further evidence to the presence of a subshell gap at N=32 [19]. β-decay studies of Ca, Sc, and Ti isotopes around N=32 provided yet more evidence for the existence of the subshell in Ca isotopes [20].

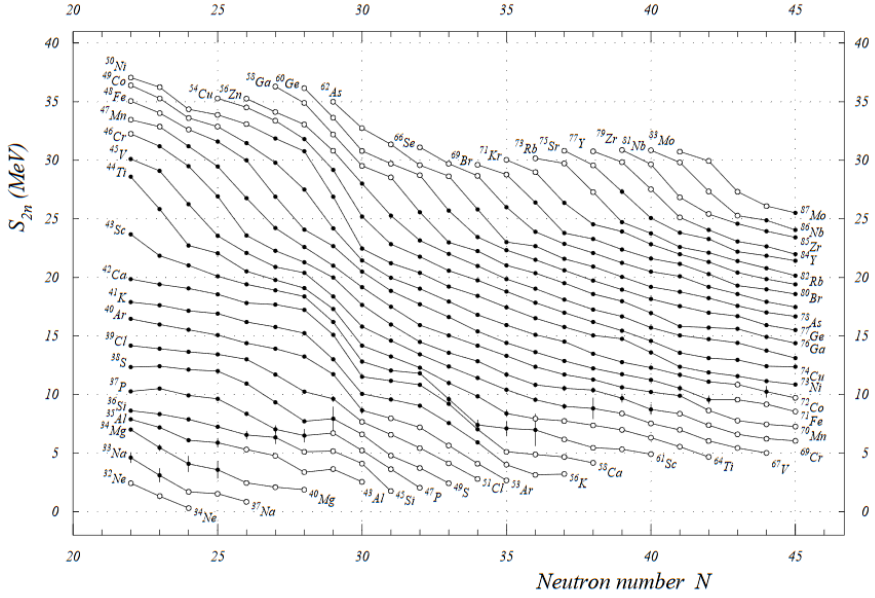

Figure 1.3: Two-neutron separation energy (S_{2N}) for increasing neutron number for isotopic chains 10≥Z≥42. The expected N=28 shell closure manifests as a kink in the slope and can be observed for nearly all species shown. In comparison a similar sudden drop at N=32,34 is unexpected and restricted to the neighbourhood of ^{52,54}Ca. Figure taken from [8].

Meanwhile the conclusion of the theoretically predicted subshell closure at N=34 was unclear [18, 20–22].

In the past decade, TITAN mass spectrometry up to N=32 identified ^{52}Ca to be significantly more bound than previously determined, and directly identified this doubly magic nuclei [3]. This was subsequently confirmed at ISOLTRAP [4]. Decay-spectroscopy measurements of ^{54}Ca at RIKEN identified N=34 shell effects in ^{54}Ca, though of a lower magnitude than in ^{52}Ca [23], later supported by mass measurement results [24]. In neighbouring chains, mass measurement results and γ-ray studies support the persistence of the N=32 subshell into Ar, K and Sc isotopes [25–27], and the N=34 subshell closure in Ar and Sc [27, 28]. Converse to the decay-spectroscopy and mass measurement data, the charge radii of ^{52}Ca measured at ISOLDE was found to be "much larger than expected for a doubly magic nucleus" [29]. The TITAN investigation into the region beyond the N=28 shell closure in nuclei far from stability continued in 2017 via the study of neutron-rich $^{51-55}$Ti and $^{52-55}$V isotopes across the N=32 shell closure [30, 31] utilising the established TITAN measurement Penning trap and demonstrating the TITAN MR-TOF-MS as a trusted mass measurement device. The results, as well as significantly reducing uncertainties on the mass values, identified weak shell effects in Ti isotopes and complete quenching of shell effects in V isotopes.

In this thesis, systematic mass measurements of Ca, Sc, Ti and V isotopes across the N=32,34 shell closures are presented to map the evolution of magicity with increasing proton number. Ca is proton magic, with Z=20, and hence an anchor point from which these studies originate. As protons are added, the forces between the nucleons changes and the N=32,34 shell closures evolve. High-precision mass measurement results around Z ≤ 20 were collected at the TITAN facility, using the TITAN MR-TOF-MS. The TITAN MR-TOF-MS,

commissioned in 2017, is characterised in the thesis, including an analysis of systematic errors which contribute to all TITAN MR-TOF-MS measurements. This evaluation of errors is utilised in the analysis of high-precision mass measurements of isotopes of Ca, Sc, Ti, and V. The mass measurement results are complimented by half-life measurements of $^{51-54}$Ti isotopes collected via decay spectroscopy at the ISAC Yield Station. The results presented in this work combine to provide a multifaceted picture of the N=32 shell closure, and extend beyond N=34, in the Z $\leq$ 20 region, and provide motivation for both experimental and theoretical developments to better understand the complex forces between nucleons, and their evolution at the extremities of the nuclear chart.

Chapter 2

Background to Experimental Methods

To study the nuclear properties which are exhibited by magic nuclei, access to radioactive ions is required. Nuclei far from the valley of stability, with a great imbalance of protons to neutrons, described as the most exotic nuclei, are the most difficult to produce and the most interesting to study due to their rarity and the unusual effects which do not occur in stable nuclei. Moreover, the extreme proton-to-neutron ratio represents a 'stress test' of theoretical predictions in extreme environments. Experimentally, these species have the shortest half-lives (down to ns and below) which makes performing measurements on them more challenging due to the short time window before their decay. It is a technical requirement to get these isotopes from production to the measurement facility fast enough, compared to their specific nuclear half-life. Moreover, these nuclei tend to have the lowest production rates due to reduced production cross-sections and suffer the most from contamination due to increased production yields of isobars closer to stability.

2.1 Radioactive Ion Beam (RIB) production

To perform measurements on radionuclides a radioactive ion beam (RIB) is required. There are two main methods for RIB production: the in-flight method and the isotope separation on-line (ISOL) method [32], both shown in figure 2.1.

The in-flight method

The in-flight method projects a heavy ion beam (up to U) onto a thin target at high energy (∼100 MeV to 1 GeV). Due to the heavy ion beam at high energy, the reaction products are liberated from the target and are carried forwards. Consequentially, they are separated while in flight (hence the name 'in-flight'). Due to the high beam energy the products are projected forward from the target in an ionic state. This is a fast production method where flight times are on the scale of 100-300 ns. All elements up to U can be produced which gives an opportunity for new isotopes to be discovered. The beam produced has a large energy spread and is a cocktail of elements. In addition, such an approach leads to low beam purity of a specific desired ion of interest, and requires a fragment separator to select species. Current examples of in-flight facilities are at GANIL in France [34], GSI in Germany [35], NSCL/MSU

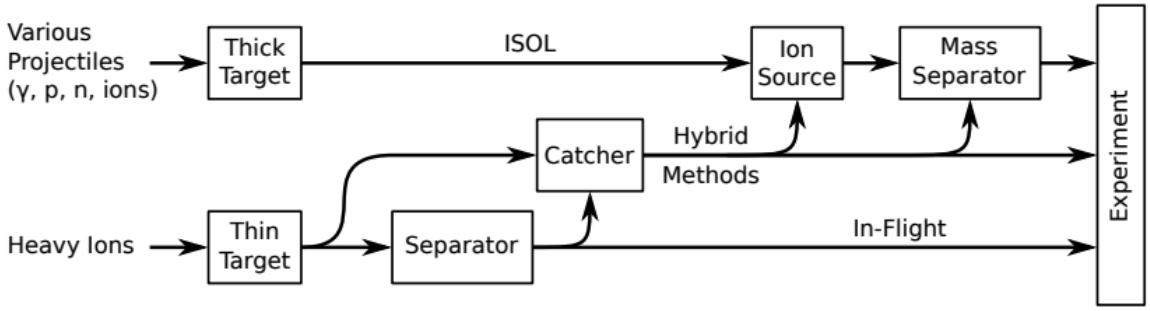

Figure 2.1: Schematic for the two radioactive ion beam (RIB) production methods: the isotope separation on-line (ISOL) method and the in-flight method. Also included is the hybrid method which uses a gas catcher, this method is not discussed in detail. Figure taken from [33].

in the US [36], RIKEN in Japan [37], and the Heavy Ion Research Facility in Lanzhou, China [38]. Future facilities or upgrades are planned at FAIR at GSI [39], and FRIB at NSCL/MSU [36].

The Isotope Separation On-Line (ISOL) method

ISOL uses light particles (typically protons, neutrons, deuterons, photons or He ions) at high energy (around 100 MeV to 1 GeV) impinged upon a thick target. The target is thick enough so the light projectile is stopped within it and nuclear fission (in the case of photons), fragmentation and spallation reactions occur in the target, depending on the target material (for example Ta, UCx, U, etc.). The reactions happen essentially 'at rest' as opposed to 'in-flight'. The reaction products diffuse out of the target through a transfer line for ionisation. Compared with in-flight, the ISOL technique is more element specific and typically leads to singly charged ions, and subsequently cleaner beams with less contamination are produced. The energy spread in the resulting beam is smaller than in-flight, originating from heating of the target and corresponding ionisation methods and geometries. ISOL beams are ideal for low energy experiments, for example in-trap high precision mass measurement experiments and laser spectroscopy. The ion beam can be re-accelerated if high-energy beams are needed. Current major ISOL facilities are HIE-ISOLDE at CERN [40, 41], SPIRAL at GANIL in France [42], TRIUMF/ISAC in Canada [43], IGISOL in Finland [44] and ALTO in France [45]. Future projects are SPIRAL-2 at GANIL [46], and ARIEL at TRIUMF [47].

2.2 Mass measurement techniques

Mass spectrometry is a direct measurement method which can be employed to measure the mass of stable or radioactive ions (given access to a RIB facility). Mass measurements of radioactive nuclei have expanded knowledge and understanding of the nucleus, which has led to the development of the nuclear shell model [2]. Current high-precision mass measurement techniques provide knowledge for nuclear structure, nuclear decay, nuclear astrophysics, as well as input and testing of theoretical models [48].

For high-precision mass measurements to be performed, mass spectrometers need high resolving power and low relative uncertainty. Mass resolving power ($R = m/\Delta m$) is the ability to separate and distinguish between two species. Relative uncertainty (precision) ($\delta m/m$) is the ratio of the absolute uncertainty of the mass value to the mass value itself. The latter has contributions from many factors including energy spread, statistics and systematic uncertainty of the measurement method or device. The precision required to determine nuclear shell effects (which are on the order of MeV) is typically δm/m = 1×10^{-7}, nuclear astrophysics δm/m = 1×10^{-7} - 10^{-8}, while other nuclear applications (for example, testing fundamental symmetries and neutrino physics) need as much as δm/m = 1×10^{-8} - 10^{-9} [7].

In the following sections different mass spectrometry techniques suitable for mass measurements of radioisotopes will be discussed and compared. The techniques discussed are considered to be a form of Time-Of-Flight (TOF) Mass Spectrometry: a particular type of mass spectrometry which utilises the principle that ions with a given kinetic energy, which are travelling the same distance, will take a different time to travel from one point to another depending on their mass-to-charge ratio, which ultimately can be used to deduce the mass.

Storage Ring Mass Spectrometry

A storage ring is used to store charged particles at well-defined energies. Currently, storage rings for RIBs exist at in-flight facilities and so facilitate the study of fragmentation based isotopes [7]. Plans exist to couple the ISOLDE-ISOL facility with a storage ring [49]. In storage ring mass spectrometry the ions are separated using bending and focusing magnetic multipoles. A beam of ions with charge q, travel through a well defined magnetic field B, with momentum p, to form a circular motion with a gyroradius of ρ (this is the radius of the circular motion) due to this field. The revolution time of an ion in a storage ring with fixed magnetic rigidity $B\rho$, defined in equation 2.1, depends on its momentum–to–charge ratio given by mv/q, where m is the ionic mass.

$$B\rho = \frac{p}{q} = \frac{mv}{q} \tag{2.1}$$

The mass-to-charge ratios (m/q) of the separated ions is deduced from their revolution frequencies ν, according to equation 2.2 where γ is the relativistic Lorentz factor typically needed for the energies used at fragmentation facilities, γ_t is the 'transition energy' of the storage ring (which all species in the storage ring are given regardless of their m/q), and $\Delta v/v$ is the velocity spread of the beam.

$$\frac{\Delta\nu}{\nu} = -\frac{1}{\gamma_t^2}\frac{\Delta(m/q)}{(m/q)} + \left(1 - \frac{\gamma^2}{\gamma_t^2}\right)\frac{\Delta v}{v} \tag{2.2}$$

Storage ring mass spectrometry uses two techniques: Schottky Mass Spectrometry (SMS) and Isochronous Mass Spectrometry (IMS), both schematically shown in figure 2.2 [50]. In SMS the ion beam is 'cooled' to increase the precision of the measurement by reducing the inherent energy spread. The revolution time of an ion in a storage ring depends on its momentum–to–charge ratio. An electron beam cooler (with cold electrons travelling in the opposite direction to the ion beam) is used to reduce the velocity spread of the ions, thereby making the second term of equation 2.2 practically zero. So, the revolution frequencies of cooled ions depends only on their mass-to-charge ratio m/q. The cooling time is 1-2 s which means the most exotic species cannot be studied and hence the technique is suitable only

for longer-lived nuclei. The ions induce a charge on a detector with each revolution. A Fourier transformation of the signal reveals a spectrum of the revolution frequencies which can be translated to the m/q and ultimately the atomic mass. IMS does not involve cooling and uses TOF measurement techniques for short-lived exotic nuclei which are injected at the transition energy γ_t. The revolutions of the ions are tuned such that ions with different velocities have different orbits within the ring so all ions of a given m/q will have the same revolution frequency. The revolution time (time-of-flight) of the different ion species are measured for each lap of the ring, thus allowing mass measurement and identification of the different species.

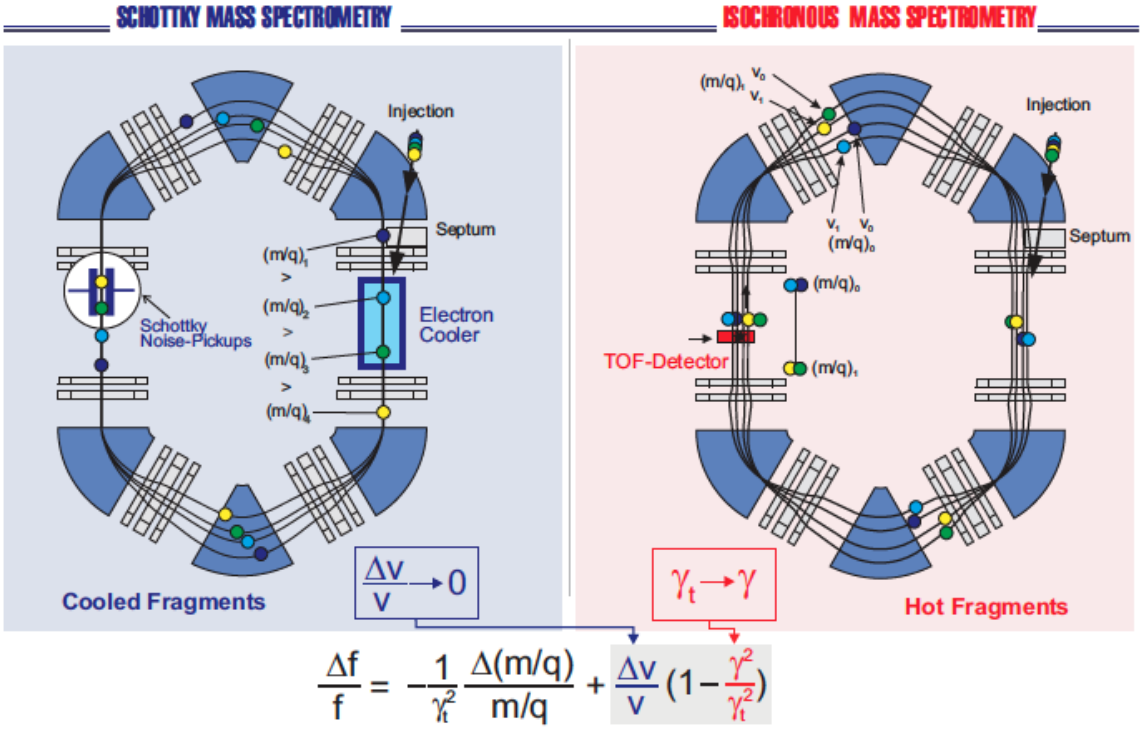

Figure 2.2: Diagram of SMS (left) and IMS (right) at the ESR. Figure from [50].

Currently, storage rings exist at in-flight fragmentation RIB facilities. Due to this production method many exotic isotopes are produced. However, they have a large energy spread. The time required for cooling in SMS to reduce the energy spread and obtain a high resolution measurement severely limits the lifetime of species possible for study at these facilities. IMS can measure short-lived nuclei (due to the lack of cooling) but is restricted in the number of ions that can be stored at one time to approximately 50. In addition to this, ideally all species from the target will be completely stripped of electrons to allow unambiguous identification, but in reality species emerge out of the target in various charge states. These all enter the storage ring and it is difficult to identify the species of interest due to the numerous A/q in the beam.

Mass resolving power of both SMS and IMS is on the order of 1×10^5 (this is an accuracy on the order of 100 keV for A$\sim$150 u nuclei), these techniques are sensitive enough to detect a single ion of interest (IOI) with production rates as low as one ion per day [7] and species

with half-lives of a few microseconds can be measured [50]. Both IMS and SMS were first developed and successfully applied at the ESR [51] at GSI, however in the meantime multiple successful experiments have also been carried out at the CSRe ring facility [52] at Lanzhou, China.

Penning Trap Mass Spectrometry

A Penning trap confines ions using a combination of electrostatic and magnetic fields. Figure 2.3 shows a diagram of the Penning trap: an electrostatic potential is produced by the biasing of the ring electrode and end cap electrodes. An electrostatic potential well is created along the magnetic field lines. Figure 2.4 shows how the magnetic field confines the ions radial motion, while the electrostatic potential well confines the ions axially (along the magnetic field lines) [48]. The combination of fields causes the ion to oscillate in a harmonic motion while being confined in three dimensions.

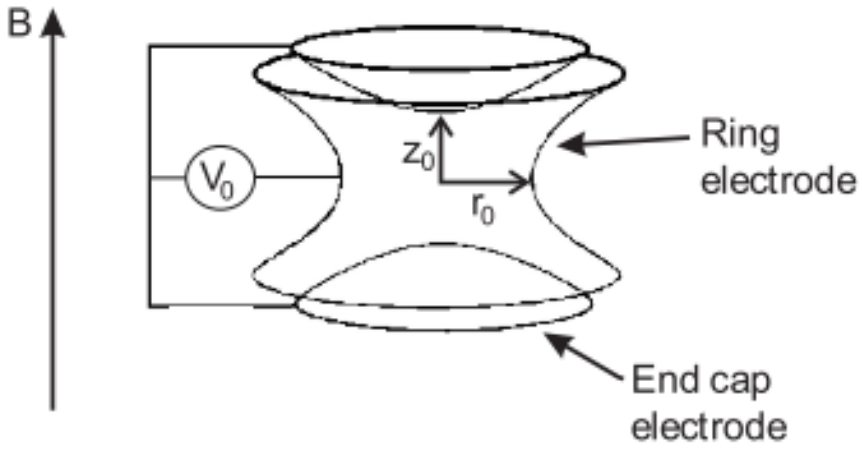

Figure 2.3: A schematic of a Penning trap. For more details, see the main text. Figure from [7].

The mass of an ion in a Penning trap is found by measuring its cyclotron frequency v_c, the frequency of the ion motion in a magnetic field, described by equation 2.3 [53] where m is the mass of the ion with charge q in a Penning trap with magnetic field strength B.

$$v_c = \frac{m}{q}\frac{B}{2\pi} \tag{2.3}$$

There are three ways to measure the cyclotron frequency v_c of ions in a Penning trap. The Time-Of-Flight Ion-Cyclotron-Resonance (TOF-ICR) [54] technique uses the application of a Radio-Frequency (RF) excitation on the trapped ions. After a defined excitation time, the ion is ejected from the trap to a detector where the time of flight is measured. Fourier-Transform Ion-Cyclotron-Resonance technique (FT-ICR) [55] measures the ion eigenmotion within the trap using a pair of pickup electrodes, and applies Fast Fourier transformation on the signal, similar to SMS in a storage ring. Phase-Image Ion-Cyclotron-Resonance (PI-ICR) [56] measures the phase of the radial eigenmotions of the ion within the trap at well-defined times projected onto a position sensitive detector outside the trap. The ions phase is reconstructed from these data and the cyclotron frequency can be deduced.

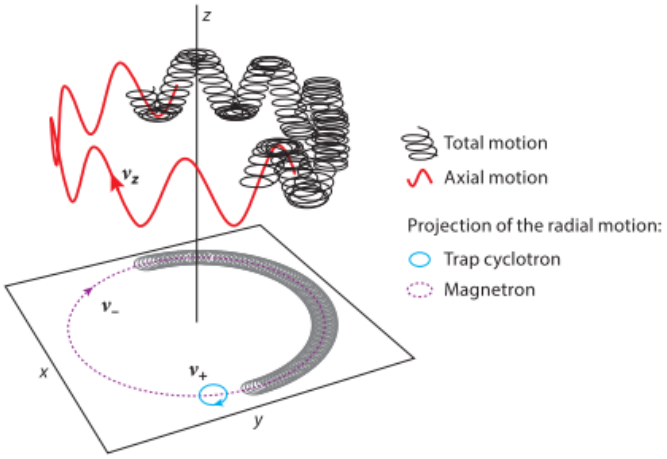

Figure 2.4: A diagram of the ion motion within a Penning trap, described in more detail in the text. Figure from [48].

TOF-ICR, due to its destructive nature, requires at least 100 ions, with ideally only a single ion in the trap at any time, to obtain a measurement with sufficient uncertainty. However, TOF-ICR is robust and universally applicable. FT-ICR, in principle, requires only one ion to determine a mass [7] but is rarely applied to radioactive ions due to the time needed to obtain sufficient data. The induced signal current in FT-ICR is so small (fA) that electronic noise can effect the measurement.FT-ICR is more complex than TOF-ICR, requires cryogenic temperatures, and the measurement benefits from highly charged ions. FT-ICR can achieve uncertainties below 1×10^{-10} on stable ions. PI-ICR is the most recently developed of the three methods and is aimed at very short-lived nuclides and investigating low-lying nuclear isomeric states. Compared with TOF-ICR, the precision of PI-ICR is approximately five times greater, and the resolving power approximately 40 times greater [48].

Penning trap mass spectrometry [57] provides the highest resolution, precision, and accuracy of all on-line mass measurement techniques, and can perform measurements on species with half-lives as low as a few milliseconds [48] and production rates as low as two ions per week [58]. Because Penning trap mass measurement techniques were initially developed for use on stable isotopes, the device and operation can be optimised and calibrated using stable isotopes [7]. This technique is very well studied and established for accuracy and precision for measurements on radioactive isotopes [7]. A mass resolution of $m/\Delta m = 1 \times 10^7$ corresponds to a few keV for A$\sim$50 u. Relative mass precisions of δm/m $= 1 \times 10^{-11}$ have been reached with stable species [59], and δm/m $= 1 \times 10^{-10}$ for radioactive species [60, 61]. The current record for the measurement of isotope with the shortest half life is ^{11}Li with $t_{1/2} = 8.8$ ms [62]. Additional methods have been developed to increase the precision of mass measurements in a Penning trap. For example, increased magnetic field strength or increasing the charge state of the ions.

Penning traps are the leading device in high-precision mass measurements for RIB. TRIUMF's ion trap for atomic and nuclear science (TITAN) [63] is such a facility. Currently there are many other online Penning trap mass spectrometers including ISOLTRAP at ISOLDE [64], JYFLTRAP [65] at the University of Jyvaskyla, SHIPTRAP [58] at GSI, TRIGATRAP [66] at the University of Mainz, LEBIT [67] at the NSCL-FRIB facility and CPT [68] at

Argonne. RIKEN are currently developing the SLOWRI Penning trap system.

Multiple-Refection Time-Of-Flight Mass Spectrometry

More recently, a new type of on-line mass spectrometry has been developed: Multiple-Reflection Time-Of-Flight (MR-TOF) Mass Spectrometry [69]. In these devices, ions are injected into a trap formed of two electrostatic mirrors between which the ions are reflected. Multiple reflections create a long path length l [70]. During this time the ions become separated according to their mass-to-charge ratio m/q. From measuring the time-of-flight t of the ions when they are ejected from the trap to a detector, their m/q can be deduced using equation 2.4, where v is the ion velocity and V is the potential.

$$\frac{m}{q} = \frac{2V}{v^2} = 2V\frac{t^2}{l^2} \tag{2.4}$$

MR-TOF mass spectrometry allows a long flight path to be achieved using a small space, which translates to a high mass resolving power ($m/\Delta m > 1 \times 10^5$). Measurement times are on the order of ms and precisions are better than $\delta m/m < 1 \times 10^{-6}$. Due to their unique performance combining high resolution, precision, operating in a fast time frame, with sensitivity able to detect below 0.01 pps these devices are ideal for mass measurements of exotic isotopes far from stability [69].

MR-TOF mass spectrometers are installed at both ISOL and in-flight facilities, these include ISOLTRAP at ISOLDE [71], TITAN at TRIUMF [72, 73], RIKEN [74], FRS at GSI [72], CPT [75] at Argonne, JYFLTRAP at IGISOL [76] and there is a diagnostic MR-TOF mass spectrometer planned at PILGRIM [77] at SPIRAL2.

Comparison of mass spectrometers

Table 2.1 compares the mass resolving power ($R = m/\Delta m$), precision ($\delta m/m$), lowest half-life of species measured ($t_{1/2}$), and order of magnitude for the typical number of ions needed for the measurement (N) for the different types of mass spectrometry discussed.

Method	R	$\delta m/m$	$t_{1/2}$	N
SMS	10^5	2×10^{-7}	1-2 s	1
IMS	10^5	1×10^{-6}	$\sim$ 1 ms	1
TOF-ICR	10^7	1×10^{-9}	$\sim$ 1 ms	100-200
FT-ICR	10^7	1×10^{-10}	$\sim$ 1 s	1
MR-TOF-MS	10^6	1×10^{-7}	$\sim$ 10 ms	10

Table 2.1: Comparison of typical values of resolving power (R = m/Δm), precision ($\delta m/m$), lowest half-life of species measured ($t_{1/2}$), order of magnitude for the number of ions needed for the measurement (N) for the different methods of mass spectrometry.

Storage ring IMS techniques can study the most short-lived exotic nuclei due to the short timescale it takes to perform a measurement, and the location of these experiments at in-flight facilities with high beam energy. Penning traps are ideal for use at ISOL facilities due to the low-energy beam. However, due to the target chemistry, some elements have low diffusion rates rendering the extraction times too long compared to the half-lives, which

makes experiments impossible. Although this can be overcome at in-flight facilities, the high-energy ion beam produced has a large momentum spread which is unfavourable with the low energy and emittance needs for Penning trap mass spectrometry [48]. Penning trap mass spectrometry excels in resolving power and precision. Unlike a Penning trap, MR-TOF mass spectrometry can simultaneously measure several species, like a storage ring, but with a much simpler data analysis process. The combination of high resolving power, fast measurement cycle, and high sensitivity in MR-TOF mass spectrometry make it applicable for the study of exotic isotopes produced at a low rate with high contamination.

High-precision mass measurements performed by the TITAN MR-TOF mass spectrometer (MR-TOF-MS) are the subject of this doctoral work. The TITAN facility, where the work was conducted, is discussed in chapter 3 where a detailed explanation of the principles of the TITAN MR-TOF-MS is included. Provided in chapter 4 is the first comprehensive study of the systematic performance of the TITAN MR-TOF-MS leading to a detailed error budget of all results produced by the device. Chapter 5 presents the scientific results of this thesis: precision mass measurements of Ca, Sc, Ti and V isotopes in the N=32,34 region, supported by half-life measurements of Ti isotopes. The findings and implications of the research are explored, before concluding and looking forward in chapter 6.

Chapter 3

The TITAN Facility

The experiments described in this thesis were performed at TRIUMF's Ion Trap for Atomic and Nuclear science (TITAN) [63], which is located at the Isotope Separator and Accelerator (ISAC) [43] facility at TRIUMF, Vancouver, Canada. The data were taken with the TITAN Multiple-Reflection Time-Of-Flight Mass Spectrometer (MR-TOF-MS) [78]. Details of beam production are described in section 3.1, and the TITAN facility is described in section 3.5.

3.1 Beam production at ISAC-TRIUMF

TRIUMF is Canada's particle accelerator centre located in Vancouver, Canada. The TRIUMF cyclotron, the largest in the world, is dedicated for research in nuclear physics, particle physics, nuclear medicine, materials science, and accelerator physics [43]. The Isotope Separator and ACcelerator (ISAC) [43] facility at TRIUMF, shown in figure 3.1, uses the well established Isotope Separation On-Line (ISOL) [79] method to produce Radioactive Ion Beams (RIBs).

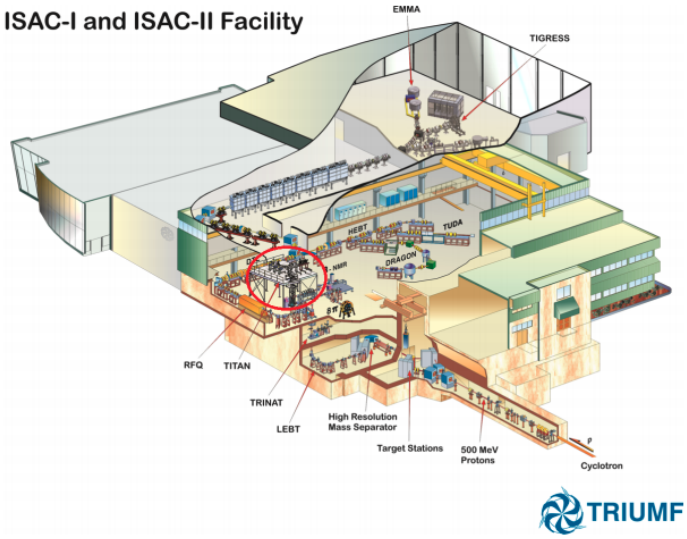

Figure 3.1: The TRIUMF-ISAC facility with TITAN shown in the red circle. Image taken from [79].

Protons from the cyclotron, at energies up to 500 MeV and currents up to 100 μA [80], are impinged upon a thick target, see figure 3.2. The target is composed of compressed disks made from material, typically metal composites, containing chemical elements from heavy to light Z [43]. In the centre is a three pronged electrode contact connection for heating to 2300°C, and the transfer tube. Inside the target, proton beam induced nuclear reactions occur to generate radioactive species. Reactions include (for heavy material) fusion, fission and spallation. The products diffuse inside the target and down to the relatively colder surfaces as neutral atoms. Various and specific ionisation methods are used to generate ionised isotopes.

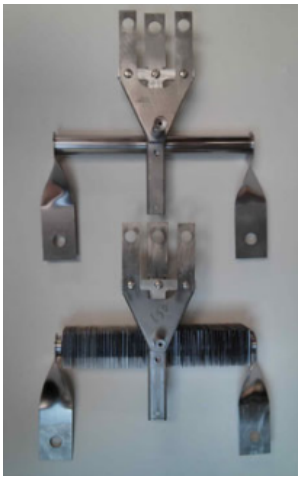

Figure 3.2: Image of two standard ISAC targets: low power (top) and high power (bottom). The high power target has metal fins along the target tube for cooling. The targets are 19 cm long between the holders, with the 3-pronged heating electrode contacts and the transfer tube in the middle. Image from [43].

3.2 Ion sources

To generate specific beams, various ion sources are utilised. The beam formed from these isotopes is delivered at 20-60 keV transport energy to a magnetic mass separator. After selection the remaining beam is delivered to the experiment. There are four general ion sources available at TRIUMF.

The Surface Ion Source (SIS)

The most simple of the ion sources available at TRIUMF is the Surface Ion Source (SIS) [43]. This is most effective for alkalis and some rare earth elements, with an ionisation potential below 6 eV. The transfer tube, made of Ta, has inside a Rh foil which surface ionises the atoms as they escape from the target. The first ionisation potential of group I and II elements in the periodic table is lower than the work-function of the first electron of Rh, so, for these elements it is energetically favourable to 'share' an electron. The result is a liberated ionised isotope.

The TRIUMF Resonant Ionisation Laser Ion Source (TRILIS)

The TRIUMF Resonant Ionisation Laser Ion Source (TRILIS) [81, 82] utilises an element-selective two- or three-step laser ionisation scheme. For this, the laser wavelengths are chosen to be resonant with the excitation steps of the selected species, thus exciting the valence electron of the atom into the continuum (resulting in ionisation). Figure 3.3 shows an example of the laser ionisation scheme of Ti.

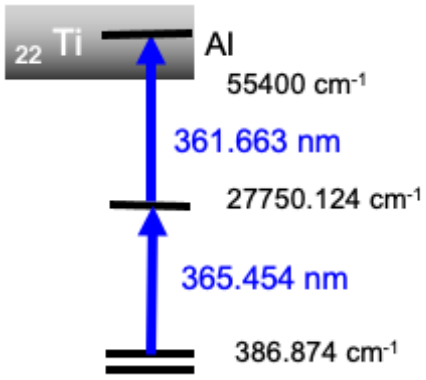

Figure 3.3: Example of a two-step Ti laser ionisation scheme. Laser wavelengths are shown in blue. AI indicates autoionisation.

Figure 3.4 shows how multiple laser beams overlap, and are injected through the pre-separator magnet, to form the ionisation region [81]. Temperatures are around 2000°C to enable optimal extraction of the desired species from the target [82].

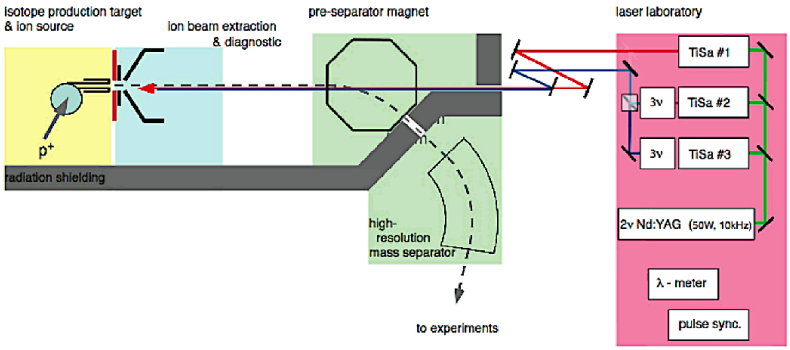

Figure 3.4: Image of the TRILIS laser setup and the laser beam path to the ISAC target station. The laser beams overlap upon entrance into the pre-separator magnet. Figure from [81].

The Ion Guide Laser Ion Source (IG-LIS)

A specific version of TRILIS is the Ion Guide Laser Ion Source (IG-LIS) [83], which uses a combination of laser ionisation and suppression of surface ionised background ions. Resonant laser ionisation maximises the yields of the selected elements, as in TRILIS, and uses an RF guide for axial confinement. A charged repeller electrode is used to block all surface

ionised species so only the neutral atoms enter the RF guide and are laser ionised, and then extracted. This reduces contamination from unwanted surface ionised species, and results in a highly selective ion source, like TRILIS, but with decreased beam intensity due to the repeller electrode removing all except the species ionised by resonant laser excitation.

The Forced Electron Beam Induced Arc Discharge (FEBIAD)

The Forced Electron Beam Induced Arc Discharge (FEBIAD) [84] plasma ion source is used for species with high ionisation energies, for example noble gases. Species from the target diffuse down the transfer line and into the plasma chamber. Electrons produced by a hot cathode are accelerated through a potential of 100-200 V to an anode, and a plasma is formed by RF radiation. The plasma interacts with the neutral isotopes from the target and ionises isotopes though impact ionisation. The ions are then extracted and formed into a beam.

The Off-Line Ion Source (OLIS)

For stable (non-radioactive) beam, the Off-Line Ion Source (OLIS) [43, 85] produces beams for experiments in the ISAC facility. OLIS has the options of a surface ion source, microwave cusp ion source, a multi-charge ion source, and a hybrid surface-arc discharge ion source. The OLIS surface ion source is similar to the ISAC SIS, and is used for the production of stable alkali isotopes. The microwave cusp ion source [86] produces cocktail ion beams from microwave-power applied to a mixture of gases to form a magnetically confined plasma. The multi-charge ion source [87] was installed for species with higher charge states ($A/q \leq 6$) for use with the linear accelerator or post-accelerator system. The hybrid surface-arc discharge ion source [88] was developed for a specifically requested $^{40}Ca^{2+}$ ion beam. Beam from ISAC or OLIS can be delivered to many experimental facilities at ISAC, one of which being TRIUMF's Ion Trap for Atomic and Nuclear science (TITAN) [43].

3.3 Beam transport

After the ion source is a pre-separator magnet which performs a preliminary mass selection to clean the beam and reduce contamination. Following the pre-separator magnet is the high-resolution mass separating magnet, labelled in figure 3.1. The ISAC mass separator system is designed for the mass range of 6 to 238 u (He to U isotopes) [80], and has a mass resolution of approximately $R = m/\Delta m = 2000$ [43]. The ion beam exits the mass separator and is injected into the low-energy-beam-transport (LEBT) line. The 20-60 keV beam is transported to the ISAC-I experimental hall.

3.4 The ISAC Yield Station

The ISAC Yield Station [89], situated in the ISAC-I experimental hall, is primarily used for determining beam composition and intensity prior to beam delivery to experiments, and can also perform half-life measurements. The radioactive ion beam is implanted onto aluminised Mylar tape within a vacuum chamber. Surrounding the implantation spot are two PIN

diodes for α-detection, four plastic scintillator detectors for β-detection, and a single high-purity germanium (HPGe) detector for γ-detection. The collected data permits half-life determinations and γ-ray tagging.

3.5 TITAN

TITAN, circled in red in figure 3.1 and shown schematically in figure 3.5, comprises multiple experimental elements for performing precision mass measurement experiments on trapped ions for studies of nuclear structure, nuclear astrophysics, and fundamental symmetries. The combination of ion traps at TITAN (including an Electron Beam Ion Trap (EBIT) charge-breeder, Penning trap, and Multiple-Reflection Time-Of-Flight Mass Spectrometer (MR-TOF-MS) isobar separator) provides unique opportunities for mass spectrometry not possible at any other facility. The facility is located in the ISAC experimental hall which gives access to RIB for these studies. The different traps, detailed in the following sections, each have a dedicated function [90]. For example, the EBIT for producing highly charged ions (HCI), the Penning trap for high-precision mass measurements, and the MR-TOF-MS for fast mass separation and identification.

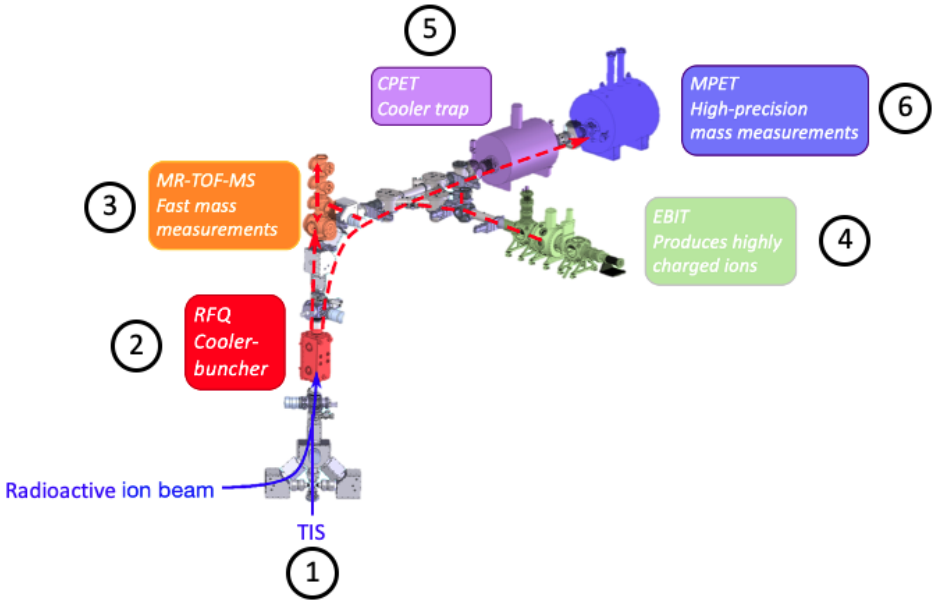

Figure 3.5: Schematic diagram of the TITAN facility. Continuous ion beam (blue) is sent to the TITAN Radio-Frequency Quadrupole (RFQ) where it is cooled and bunched. The bunched beam (red dashed) can then be sent to the other traps: the Multiple-Reflection Time-Of-Flight Mass Spectrometer (MR-TOF-MS), the Electron Beam Ion Trap (EBIT), the Cooler Penning Trap (CPET, currently under development), and the Measurement Penning Trap (MPET). The numbers refer to specific elements which are discussed in the main text. The RFQ and MR-TOF-MS were used in this doctoral work. Figure modified from [78].

The TITAN Ion source

The TITAN Ion Source (TIS) (labelled 1 in figure 3.5) is a stable surface ion source which

can produce alkali beams like $^{39,41}K^+$ and $^{85,87}Rb^+$ for off-line operation and calibration of the TITAN experimental system independent of beam from ISAC or OLIS.

The TITAN RFQ cooler-buncher

The first ion trap is a segmented, linear, gas-filled Radio-Frequency Quadrupole (RFQ) cooler/buncher (indicated as 2 in figure 3.5) [91, 92] which accumulates the continuous ion beam of (typically) singly charged ions (SCI), cools them using hydrogen or helium gas, and releases the ions in well defined bunches. The cooled ion bunches can be sent to any subsequent trap depending on the intention of the measurement. This RFQ consists of four rods, whose RF is 180° out of phase with its nearest neighbours. The RF field results in the transverse confinement of the ions. Longitudinal segmentation of the rods and applying an appropriate electrostatic field leads to an electrostatic potential that guides and holds the ions. The RFQ is required at TITAN for general beam preparation, to reduce the 20 keV ion beam from ISAC to 1.3 keV for use at TITAN, to reduce energy distribution (cooling) for high-precision experiments, and to form bunches of the continuous ion beam for high-efficiency pulsed experiments.

The TITAN Electron Beam Ion Trap & decay spectroscopy program

The Electron Beam Ion Trap (EBIT) (labelled 4 in figure 3.5) [93] traps and charge breeds singly charged ions (SCI) to multiply charged ions (MCI) or highly charged ions (HCI). The ions can be extracted as a bunch and sent to subsequent traps for mass measurement. Alternatively, HCI can be stored in the TITAN EBIT and in-trap decay-spectroscopy studies of HCI [94] can be performed, utilising the open geometry of the EBIT combined with a suite of detectors.

In general, an EBIT uses electron impact ionisation to charge breed SCI in order to produce MCI or HCI. Electrons are released at the electron gun and accelerated as a beam through a series of cylindrical drift tubes towards the electron collector. The potential difference between the drift tubes and the electron gun cathode defines the kinetic energy of the electrons. A pair of superconducting Helmholtz coils magnetically confines and compresses the electron beam with maximum density occurring at the trap centre at the highest field. This geometric configuration together with the space-charge of the electron beam itself leads to a 3-dimensional confinement of the ions, while electron impact ionisation takes place. By switching the electrostatic potential of the drift tube the ions can be extracted.

The TITAN Measurement Penning trap

The TITAN measurement Penning trap (labelled 6 in figure 3.5) [95] is a system developed to perform high-precision mass measurements on SCI and HCI. The TITAN measurement Penning trap is the only on-line system coupled to a charge breeder to allow measurements on highly charged ions. A Penning trap uses a strong homogeneous magnetic field to radially confine ions, combined with a quadrupolar electrostatic potential to axially trap the ions. The ions are trapped in a small volume so well-defined and stable conditions can be maintained. For measurements, the cyclotron frequency, as described in equation 2.3, which scales with m/q (the mass-to-charge ratio), is measured via the time-of-flight ion-cyclotron-resonance technique (TOF-ICR) [96]. The homogeneous magnetic field strength within the trap can be

derived from calibration measurements, so the m/q can be calculated. By using HCI from the EBIT, the resolving power R in the Penning trap can be increased according to equation 3.1 where T_{RF} is the radio-frequency excitation time [97] for the TOF-ICR.

$$R = \frac{m}{\Delta m} \propto \frac{qBT_{RF}}{2\pi m} \tag{3.1}$$

Penning trap mass spectrometry is the most precise on-line mass measurement technique currently [48]. The maximum precision of the TITAN Penning trap is $\delta m/m = 3 \times 10^{-9}$ achieved in measuring ^{27}Al [98]. TITAN currently maintains the record of measurement of the shortest-lived nuclide with Penning trap mass spectrometry: ^{11}Li with a half life of 8.8 ms [62] and precision of $\delta m/m = 7.5 \times 10^{-9}$.

The TITAN Multiple-Reflection Time-Of-Flight Mass Spectrometer

The TITAN MR-TOF-MS [78], shown at 3 in figure 3.5 and in the red box in figure 3.6, is used to perform mass measurements and can also be used for isobaric separation [99]. An MR-TOF-MS uses two electrostatic ion mirrors to achieve multiple reflections of the ions to generate a long flight path so they are spatially separated according to their mass-to-charge ratio m/q. As the quasi-monoenergetic bunch of different ions oscillates between a pair of electrostatic mirrors, it separates into its components based on their m/q as the velocity is energy and mass dependent. The mass of each component can be deduced by recording and comparing the individual time of flight.

Figure 3.6: Image of the TITAN platform with a human standing underneath the MR-TOF-MS (highlighted in the red box) for scale.

As an isobar separator, the technique of 'retrapping' is used to mass-separate ions in space, or correspondingly in (arrival) time at a certain point in space [99]. Ions outside of the chosen time-of-flight window (corresponding to the unwanted species) can be ejected from the system. An isobarically clean bunch of ions can be used either for mass measurement with the MR-TOF-MS or be sent to another trap, for example the measurement Penning trap for high-precision mass measurement, or the EBIT for charge breeding.

The maximum precision achieved with the TITAN MR-TOF-MS is $\delta m/m = 8 \times 10^{-8}$ [100], with measurements performed on ions with lifetimes as short as 5.5 ms [101]. The MR-TOF-MS is extremely sensitive and requires a rate of only 0.01 particle per second for a measurement. The setup is described further in this section, and systematic studies including error evaluations will be discussed in chapter 4.

The TITAN MR-TOF-MS is based on the design in [72, 102], and has two main sections: a buffer-gas-filled low-energy ion transport and preparation section [103], indicated 1 in the schematic of the TITAN MR-TOF-MS shown in figure 3.7, and a ultra-high-vacuum ($\sim 1 \times 10^{-8}$ mbar and lower) electrostatic mass analyser section, indicated 2 in figure 3.7.

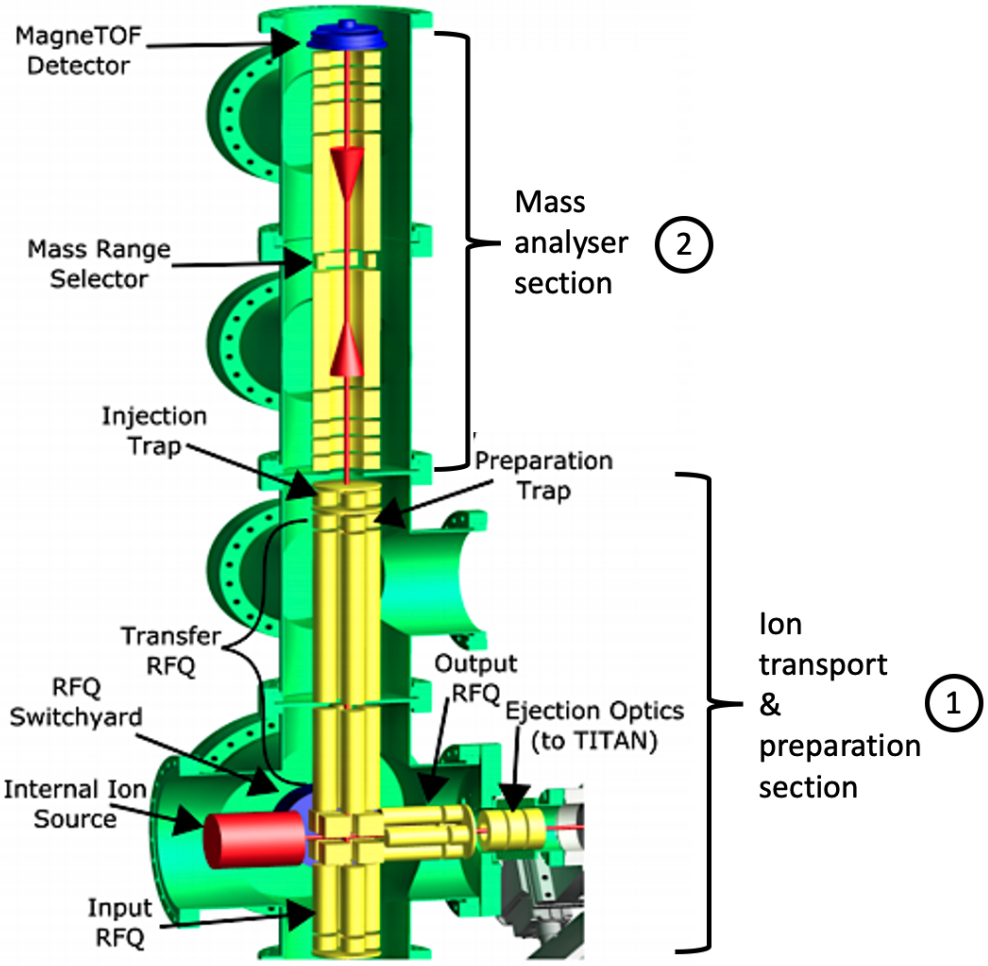

Figure 3.7: A diagram updated from [78] of the TITAN MR-TOF-MS. Ion optical elements are highlighted in yellow, detectors are shown in blue. The red arrows indicate the direction of ions passing through the system.

The ion transport & preparation section

Part 1 includes a series of trapping and cooling systems [33, 72]. The input RFQ guides beams from the TITAN RFQ to the six-way RFQ switchyard [103] which directs the beam and allows merging of multiple beams. Thus, stable calibrant ions from an internal ion source may be used during RIB experiments. Ions proceed through the transfer section and are accumulated in the injection trap where they are cooled and bunched. The injection trap is a buffer-gas filled linear RF ion trap. Collisions with the He gas cool the trapped ion bunch to reduce the size and thus reduce the time and energy spreads of the ejected ion bunches [104]. The injection trap can also be used for retrapping. The ion bunch is injected into the mass analyser through an accelerating lens and aperture of the entrance electrode of the first ion mirror.

The mass analyser section

Part 2 is the mass analyser, shown in figure 3.8, formed from nine cylindrical electrodes: the outermost three electrodes (E1-3 and E7-9) each form two identical axially symmetric gridless electrostatic ion mirrors at either end of the analyser and have openings (apertures) for injection or extraction, an accelerating Einzel lens electrode next to each mirror (E4 and E6), and the central electrode (E5) is a drift tube at ground potential. The ion-optical design is based on [104], but this device is a more compact version [72]. The voltages of the first ion mirror are switched to low values (lower than the nominal kinetic energy of the incoming bunch) during injection at the start of the measurement cycle. At the centre of the analyser is the mass range selector (MRS) [72], a cylindrical electrode split four-fold, used to remove non-isobaric contaminants from the time-of-flight (TOF) spectra. A pulsed potential is applied to the electrodes to deflect ions outside of a chosen TOF and therefore mass-to-charge (m/q) range. The deflection voltage is applied only after the ion of interest (IOI) has passed, and therefore all contaminants can be deflected out of the analyser via two apertures before and after the mass range selector. The MRS is applied for several turns during each measurement cycle.

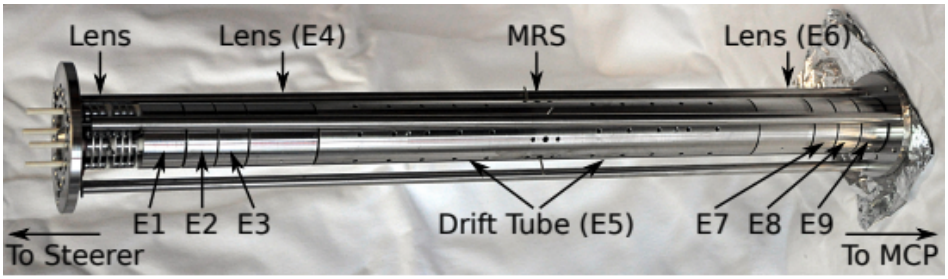

Figure 3.8: An image of the mass analyser section of the TITAN MR-TOF-MS. The ion optics elements are labelled. Image from [78].

Ions are reflected between the mirror electrodes and become spatially separated according to their A/q. The ions are ejected by switching off the mirror potential where they are ejected to either a TOF detector [105] for mass measurement or back into the injection trap for mass-selective retrapping. The electron multiplier detector (MagneTOF) is chosen because it operates well under high pressure ($\sim 1 \times 10^{-8}$ mbar and lower) and has a narrow pulse width (FWHM < 0.55 ns), which is good for mass resolving power. In addition, it does not

need to be stored under vacuum and has low-noise performance. Using the detector, the ions TOF is measured and their mass deduced.

The time at which the ion bunch is injected into the mass analyser is the start of their flight time. While the ions are in the injection trap they will have some distribution in space, time and energy. This is reduced by buffer gas cooling but there remains a small amount which carries forward into the motion of the ions when in the analyser. The ions path also includes travel from the injection trap into the analyser, and from the analyser to the detector when they are ejected. To correct for the distribution, and the small additional distances, after injection into the analyser the ions first undergo a time-focus shift (TFS) turn [106]. The TFS turn is used to focus the ions regardless of their starting distribution and compensates resulting effects. The time focus of the ions in the analyser is altered by varying the potential of the electrodes which form the mirrors (and hence the reflecting and accelerating field), as seen in figure 3.9. The TFS reflection accelerates ions which are 'behind' and reduces the energy of ions which are 'ahead' in order to focus them in time. Figure 3.10 shows the initial time focus of the ions leaving the injection trap, the TFS reflections focusing ions to the centre of the analyser, and the isochronous turn (IT) reflections focusing them on the detector plane. The ions are separated according to their mass using a defined series of isochronous turns (IT). The combination of reflecting and accelerating fields in the mirror electrodes means these reflections are independent of the ion energy so the TOF only depends on A/q. To achieve the highest possible resolving power of the device, the ions undergo hundreds of IT between the two mirrors until they are ejected from the analyser.

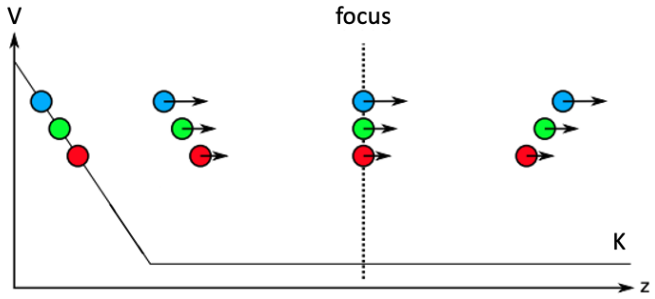

Figure 3.9: Diagram describing the effect of time focus shift (TFS): ions which begin 'behind' (blue) gain kinetic energy (K) due to the electric acceleration field and arrive at the same time as ions which began 'ahead' (red) as their energy gain is reduced. Image modified from [33].

In the analyser, ions reflected between the electrostatic mirrors reach flight path lengths up to hundreds of meters. The total time-of-flight t_{TOF} and total distance travelled l_{TOF} of an ion in the MR-TOF-MS can be found from the sum of the path from the injection trap to the detector, including the TFS reflection (t_{TFS}, l_{TFS}), and N number of IT reflections (t_{IT}, l_{IT}) within the analyser.

$$t_{TOF} = t_{TFS} + Nt_{IT} \tag{3.2}$$

$$l_{TOF} = l_{TFS} + Nl_{IT} \tag{3.3}$$

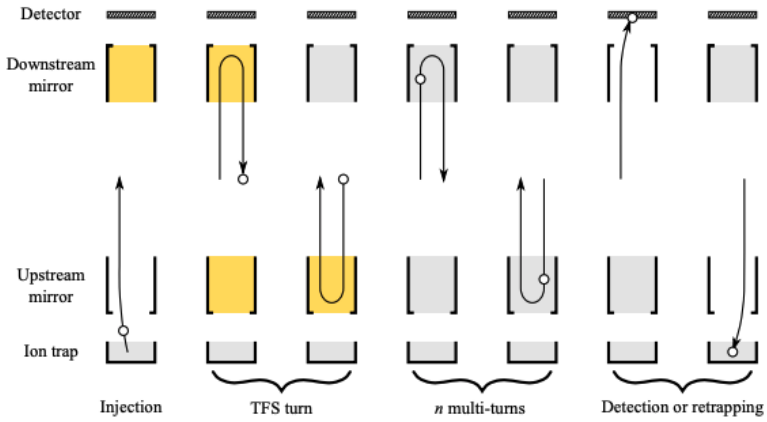

Figure 3.10: Schematic diagram showing the time focus (circles) of an ion bunch in the MR-TOF-MS. The ions path is overlapping in reality, with only one pair of mirrors, but is separated and shown repeatedly in sequence from left to right for clarity in this graphic. Yellow indicates the TFS turns, grey is IT. Figure from [107].

The mass of an ion is determined based on the relationship between the mass m, the charge q, and the time-of-flight needed to travel a certain flight path. The potential V of the ion mirrors is set to provide ions with velocity v.

$$E_{pot} = E_{kin} \tag{3.4}$$

$$Vq = \frac{1}{2}mv^2 \tag{3.5}$$

Equation 3.5 can be solved for the mass-to-charge ratio m/q.

$$\frac{m}{q} = \frac{2V}{v^2} = 2V\frac{t^2}{l^2} \tag{3.6}$$

Equations 3.2 and 3.3 allow the introduction of calibration parameters c, t_0 and b.

$$\frac{m}{q} = 2V\frac{t_{TOF}^2}{l_{TOF}^2} = 2V\frac{t_{TOF}^2}{(l_{TFS} + Nl_{IT})^2} \tag{3.7}$$

$$\frac{m}{q} = 2V\frac{(t_{TOF} - t_0)^2}{l_{TFS}^2(1 + N\frac{l_{IT}}{l_{TFS}})^2} \tag{3.8}$$

t_0 is a time offset, originating from the time difference between when the ions are triggered to be injected into the trap compared with when they actually enter the trap, plus the delays for the signal to reach the data acquisition. c is a calibration parameter specific to this device which depends on the kinetic energy and path-length of the ions not including IT (only injection, TFS, and ejection) as described in equation 3.9.

$$c = \frac{2V}{l_{TFS}^2} \tag{3.9}$$

t_0 and c can be determined from reference measurements using ions with well-known masses. b is used for scaling to multiple turns as in equation 3.10.

$$b = \frac{l_{IT}}{l_{TFS}} \tag{3.10}$$

Thus, the mass of the ions can be determined from equation 3.11 via

$$\frac{m}{q} = c\frac{(t_{TOF} - t_0)^2}{(1 + Nb)^2} \tag{3.11}$$

If the calibrant ion has the same mass number and charge, and therefore performs the same number of turns, as the ion of interest (IOI) then equation 3.11 can be simplified to

$$\frac{m}{q} = c(t_{TOF} - t_0)^2 \tag{3.12}$$

Mass resolving power R is calculated by equation 3.13, where m is the mass of the ion, and Δm is FWHM of that mass peak. Mass resolving power of the TITAN MR-TOF-MS routinely exceeds $R > 200\,000$.

$$R = \frac{m}{\Delta m} = \frac{t}{2\Delta t} \tag{3.13}$$

Methods for reducing contamination

When performing experiments using RIB, the spectra can be dominated by contaminants with much higher yields than the species of interest. Two techniques specific to the TITAN MR-TOF-MS can be applied to combat this: firstly 'retrapping' [99] and secondly 'collision induced dissociation (CID)' [100].

Retrapping selectively 'retraps' the ions of interest within the MR-TOF-MS system and expels all other ions [99]. Figure 3.11 shows a simple diagram describing mass-selective retrapping. Different species are spatially separated in the analyser. The potential of the entrance electrodes is lowered to allow ions to fly back into the injection trap. The injection trap potential is closed only for a specific TOF window (when the ion of interest is inside) and thus all ions which arrive before and after that window are reflected. The purified beam can be reinjected back into the analyser for mass measurement.

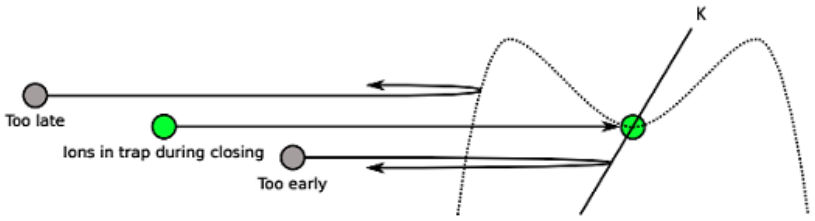

Figure 3.11: Diagram describing mass-selective retrapping using the injection trap potential (dashed line) to selectively retrap only the IOI. Ions extracted from the mass analyser are transported back to the injection trap. The ions are separated in space according to their mass, with kinetic energy K. By timing the switch of the capture electrode potential (indicated dynamically by the diagonal line), both for open and closing, specific ions can be captured. Figure modified from [33].

CID is used to remove contaminant molecular species which are created in gas stopping cells when reducing beam energy [100, 108]. Increasing the gas pressure in the input RFQ of the MR-TOF-MS breaks apart the contaminant molecules, fragmenting the molecules into separate elements (with a different mass-over-charge ratio), which are then no longer in the spectra at the mass unit of interest.

Chapter 4

The TITAN MR-TOF-MS system

The MR-TOF-MS system is an important part of mass determination and beam preparation at TITAN. Its basic operational principle has been introduced in chapter 3. The uncertainty of mass measurements studied with well-known calibrant isotopes has a dominant contribution from systematic errors, hence, in this chapter, a detailed study of the MR-TOF-MS characteristics, performance, and uncertainty is presented. Despite the dramatic rise of MR-TOF mass spectrometry in RIB mass spectrometry, a comprehensive examination of systematic uncertainties has yet to be published. As many of these are device specific (as opposed to experiment specific) they can be examined through off-line, as well as on-line, studies.

In chapter 3 an ideal MR-TOF-MS measurement was described: a single calibrant ion and a single radioactive ion (called the ion of interest, IOI) traverse the same electric fields, resulting in a small difference in their time of flights (TOF) due strictly to their mass difference. A realistic ion bunch however, has an energy and time distribution, which results in a peak (instead of a delta function) in the TOF distribution, whose shape depends also on tuning or shaping of the electrostatic fields. Ideally, the mechanical structure is exactly machined and aligned; however realistic imperfections affect trap lifetime and thus resolving power and precision. Besides the geometry, the employed power supplies can be dynamic or time-dependent and hence the electric field may suffer variations (such as, jitter or drift). Short fluctuations ($< \mu s$ jitter) affect only one ion and thus shift the measured TOF and mass [73, 109]. Longer fluctuations (> hours drift) threaten the stability of the tune and thus resolving power and precision.

High beam intensities cause peak broadening for the most abundant species of the resulting spectra. Moreover, the accumulative space-charge influences the overall electric field in a dynamic manner. Furthermore, peak shape in the TITAN MR-TOF-MS spectra has varied since the commissioning in 2017, when the peak shape was Lorentz-like. More recently (since 2019) the peak shape is Gaussian with tails to the left and right. This is a reflection of the detailed settings and shaping of the MR-TOF-MS mirrors. The tails depend on the tune of the analyser (and the voltages applied). The electrode voltages have been tuned in the years since commissioning to improve resolving power, and so as a result the peak shape has evolved.

Peaks overlapping one another in a spectrum, which occurs when masses are very similar, can make it difficult to obtain an optimum fit for species in close proximity and obtain their true mass values. Deadtime effects at the detector can be observed for an extremely abundant

peak with rates above 2 counts per cycle (cpc). Ion-ion interactions can be observed as peak shifting. This typically occurs via two phenomena: with rates of 0-10 cpc the ions repel each other so peak separation increases, whereas for rates of 100-1000 cpc the ions begin 'bumping into' each other and form bunches, a phenomena known in accelerator physics as 'self-bunching' [110, 111]. While accumulating data two clocks operate within the system: one to trigger the processes of the MR-TOF-MS and another to acquire data. Ideally, the two clocks are fully synchronised.

This study was conducted in 2019. Some of the sections in the chapter discuss the system in terms of years 2017, 2018 and 2019 because each year since commissioning there have been upgrades to the system which alter the associated uncertainty. Some of these upgrades are discussed here, for example, upgrading the time-to-digital converter (TDC), balancing RF amplitudes and modifying switches. Alongside this, tuning of the system voltages and operation has been developed over the past years, including limiting the incoming rate of ions. Some upgrades were done prior to the time covered here and are discussed in other theses [33, 100, 107, 112].

High-precision measurements typically rely on an isobaric species as a calibrant, which are not always available during online radioactive beam experiments. If there is no suitable calibrant ion at the same mass as the ion of interest, there is the possibility to use a non-isobar calibrant species for analysis. However this is accompanied by an increased uncertainty due to the difference in mass between the calibrant and the IOI and hence a difference in 'sampled' field regions and variation in flight path. Data from several online experiments, the details of which are given in table 4.1, were analysed to assess the capabilities of the TITAN MR-TOF-MS for the use of non-isobaric calibration species and compare the results from 45 well known isotopes with AME2016 data [8].

Table 4.1: Details of each data set including date taken, calibrant ions for parameters c and t_0, mass units (A/q) included in this study, target, and ion source.

Date	Calibrants	A/q	Target	Ion source
May 2017	$^{39,41}K^+$	52-54, 56	LPTa	SIS/TRILIS
June 2017	$^{85,87}Rb^+$	80-84	UCx	IGLIS
Nov 2018	$^{133}Cs^+$, $^{85,87}Rb^+$	97, 99, 101-103, 106	UCx	SIS/TRILIS
Dec 2018	$^{133}Cs^+$, $^{85,87}Rb^+$	106- 107	LPTa	SIS/TRILIS
Oct 2018	$^{133}Cs^+$, $^{85,87}Rb^+$	130	UCx	IGLIS
Aug 2018	$^{133}Cs^+$, $^{85,87}Rb^+$	149, 151-157	HPTa	SIS/TRILIS

For all data in this chapter the MR-TOF-MS operated on a 20 ms cycle time and, unless otherwise mentioned, beams were produced by the ISAC facility and merged with ions from a stable alkali source mounted on one side of the RFQ switchyard inside the MR-TOF-MS, shown in figure 3.7. In the case of radioactive beam either a Surface Ion Source (SIS), the TRIUMF Resonant Ionisation Laser Ion Source (TRILIS) [81] or the Ion-Guide Laser Ion Source (IGLIS) [83] were used to ionise the desired species. All systematic errors in this study are extrapolated for an ion with A/q=80, typically performing approximately 300 IT resulting in an average TOF of 7 ms.

4.1 Analyser

Mechanical & alignment uncertainties

Perfect machining and alignment would form the perfect trap and hence the lifetime, and thus resolving power and precision would be of the highest standard. Misalignment in the device can lead to asymmetry in the fields, which in turn affects the ions in the system, and therefore precision and resolution of the measurements. Perfection is impossible, so features have been built into the design of the MR-TOF-MS to aid with alignment and beam steering to strive for maximum resolving power and precision [33].

The TITAN MR-TOF-MS was aligned along the axis of the TITAN Penning trap beamline using a theodolite [113]. Alignment along the TITAN RFQ axis however, was not directly possible due to the lack of line of sight through the MR-TOF-MS RFQ switchyard. The output apertures are aligned to the axis of the TITAN Penning trap beamline. Thus, because of the independent alignment, the MR-TOF-MS input optics are not aligned with the vertical axis of the TITAN beamline (the TITAN RFQ beamline). This decision was made based on the beam quality for injection into the Penning trap being more sensitive than the injection from the TITAN RFQ into the MR-TOF-MS input optics. Moreover, since the MR-TOF-MS system was considered a standalone unit, a self-contained approach for internal alignment was preferred.

There are flanges with membrane bellows between each section of the MR-TOF-MS. These could be altered to align each separate segment during installation and commissioning. Due to the flexible bellows, the alignment of the MR-TOF input optics could be better than $\pm$ 1 mm [113]. A lens and steerer are part of the MR-TOF-MS injection optics to correct for misalignment and optimise efficiency of the ions incoming from the TITAN RFQ.

Within the MR-TOF-MS RFQ switchyard there are alignment rods, and alignment holes and threads to connect the adjacent system features. There is a set of steerer electrodes before the analyser section to further compensate for misalignment and maximise efficiency. A set of ceramic rods, as seen in figure 4.1, ensure alignment between the injection steerer, lens and analyser. A series of electrodes form a lens between the steerer and the analyser. Precision ground ceramic balls ensure distancing and alignment between the electrodes. Figure 4.1 also shows the vertical alignment rods in the analyser section, and some of the analyser electrodes (E1-5). The MRS electrodes (inside E5) function as steerers within the analyser if needed. These numerous features of the system ensure compensation for mechanical misalignment, and allow steering of the ions, minimising these effects on the system.

Uncertainty due to phase space in the injection trap

The injection trap, labelled in figure 3.7, is formed of four RF segments and two aperture electrodes at either end. After ions are injected, the 'push' aperture is switched to +1600 V, the 'pull' aperture lowered to +1000 V, before that both are biased at +1300 V. Several effects in the injection trap contribute to the systematic uncertainty.

Firstly, the phase space of ions (which describes the transverse position and velocity of the ions, and can be reduced by cooling) in the injection trap varies for different mass-to-charge ratios while they are stored in the injection trap. The effect scales with Δm since the velocity distribution is mass dependent. During the He buffer gas cooling, a lighter ion will have a greater relative momentum transfer to a He ion than a heavier ion, so the cooling is less

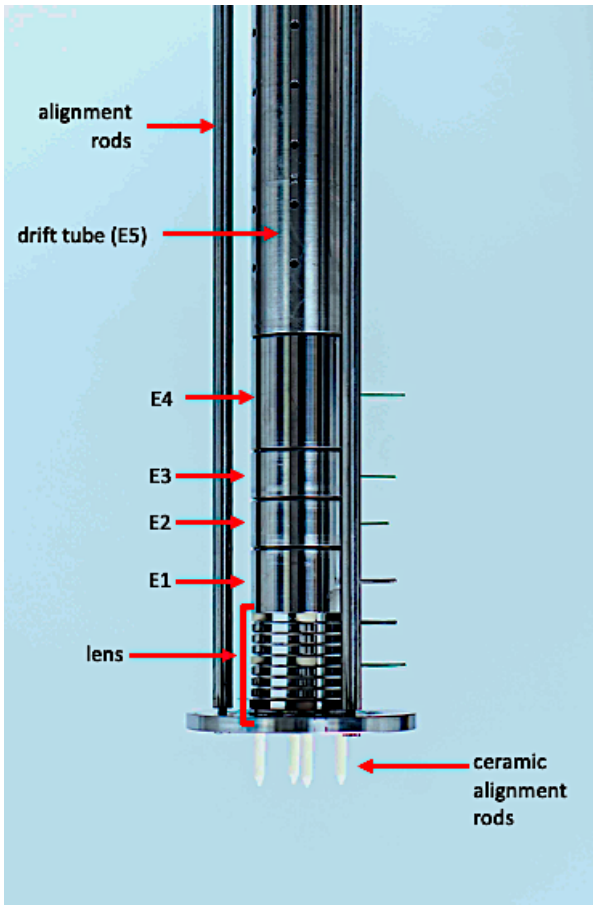

Figure 4.1: Image of part of the analyser section labelled with optics and alignment rods.

efficient for heavy ions. Prior to this study, SIMION simulations confirmed the effects from phase space in the injection trap for isobars to be negligible. The effect is, however, relevant only when the IOI and the mass calibrant are non-isobars, for example as shown in section 4.4. In order to reduce this uncertainty when using non-isobar calibrants at TITAN, the ions are ejected at a random RF phase. As a result, the initial injection states are averaged over multiple injection cycles and the variation averages out. Though, this is at the cost of a slightly reduced resolving power due to variation in the phase of the ions being injected for each measurement cycle.

In addition, the IOI and the mass calibrant ion may experience different fields from non-balanced RF amplitudes which induce an additional DC field from the surrounding apertures. Furthermore, the switching time of these apertures when injecting ions into the trap is typically on the same order as the time it takes the ions to leave the trap itself. This results in a mass dependent energy gain of the ions, such that lighter ions are physically closer to the analyser when the switching is completed, while heavier ions move slower. This effect was greatly reduced by improving the switching characteristics before the 2018 experimental season.

Upper limit values from the uncertainty due to non-ideal switching of the aperture voltages (dm/m_{PHASE}) are shown in table 4.2. The maximum uncertainty for non-isobar calibrants

is $dm/m \leq 1.4 \times 10^{-7}$ for a difference in mass of a factor of 2, given the RF amplitudes are balanced within 0.5 V. Since this effects only ions with different A/q, the effect is zero when using isobar calibrants.

Table 4.2: Uncertainty estimates due to phase space variations inside the injection trap in three different measurement campaigns. This effect applies only to non-isobars.

		2017	**2018**	**2019**
dm/m_{PHASE}	(ns)	1.0	0.5	0.5
	(rel)	2.8×10^{-7}	1.4×10^{-7}	1.4×10^{-7}

Uncertainty from non-ideal mirror switching

A major source of systematic uncertainty during MR-TOF-MS operation is the switching of the mirror electrode voltages. Variation in the switching (time, amplitude, switching-profile) manifest as systematic drifts of the IOI's TOF. The mirror electrodes within the mass analyser can have three modes: open, time-focus-shift (TFS), and isochronus turn (IT), as described in section 3.5. During an operation cycle, the electric potential of the mirror electrodes is changed four times, as shown in figure 3.10. Firstly, mirror 1 changes from open to TFS to allow the ions to enter the analyser and then for the initial TFS ion turn. Next, both mirrors sequentially will undergo a change from TFS to IT voltages. Finally, mirror 2 changes from IT to open to allow ions to reach the detector. The switching is performed when the IOI has the largest distance to the switched mirror: when it is in the other mirror, the timing is established empirically. The switching of these mirror voltages is not instantaneous but instead follows a switching process with a reproducible profile.

This effect was investigated offline using $^{133}Cs^{+}$ ions from the internal ion source by changing the time when each of the mirror voltages is switched. The slope of the electrical potential at the mirror is constant throughout the measurement. In this measurement, the point in time when the mirror switching occurs was scanned and the TOF was monitored. Upgrades have been made to isolate and stabilise the mirror power supplies in order to adjust the rise and fall time of the mirror voltages and reduce field fluctuation effects, improve reproducibility of the switching and facilitate more ideal behaviour [114].

The switching time was measured and compared to its set point, as shown in figure 4.2. Flat regions indicate insignificant deviations and therefore insignificant shifts in TOF. Curved regions indicate increasing deviations, indicating the ions experienced unstable fields. If the calibrant ion is an isobar, only the ejection (bottom panel, mirror 2: IT→open) impacts their TOF since injection and switching to IT mode occur when the IOI and calibrant are still near identical TOF (and position). The remaining scatter of the points corresponds to a $dm/m \leq 7.4 \times 10^{-8}$ (0.26 ns) uncertainty.

For non-isobaric calibrant species, however, the other switching operations matter. Here, the first operation (top panel, mirror 1: open→TFS) shows the largest effect of up to 3 ns deviation, corresponding to a maximum $dm/m \leq 8.6 \times 10^{-7}$ relative uncertainty. Furthermore, this effect increases in magnitude in proportion with the difference in time-of-flight between the calibrant ion and the ion of interest at the time of the switching operation.

Since 2018, upgrades have been made to isolate and stabilise the mirror power supplies in order to slow down the switching time of the mirrors and reduce field fluctuation effects. The

values in table 4.3 are upper limits of the uncertainty due to non-ideal switching for isobars ($dm/m_{SWITCHisobar}$) and non-isobars ($dm/m_{SWITCHnon-isobars}$).

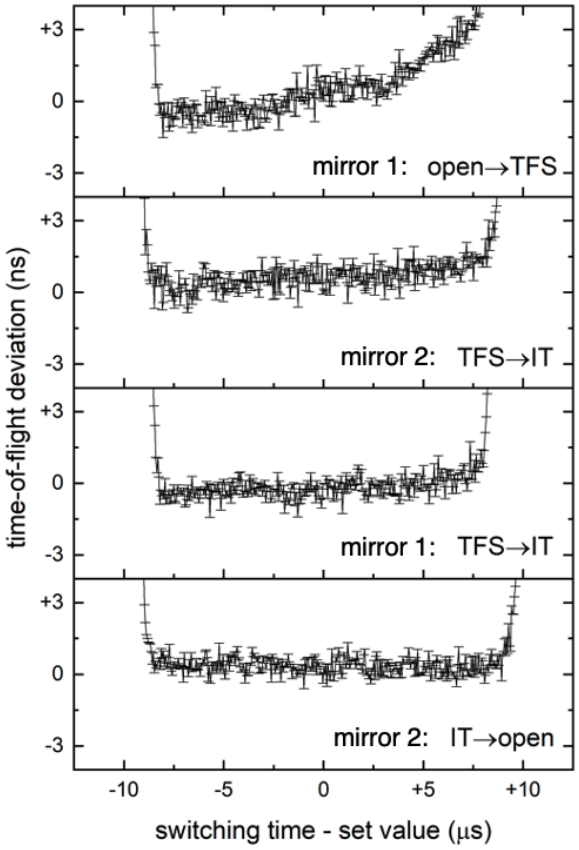

Figure 4.2: Variation in the time of flight of $^{133}Cs^{+}$ as a function of switching time difference from the set point value.

Table 4.3: Upper limit uncertainties originating from non-ideal switching for isobar and non-isobar species in 2017, 2018 and 2019 for measurements taken with the TITAN MR-TOF-MS. Uncertainties are shown as absolute values (ns) for a 7 ms time-of-flight and as relative uncertainties (rel).

		2017	**2018**	**2019**
$dm/m_{SWITCHisobar}$	(ns)	0.80	0.42	0.26
	(rel)	2.3×10^{-7}	1.2×10^{-7}	7.4×10^{-8}
$dm/m_{SWITCHnon-isobar}$	(ns)	3.00	3.00	1.00
	(rel)	8.6×10^{-7}	8.6×10^{-7}	2.9×10^{-7}

Uncertainty due to space-charge in the analyser

Ion-ion interactions occur between charged species with similar masses which travel in close proximity to one another in an external field. The Coulomb repulsion between the equally positive charges results in peak shifts in the TOF spectrum, the magnitude of which depends on the mass difference between the two species participating. Space-charge effects were investigated using the isobar pair of $^{40}Ar_2^+$ and $^{80}Kr^+$, as shown in figure 4.3. The isobar pair were delivered with comparable rates from OLIS to the TITAN MR-TOF-MS. The overall rate was varied from an intensity of approximately 0.02 counts per cycle (cpc) of $^{40}Ar_2^+$ and 0.03 cpc of $^{80}Kr^+$ (combined rate of 0.05 cpc) up to 5 cpc $^{40}Ar_2^+$ and 7.8 cpc of $^{80}Kr^+$ (combined rate of almost 13 cpc).

Using $^{80}Kr^+$ as the calibrant peak, the relative mass deviation of $^{40}Ar_2^+$ from the literature value indicates the rising effect of the ion-ion interactions as the beam rate is increased. The results of the study indicate the optimal operating intensity is on average less than 1 cpc.

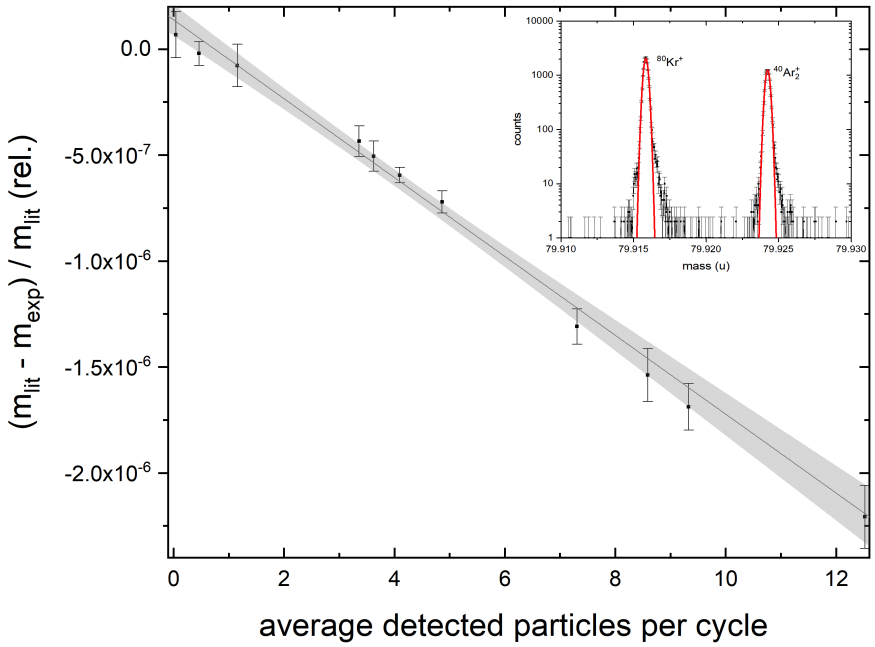

Figure 4.3: Increasing number of ions within in the analyser from an average of 0.05 counts per cycle up to a total of 13 counts per cycle demonstrates an increase in the relative mass deviation from literature with a rate of $dm/m = -1.9 \times 10^{-7}$ per detected particle per cycle. Data taken using OLIS beam of $^{40}Ar_2^+$ undergoing 300 IT in the analyser, using $^{80}Kr^+$ as the calibrant. Inset: Sample MR-TOF-MS spectra of the isobar pair of $^{40}Ar_2^+$ and $^{80}Kr^+$, a Gaussian fit is shown in red.

Uncertainty due to the mass range selector (MRS)

The mass-to-charge spectrum of the MR-TOF-MS displays all ions detected in the system, which can often include ions of different species undergoing different numbers of revolutions in the analyser. The additional species in the spectrum can be removed by pulsing the MRS

quadrupolar electrode to deflect ions outside of a defined time-of-flight (and therefore mass-to-charge) range, as described in section 3.5. Recently the switches which control the changing electrode voltage were updated for more precise switching times of about 80 ns [112] from 160 ns, to better define the start and end of the TOF window.

As a consequence of using the MRS, all ions in the system experience some effects when pulsed deflector voltage is switched on and off. To investigate this effect, the MRS was switched on (voltage applied) and off (zero voltage) periodically during a measurement cycle of $^{133}Cs^{+}$ ions from the internal ion source [112]. The centre of the $^{133}Cs^{+}$ peak was recorded and the variation analysed. The systematic shifts due to the MRS are at maximum $dm/m \leq 8.6 \times 10^{-8}$ as documented in table 4.4. The scale of these effects is non-negligible and requires further investigations and improvements.

Table 4.4: Maximum uncertainty from using MRS (relevant for isobars only) in years 2017, 2018 and 2019.

		2017	**2018**	**2019**
dm/m_{MRS}	(ns)	0.68	0.3	0.3
	(rel)	1.9×10^{-7}	8.6×10^{-8}	8.6×10^{-8}

4.2 Detection

Uncertainty due to instabilities of the timings

While accumulating data there are two clocks operating within the system: one to trigger the processes within the MR-TOF-MS (TTL) and one for the data acquisition (TDC). A discrepancy in the TTL and TDC timings would contribute uncertainty toward the time-of-flight value. The TDC was upgraded in 2018. Previously an Ortec 9353 TDC was used during the measurements of 2017. This was replaced in 2018 with the FAST ComTeK MCS6A TDC.

To estimate the instability of the timing system, the TTL was fed directly to the TDC for a long ($>$ 12 hours) measurement and the peak drift was analysed. The resulting peak had a standard deviation of 0.3 ns, contributing to the relative uncertainty at $dm/m \leq 8 \times 10^{-8}$ for a TOF of 7 ms. This is considered to be the maximal effect, and most likely the effect is accounted for in peak broadening or jitter (causing a loss in resolving power). Additional effects arising from the non-linearity of the two clocks may be investigated in the future.

Investigation of rate effects on detection uncertainty

Dead time effects can occur at the ion detector itself, due to the ion signal, or from the speed of the DAQ system used. There is a period of time after the detection of an event where no event is recorded while the detector resets, typically recharging depleted areas. This alters the peak shape by increasing the FWHM since no counts are added during this period.

Using the isotope pair of $^{39}K^{+}$ and $^{41}K^{+}$ (93.3% and 6.7% natural abundance, respectively) the maximum detectable rate can be studied. The intensity of the ions within the system was increased until dead time effects are observed. To enhance the effect, the measurement was performed at a minimum number of turns (not to maximise resolution), resulting in a TOF peak width of approximately 4-5 ns for $^{39}K^{+}$. In figure 4.4, at a rate of 2 $^{39}K^{+}$ ions per

cycle, the abundance of $^{41}K^+$ increases. This occurs because the $^{39}K^+$ is now in dead time due to pile-up, but the $^{41}K^+$ peak (due to the lower abundance) can still be detected. Thus, in this example, about 2 $^{39}K^+$ ions per cycle can be detected. Additionally, as a result of the study the ideal rate is identified as less than 1 cpc. Dead time effects do not contribute to uncertainties in the mass values in this study as the rate was kept below 1 cpc.

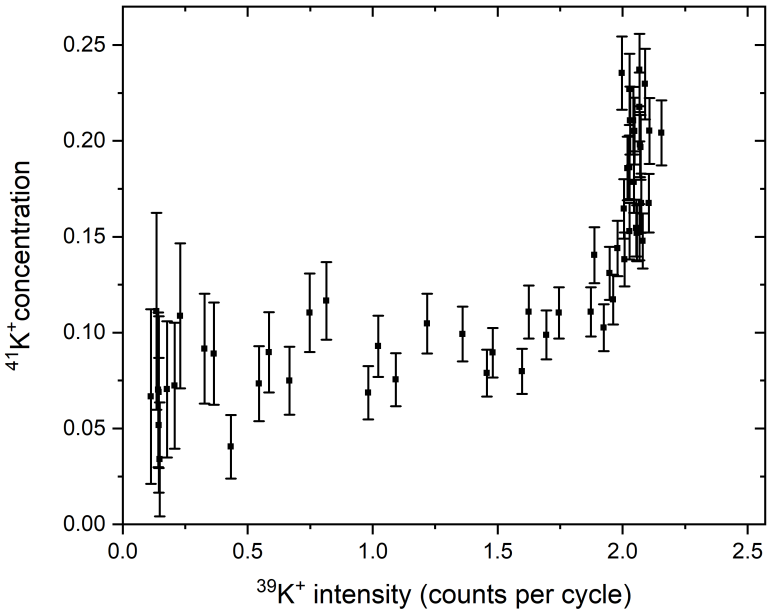

Figure 4.4: A plot showing increasing intensity of $^{39}K^+$ ions until the peak enters dead time at approximately 2 counts per cycle, where only the counts of $^{41}K^+$ ions can then increase.

4.3 Mass analysis procedure

Uncertainty of the calibration parameters Δt_0, Δb and Δc

The mass of the ions is determined by equation 3.11, which includes calibration parameters t_0, c and b. t_0 accounts for the offset from the time when the ions are triggered to be injected into the trap and when they actually enter the trap, plus delays in the data acquisition. c, defined in equation 3.9, depends on the kinetic energy and path-length of the ions (not including the IT). b is used for scaling to multiple turns as in equation 3.10. Parameters t_0, c and b are determined offline from a pair (or more) of stable calibrants prior to the experiment. These calibrant masses are well-known, and typically from the internal ion source. Using at least two well-known peaks, the parameter is identified and the uncertainty is determined [73]. If IOI and calibrant undergo the same number (the calibrant is an isobar) of turns then $\Delta c = 0$.

Uncertainty in the time-resolved calibration (TRC)

The TOF of a particular species may vary throughout the experiment due to fluctuations in the power supplies of the electrodes which form the ion mirrors. The drifts of the power supplies over the course of the measurement can be compensated with a time-resolved calibration (TRC) applied to a TOF spectrum. This is a procedure using a dynamic feedback algorithm based on identifying and fitting a peak in the spectrum over a longer range in time.

An identified peak of ions accumulated over 200 counts, with a known number of turns, preferably isolated in the spectrum (not overlapping with another species) is chosen as a TRC calibrant. The mass-to-charge value and FWHM of this calibrant in the initial spectrum of the measurement is used to set the searching range for the calibrant peak across the selected portion of the data file. An optimum 'block size' is selected to define the number of spectra to be summed across the TRC which depends on the incoming rate of the calibrant ion and IOI. The TRC compensates for power supply drifts by assuming the IOI and the calibrant ion experience the same fields, as demonstrated in figure 4.5 showing a 4 hour off-line measurement of $^{133}Cs^{+}$ ions with an initial calibration plus a TRC. Resolution of the peak before TRC is 80,000 and 200,000 after.

The error on the TRC, given by equation 4.1, depends on the statistics of the chosen calibrant in each block, the drift that occurs between the blocks A_{TRC} and the total number of blocks N_{TRC}.

$$\sigma_{TRC} = \frac{A_{TRC}}{\sqrt{N_{TRC}}} \left(\frac{m}{q}\right)_{IOI} \tag{4.1}$$

For the ideal case where the calibrant ion is delivered at a rate of 1 cpc (about 50 pps detected) the uncertainty on the TRC is $dm/m \leq 1 \times 10^{-8}$. Should the calibrant ion have a lower rate, the TRC is less effective which is reflected in a non-ideal peak shape (larger FWHM) and lower resolving power. This in turn makes peak fitting more difficult and is associated with a greater uncertainty. For the results shown in this work maximal TRC uncertainties of $dm/m \leq 3 \times 10^{-7}$ were observed.

Uncertainty in the peak shape

The peak shape in the spectra of MR-TOF-MS has evolved since commissioning in 2017. Initial spectra were more Lorentz-like, and now the peak shape is Gaussian with tails to the left and right. These tails originate from the tuning of the analyser voltages, which has been altered over time, and as a result the peak shape has evolved. Under ideal conditions, the peak shape in a MR-TOF-MS spectrum is identical for all species, and hence independent of the mass itself. An appropriate peak shape can be selected for all peaks in a given spectrum which adequately describes the peak shape, and enables a centroid value of the m/q to be obtained. The chosen peak shape is fitted on a calibrant peak, to find the peak width which is proportional to the m/q of the ion, then applied to all other peaks.

Through testing peak fittings of Gaussian, inverse polynomial, Lorentz and hyper-Exponentially Modified Gaussian (Hyper-EMG, which combines a Gaussian centre with exponential tails [73]), see figure 4.6, the best describing characterisation is Hyper-EMG. However, in this study the IOI were mostly well separated from other peaks in the spectra and so, for ease and speed, a Gaussian fit suffices. Uncertainty from the fitting of a Gaussian fit to an well-separated IOI peak gives an uncertainty contribution on the order of $dm/m \leq 9 \times 10^{-8}$ for the masses discussed in section 4.4.

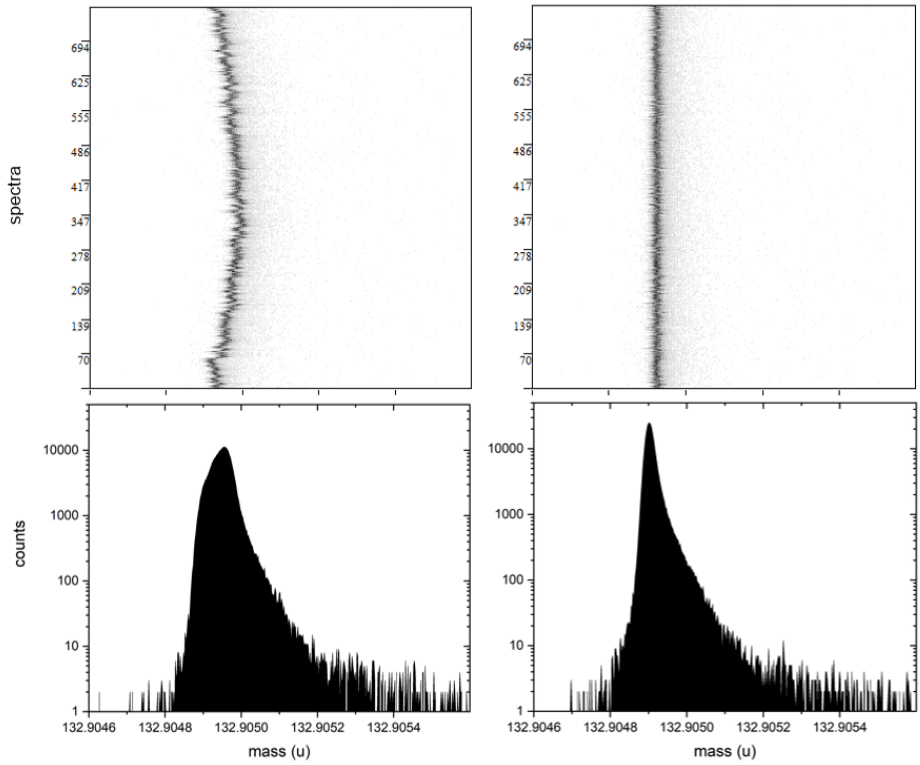

Figure 4.5: Example of a TRC correcting for peak drifts in a 4 hour spectrum of $^{133}Cs^{+}$ ions undergoing 321 turns. Graphs show the mass-to-charge spectra pre-TRC (left) and post-TRC (right). The top panels show the drift of the peak from spectrum to spectrum. The bottom panels show the summed mass-to-charge spectra and therefore the resulting mass peak.

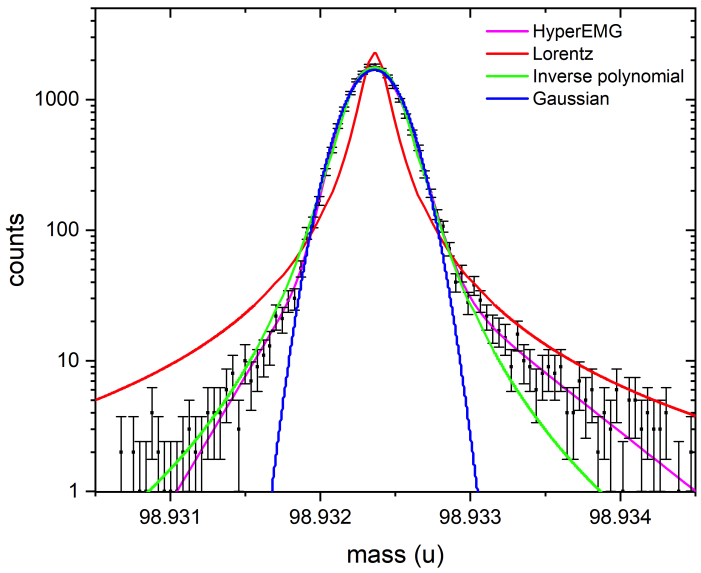

Figure 4.6: Comparison of Hyper-EMG, Lorentz, inverse polynomial and Gaussian peak shapes on a typical MR-TOF-MS spectrum peak.

Uncertainty in overlapping peaks

Peaks in the spectrum of the MR-TOF-MS are not always well-separated and may overlap depending on the mass resolving power of the system, number of turns and closeness in mass. If the overlap of peaks is minimal then fitting is trivial and a Gaussian fit is sufficient. If peaks overlap to a greater degree the fitting becomes more complex as the centroids and widths of the peaks become convoluted. A common example is fitting of both the ground state and an isomer of the same species, due to biasing of the fit results towards the centre of the two peaks because the A/q is so similar, the two peaks are indistinguishable. Analysis for these overlapping peaks has a limit where they are unresolveable from each other.

Investigations using a typical TITAN MR-TOF-MS peak were carried out and found it is possible to fit peaks separated by a minimum of approximately 3 FWHM, as shown in figure 4.7. On the x-axis is relative peak deviation (Δm/FWHM, shown in MeV on the top axis) which is how much two peaks are separated by. Shown on the y-axis is relative deviation between the actual (applied) separation of two peaks and the separation as a result of the Gaussian fit. Results from data using two peaks with identical intensity are shown in blue, an intensity ratio of 1:5 (one peak is five times greater than the other) are shown in green, and a difference in intensity of 1:10 shown in red.

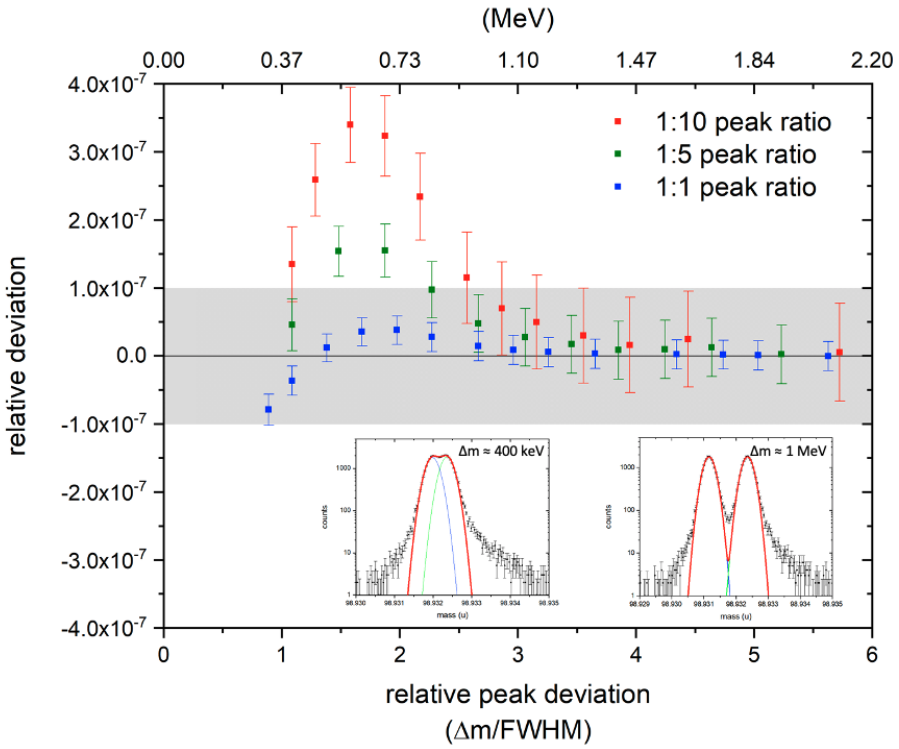

Figure 4.7: This graph shows how the actual (applied) separation between the two peaks is detected by the fit. Inserts show examples of fitting species separated by approximately 400 keV (left) and 1 MeV (right) at 99u. See text for details.

The relative deviation decreases as the relative peak deviation increases, since the separate

peak centroids are easier to distinguish and fit. The studies with one more dominant peak shows the relative deviation is greater due to the the fitting algorithm skewing the fit to one particular peak. These investigations found it is possible to fit peaks separated by a minimum energy of approximately 300 keV at 99 u, indicating a minimum relative separation of $dm/m = 3 \times 10^{-6}$ is required to distinguish species of the same mass. The contribution to the uncertainty is on the order of $dm/m \leq 1 \times 10^{-7}$ when the peaks are separated by 3 FWHM, beyond this limit the peak fitting is compromised. Typical mass resolving power of 200,000 enables peaks within ≤30 keV of each other to be separated with masses around A∼100 u.

Uncertainties during the mass calibration

The mass calibration, used to determine the mass value of the IOI using another calibrant mass in the spectrum, has an uncertainty composed of multiple parts. Firstly the statistical uncertainty of the chosen calibrant, error in the fit of the calibrant peak, as well as the uncertainty in the literature mass value of the calibrant ion, as given by equation 4.2.

$$\left(\frac{dm}{m}\right)_{calib} = \sqrt{\left(\frac{dm}{m}\right)^2_{STAT} + \left(\frac{dm}{m}\right)^2_{FIT} + \left(\frac{dm}{m}\right)^2_{LIT}} \tag{4.2}$$

The statistical uncertainty of a mass value deduced from detected counts which form a Gaussian distribution is given by equation 4.3

$$\sigma_{stat} = A_{STAT}\frac{FWHM}{\sqrt{N}} \tag{4.3}$$

where $A_{STAT} = 0.424$, FWHM is the FWHM of the calibrant peak, and N is the number of counts in the peak. Uncertainty from the fit is from the fitting of a Gaussian peak to the calibrant peak. The uncertainty from the literature value was taken from the AME2016 [8] uncertainty.

An ideal calibrant is one of high abundance in the spectrum, preferably not significantly overlapping with other species, which is usually close to stability (or stable) and therefore has a well-measured mass with a small relative uncertainty, and no isomers. This is typically on the order of $dm/m \sim 1 \times 10^{-7}$.

For example, in chapter 5 of this thesis, the calibrant used at 54u was $^{54}Cr^{+}$. The literature uncertainty from the AME2016 [8] is 3.78×10^{-7} u, statistical uncertainty of the peak is 1.98×10^{-7} and the fit uncertainty from the Gaussian fit is 2.19×10^{-7} u. Using equation 4.2, the relative uncertainty of $^{54}Cr^{+}$ as a calibrant is $dm/m = 4.8 \times 10^{-7}$.

4.4 Uncertainties stemming from using non-isobaric calibrant ions

For the data presented in chapter 5, isobaric calibrants were used at all mass units. However, during other analyses, there are cases where a suitable isobaric calibrant peak is difficult to identify. A substantial peak for calibration, with minimal overlap with other species, that already has a well measured and accepted mass, is needed. Ideally stable ions from the internal MR-TOF-MS ion source are used as calibrants however these ions are, in most cases, non-isobars of the IOI and undergo a different number of turns within the

system, which may lead to a different experience of fields and hence increased uncertainty. The magnitude of this effect has been investigated.

A study across experimental data taken in 2017 and 2018 with the TITAN MR-TOF-MS has been performed in order to determine the uncertainty associated with using a stable non-isobar calibrant from the internal MR-TOF-MS ion source. The study covered more than 100 mass units in order to locate spectra containing stable non-isobar calibrants considering only peaks of well-measured species, containing approximately 200 counts or more, which do not overlap with neighbouring peaks which may alter the mass values calculated. For these measurements MRS was off, as the investigation used non-isobar calibrants, and hence this does not contribute to the uncertainty of these measurements. Masses are compared with AME2016 data [8]. Calibration of c and t_0 was performed according to table 4.1, high-resolution mass calibrants for b were either ^{39,41}K, ^{85,87}Rb or ^{133}Cs ions as documented in table 4.5, extending up to a mass difference of 36 AMU between calibrant and IOI.

Mass values from six TITAN RIB beam times from 2017 and 2018 were analysed using non-isobar calibrant ions, and the systematic uncertainties as described in this chapter were considered. The results are shown in figure 4.8 and presented in table 4.5. Results are given in terms of the mass excess (ME), defined by equation 4.4 where N is the number of neutrons, Z is the number of protons, $M(Z,N)$ is the mass of the nucleus, u is the nucleon unit mass based on 1/12 the mass of the ^{12}C atom, and A is the total number of nucleons.

$$ME(Z,N) = M(Z,N) - uA \tag{4.4}$$

Table 4.5: Mass excess (ME) as determined by the TITAN MR-TOF-MS using non-isobar calibrants. N_{IOI} and N_{CALIB} are the number of turns in the analyser for the species being measured and the calibrant ion, respectively. ME is in keV. Lines separate the measurement campaigns during which the masses were measured.

Species	Calibrant	N_{IOI}	N_{CALIB}	ME_{TITAN}
^{52}Cr	^{41}K	512	577	-55423(43)
^{52}Ti	^{41}K	512	577	-49473(41)
^{53}Cr	^{39}K	512	567	-55275(41)
^{53}Cr	^{41}K	512	582	-55266(41)
^{54}V	^{39}K	512	603	-49909(43)
^{54}V	^{41}K	512	588	-49910(43)
^{54}Cr	^{39}K	512	603	-56939(43)
^{54}Cr	^{41}K	512	588	-56940(43)
^{54}Mn	^{39}K	512	603	-55557(43)
^{54}Mn	^{41}K	512	588	-55558(43)
^{56}Cr	^{39}K	512	614	-56929(43)
^{56}Mn	^{39}K	512	614	-55295(44)
^{81}Ga	^{85}Rb	373	364	-57621(44)
^{81}Ga	^{87}Rb	373	360	-57605(45)
^{82}Ga	^{85}Rb	382	371	-52940(43)
^{82}Ga	^{87}Rb	382	375	-52924(44)
^{97}Rb	^{133}Cs	394	336	-58511(48)
^{99}Sr	^{133}Cs	390	336	-62523(49)
^{99}Rb	^{133}Cs	390	336	-51118(47)

^{100}Sr	^{133}Cs	396	343	-59803(49)
^{100}Rb	^{133}Cs	396	343	-46218(46)
^{101}Sr	^{133}Cs	394	343	-55298(48)
^{102}Sr	^{133}Cs	392	343	-52166(48)
^{106}Pd	^{133}Cs	398	355	-89924(58)
^{106}Ru	^{133}Cs	398	355	-86317(56)
^{106}In	^{133}Cs	398	355	-80607(56)
^{106}In	^{133}Cs	398	355	-80635(50)
^{107}In	^{133}Cs	395	345	-83551(51)
^{130}Xe	^{133}Cs	345	341	-89906(51)
^{149}Eu	^{133}Cs	324	343	-76441(61)
^{151}Eu	^{133}Cs	335	357	-74686(61)
^{152}Eu	^{133}Cs	332	355	-72899(61)
^{153}Eu	^{133}Cs	330	354	-73412(61)
^{153}Dy	^{133}Cs	330	354	-69168(61)
^{154}Eu	^{133}Cs	328	353	-71761(61)
^{154}Dy	^{133}Cs	328	353	-70422(60)
^{154}Yb	^{133}Cs	328	353	-49920(59)
^{155}Eu	^{133}Cs	326	352	-71856(61)
^{155}Dy	^{133}Cs	326	352	-69204(61)
^{155}Yb	^{133}Cs	326	352	-50516(59)
^{156}Yb	^{133}Cs	324	351	-53269(59)
^{157}Ho	^{133}Cs	323	351	-66872(44)
^{157}Er	^{133}Cs	324	351	-63470(44)
^{157}Tm	^{133}Cs	324	351	-58810(60)
^{157}Yb	^{133}Cs	324	351	-53503(59)

From the results shown in figure 4.8, the uncertainty stemming from using a non-isobar calibrant varies for each measurement campaign (shown in different colours). The inset in figure 4.8 shows the average deviation from literature is $dm/m = 8 \times 10^{-8}$ with a standard deviation of 2×10^{-7}. The slope is 6×10^{-9} per mass unit difference but can be significantly less depending on each effect discussed within this chapter and should be assessed for a given experimental campaign.

4.5 Summary

Sources of uncertainty in the TITAN MR-TOF-MS system have been studied, including effects originating within the analyser, at detection, and during the analysis procedure. The study of using non-isobaric calibrant ions reproduced mass values of species with average deviation of $dm/m = 8 \times 10^{-8}$ and associated standard deviation of 2×10^{-7}, compared with literature results. The approximate individual error contributions originating in the analyser and at detection are detailed in table 4.6, for using an isobar or non-isobar calibrant ion, given that the MR-TOF-MS was operated with a maximum of 1 ion detected per cycle to avoid space-charge and deadtime effects. Uncertainties in the mass analysis procedure are calculated separately for each individual beamtime analysis. From this study, and the calculation of

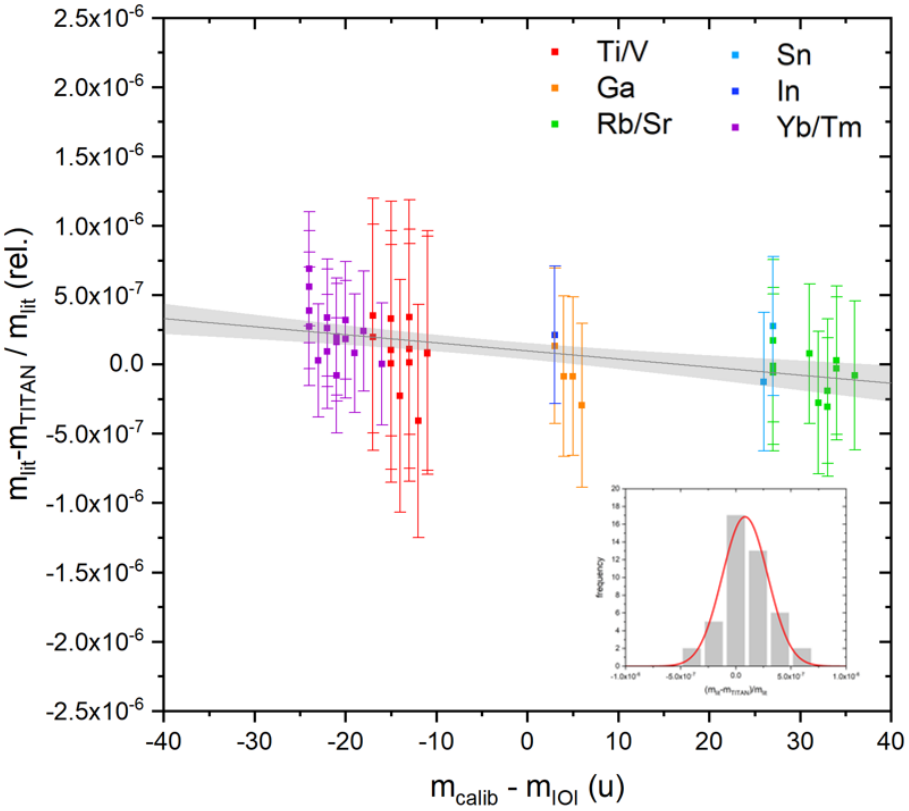

Figure 4.8: Deviation in mass value between TITAN and literature results from the use of non-isobar calibrants for multi-turn calibration as a function of mass difference between ion of interest and calibrant. Different colours indicate the experiment in which each data set was collected. The linear fit is shown as a black line with 95% confidence band in grey. Inset shows a histogram of the deviation from literature as a frequency count plot. The MR-TOF-MS shows an average deviation of $dm/m = 8 \times 10^{-8}$ and standard deviation 2×10^{-7}.

uncertainties contributing from the mass analysis procedure, a relative systematic uncertainty contribution to the mass measurements taken with the TITAN MR-TOF-MS presented in Chapter 5 can be determined to be $dm/m \leq 1.9 \times 10^{-7}$. The individual uncertainties from fitting, statistics, and the mass calibration, as well as the systematic uncertainty contribution, are presented in table 5.1.

During the year this study was conducted (2019), and the years since commissioning in 2017, numerous improvements have been made on the TITAN MR-TOF-MS system. The mass resolving power of the TITAN MR-TOF-MS is now consistently above R = 200,000. Isotopes observed between 2017-2020 are shown in figure 4.9, including a measurement of $^{125m}In^{+}$ with $t_{1/2} \sim 5$ ms, and at rates below 1 pps from the target. The future capabilities of the TITAN MR-TOF-MS are vast due to the unique setup of the TITAN facility which allows for a variety of precision mass measurements as well as other more diverse measurements. The TITAN MR-TOF-MS opens up the possibility to selectively 'retrap' a particular portion of ions [99] which can be applied to the TITAN MR-TOF-MS for mass measurement with reduced contamination, or to produce isobarically, and possibly even isomerically, pure beams for delivery to other systems.

Table 4.6: Maximum relative uncertainties deriving from the analyser and detection, for using isobar and non-isobar calibrants, provided the MR-TOF-MS was operated with a maximum of 1 ion detected per cycle.

	isobar	non-isobar
Uncertainty due to phase space in the injection trap	-	1.4×10^{-7}
Uncertainty from non-ideal mirror switching	7.4×10^{-8}	2.9×10^{-7}
Uncertainty due to space-charge in the analyser	-	-
Uncertainty due to the MRS	8.6×10^{-8}	0
Uncertainty due to instabilities of the timings	8×10^{-8}	8×10^{-8}
Investigation of rate effects on detection uncertainty	-	-

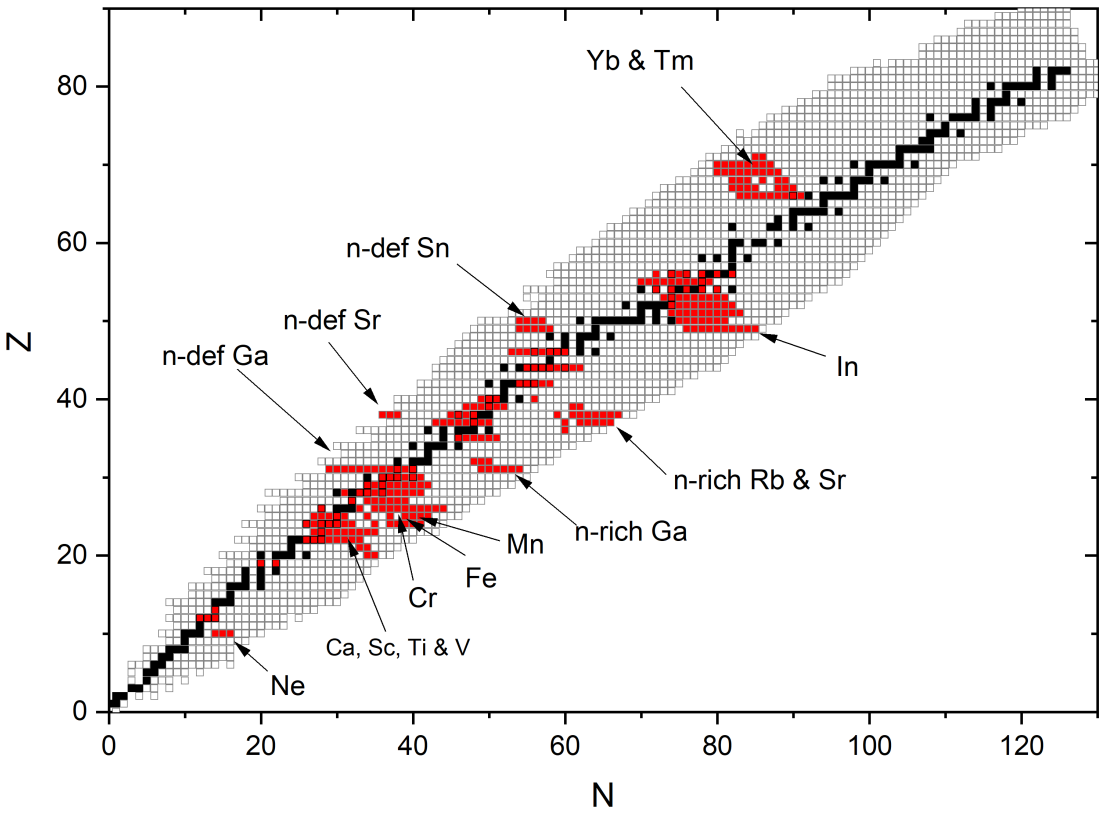

Figure 4.9: Chart of nuclides showing isotopes measured by the TITAN MR-TOF-MS from 2017-2020 in colour. Target isotopes for each measurement campaign are labelled.

Chapter 5

Exploring the emergence of the N=32,34 subshells for Z≥20

The discovery of magic isotopes, corresponding to particularly bound nuclei with specific numbers of neutrons or protons, led to the Nobel-prize winning nuclear shell model [115]. It is essentially analogous to the atomic shell model, where the neutrons and protons are filled into shells, and closed shells from at magic numbers which provide extra stability. The discovery in the 1960s was limited to stable or near stable species. Now, with access to radioactive species at RIB facilities, a larger range of isotopes has been investigated, and new phenomena have emerged. One of them is the evolution of shell closures in traditional magic numbers, which has been considered for a long time and the current status is reflected in detail in [116]. In particular, the study first mentions of magic-like behaviour in exotic nuclei at N=32,34, away from conventional shells at N=28 and 50. Signatures of magic behaviour in exotic nuclei are observed in trends of binding energies from mass measurements. Enhanced energy of the first excited states and reduced γ-ray transition probabilities are also 'hints' at, but do not directly indicate, nuclear shell effects. Shell closures near stability can be seen in charge radii measurements, though the same is not always observed far from stability [29]. Mounting evidence for traditional magic numbers evolving in cases with a large imbalance of protons and neutrons spur both experimentalists and theorists to work on understanding proton-neutron interactions.

Each nucleon experiences the potential V in the nucleus created by the other nucleons. This nuclear potential can be described by the Woods-Saxon potential, given in equation 5.1

$$V(r) = \frac{-V_0}{1 + exp[(r - R)/a]} \tag{5.1}$$

where $V(r)$ is the potential as a function of the distance r from the centre of the nucleus, V_0 is the potential well depth, R is the mean radius of the nucleus (given by $R = R_0 A^{1/3}$ where $R_0 \approx 1.2\ fm$ and A is the total number of nucleons) and a is the mean skin thickness (given by $a = 0.524\ fm$) [117]. The addition of the spin-orbit interaction further allowed predictions of the energy levels of the protons and neutrons. As seen in figure 5.1, the circled numbers correspond to magic numbers of protons and neutrons where nuclear shells form. Shell gaps are between these closed shells (indicated with double ended arrows) where the energy difference is larger. The notation of these orbitals, on the right, encompasses the principal quantum number n, the angular momentum (or orbital angular momentum) l which

gives the orbital (s (l=0), p (l=1), d (l=2), f (l=3), ...), and the total angular momentum $j = l + s$ which combines the orbital angular momentum and the nucleon spin s (protons and neutrons have $s = -1/2$ or $+1/2$ according to the Pauli principle). The degeneracy (maximum number of nucleons in a given level) is given by $(2j + 1)$. π and ν can sometimes be used to distinguish proton and neutron orbitals, respectively.

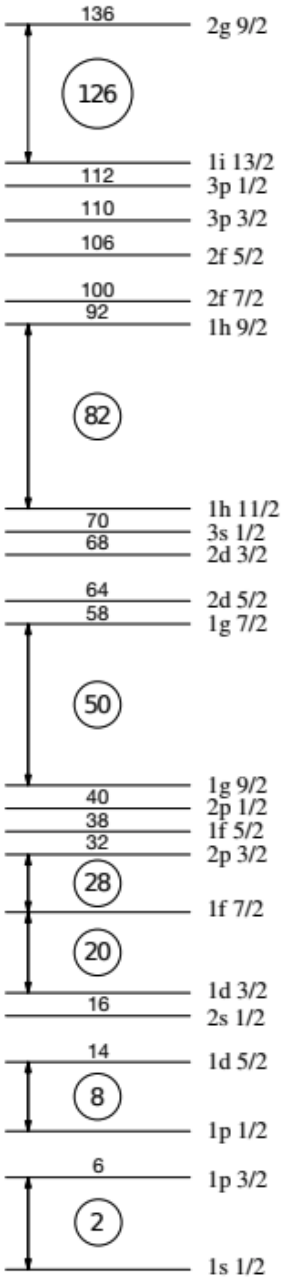

Figure 5.1: Shell structure showing cumulative number of nucleons with each closed shell, and the magic numbers which are circled. Double ended arrows indicate the shell gaps. Notation is shown on the right.

Protons and neutrons which each fill the energy levels seen in figure 5.1 interact with one another within the nucleus. Nucleon-nucleon interactions are governed by the strong (nuclear) force which has a finite range (on the order of fm) and is attractive, though on the very short scale (< 1 fm) it is repulsive. Proton-neutron interactions are known to change the relative energies of the neutron orbitals when protons are added or removed from the proton orbital [5]. In the N=32,34 region, the $\pi f_{7/2}$, $\nu p_{1/2}$ and $\nu f_{5/2}$ orbitals are the focus, as demonstrated in figure 5.2. In ^{60}Fe (Z=26, N=34) the proton-neutron interaction between the $\pi f_{7/2}$ and $\nu f_{5/2}$ is strong as indicated in the thickness of the arrow in figure 5.2. As protons are removed from the $\pi f_{7/2}$ orbital in ^{58}Cr (Z=24, N=34), the strength of the proton-neutron interaction decreases, and causes the energy of the $\nu f_{5/2}$ orbital to shift towards the $\nu p_{1/2}$ orbital. In the nucleus of ^{56}Ti (Z=22, N=34) there are two valence protons in the $\pi f_{7/2}$ shell (degeneracy $(2j+1) = 8$). The increased imbalance between proton and neutrons in the nucleus causes an energy level inversion of the $\nu p_{1/2}$ and $\nu f_{5/2}$ orbitals, and the neutrons instead fill the $\nu p_{1/2}$ level because of its relatively lower energy. The degeneracy of the $\nu p_{1/2}$ level is $(2j+1) = 2$ so it is completely occupied and a closed shell and magic effects begin to show. In ^{54}Ca (Z=20, N=34) both the proton and neutron shells are completely filled (closed). More comprehensive studies of these interactions and their role in structural evolution of the shell model require theoretical models and experimental data in the N=32,34 region to benchmark the models.

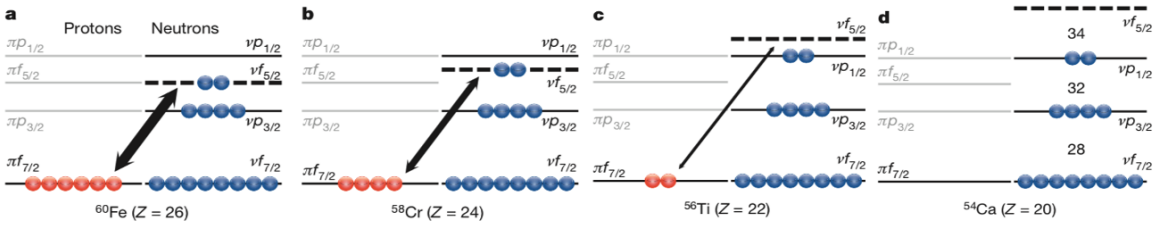

Figure 5.2: Schematic of the interaction between the $\pi f_{7/2}$ and $\nu f_{5/2}$ orbitals, as indicated by the thickness of the black arrow, for N=34. This figure is discussed in more detail in the text. Figure modified from [23].

Theoretical models correctly predicted shell closures at N=2,8,20 using established calculations of nucleon-nucleon (NN) forces, but these failed at N=28. The calculations focusing on NN interactions consider only the interaction of two nucleons and ignores all other nucleons in the nucleus. The introduction of three-nucleon (3N) forces in chiral effective field theory (EFT) [118] established that 3N forces depicted the repulsive interactions between two valence neutrons and an additional nucleon are essential in the explanation of the N=28 magic number. This identified the N=28 shell closure and the predicted double-magicity (magic in both N and Z) of ^{48}Ca. These studies also predicted N=32,34 shell closures, validating the results from the experimental γ-spectroscopy studies of Ti [22].

Calcium isotopes (with magic Z=20) play a key role in understanding nuclear structure at and beyond the N=28 region. TITAN mass spectrometry up to N=32 found ^{52}Ca to be 1.74 MeV (a value similar to the binding energy of the deuteron) more bound than previously determined [3], indicating unexpected magicity. This large deviation was subsequently confirmed at ISOLTRAP [4]. These first direct mass measurements identify the N=32 shell closure in Ca isotopes from the sharp decrease in S_{2N}, similar to the behaviour seen in doubly magic ^{48}Ca. Decay spectroscopy measurements of ^{54}Ca at RIKEN identify 'the onset of a sizeable subshell closure at neutron number 34' from the energy of the first 2+ excited state

of the nucleus E(2+) [23], see figure 5.3. The large E(2+) of ^{48}Ca indicates the strength of the shell closures at Z=20 and N=28, the classical magic numbers. E(2+) at N=32 is slightly lower and therefore indicates a slightly weaker subshell closure in ^{52}Ca, which is slightly weaker still at N=34 in ^{54}Ca.

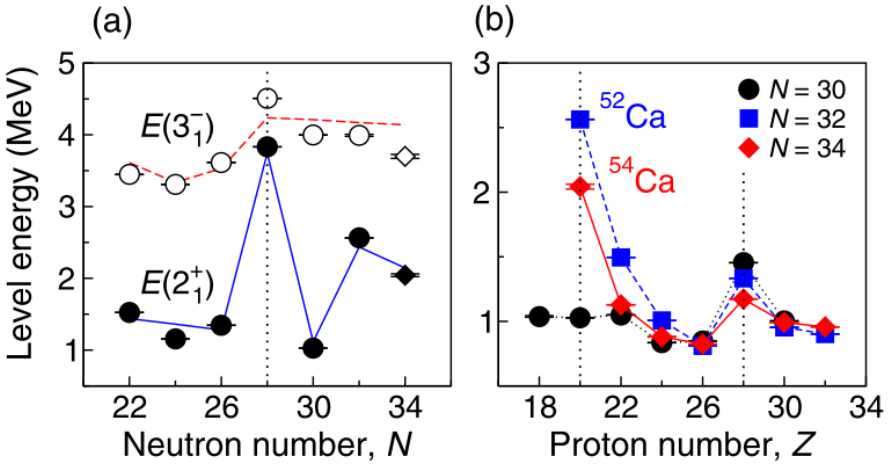

Figure 5.3: (a) Energies of the first 2^+ (and 3^-) states in Ca isotopes as a function of N. (b) energy of the first 2^+ state in N=30,32,34 isotonic chains as a function of Z. Figure modified from [5, 23].

3N forces employed in chiral EFT calculations have mapped the evolution of the shell structure of neutron-rich Ca isotopes towards the dripline [119]. These results confirmed the shell closure in ^{48}Ca due to the effects of 3N forces, with similar effects seen in ^{52}Ca, and a 'weak subshell closure' in ^{54}Ca. NN and 3N interactions work well in isotopes as heavy as O, but ab initio calculations are needed beyond this point. Ab initio (based on first principles, assuming that each nucleon is a point-like and non-relativistic particle) calculations have been performed for Ar, K, Ca, Sc, and Ti isotopic chains up to N=32 [120] to investigate off-shell (Z≠20) in surrounding non-doubly-magic nuclei.

To match theoretical predictions in the mid-shell region, the masses of neutron-rich $^{51-55}$Ti and $^{52-55}$V isotopes were determined at TITAN previously, where the N=32 shell closure effects were observed to weaken in Ti, and disappear in V [30, 31]. This work extends this effort into the Sc and Ca isotopic chains, and beyond N=34. Details of the experimental procedure are in section 5.1. The beam, contaminants and techniques used to reduce these are discussed in section 5.2. The data analysis procedure is discussed in section 5.3. The mass measurement, and half-life, results are presented in section 5.4. Finally, the results are discussed in section 5.6.

5.1 Experimental details

An ISAC RIB beam containing neutron-rich Ca, Sc, Ti and V isotopes was produced by impinging 480 MeV protons with 50 μA intensity onto a high-power Ta target. The TRILIS laser ion source [81, 82] was used to ionise Ti while all other elements were surface ionised.

The beam from ISAC was sent to TITAN with a transport energy of 20 keV. The TITAN RFQ accumulated the ions for 20 ms, cooling and bunching the ions, and a pulsed drift tube was employed to adjust the ion kinetic energy to 1.3 keV for operation with the MR-TOF-MS.

The TITAN MR-TOF-MS was operated on a 50 Hz duty cycle, synchronised with the RFQ cooling scheme. A new ion bunch was sent from the TITAN RFQ every 20 ms (corresponding to the time for one measurement cycle). After the pulsed beam entered the TITAN MR-TOF-MS, it was further cooled and bunched for about 13 ms in the trap section. The ions underwent 350-550 isochronous turns (IT) depending on the A/q ratio of the ions under investigation, resulting in flight times of around 7 ms. This corresponds to resolving powers of R = 180-200k. The number of ions was kept around 1 ion detected per cycle.

Total measurement efficiencies, including transport and detection, varied 10-30% depending on the species and its charge state. Efficiency of ions being detected was calculated from the measured rate of ions on a detector before the TITAN beamline, and again at the MagneTOF detector at the top of the MR-TOF-MS, see figures 3.5 and 3.7. The detected rate of the ions of interest ranged from approximately 0.01-1 pps. Large contributing factors to ion losses are residual gas interactions within the system (due to an imperfect vacuum), imperfect tuning and detector limitations. It was possible to measure nuclei further from stability than in previous measurements (beyond 55u, as in [30, 31]) due to the increased capabilities of the MR-TOF-MS as a result of system upgrades described in chapter 4. Overall, masses of species at 54-58u were measured with the TITAN MR-TOF-MS.

5.2 Beam properties

The beam delivered from ISAC was controlled in mass range by the mass separator magnet which is tuned (along with optics and slits) to the requested mass unit. However, because of the resolution R=2000-3000 the beam can contain a cocktail of isobars from the ISAC target and ion source. An example of the delivered beam is shown in the MR-TOF-MS spectrum in figure 5.4 and in the time-of-flight spectra for all beams which can be seen in the Appendix.

For all isotopes measured in this chapter, efforts were made to identify the constituent species in the beam. Vanadium isotopes were observed in all beams while calcium and scandium were detected up to A/q = 54 and 55 respectively. Titanium isotopes, found at A/q = 54-56, were additionally identified by measuring a spectrum with and without laser ionisation. The ionisation gain due to lasers was determined to be up to a factor of 10 for ^{54}Ti, and a factor 2 for ^{55}Ti as seen in figure 5.5.

The most abundant species at every mass unit were Cr^+, Mn^+, and Fe^+. Molecular contaminants like calcium oxide were observed. Also observed were doubly and triply charged contaminants. The 2+ and 3+ contaminants are most likely caused by the effect of 'backstreaming electrons' in the target. Electrons can be emitted from the so-called 'puller' and 'ground' electrodes near the target (either because of heating or radioactive decay), which can then be accelerated back into the target with enough energy (approx 20 kV) to ionise some species through electron-beam impact ionisation. These elements are then drawn from the target and some can pass through the mass separator magnet to be detected at the MR-TOF-MS. A discussion of all spectra and contaminants in detail are provided in the Appendix.

Contamination was reduced through three steps: first, by adjusting the ISAC mass separator magnet, the ratio of titanium to contamination was optimised. Secondly, the technique of collision induced dissociation (CID) [100], as described in section 3.5, uses increased gas

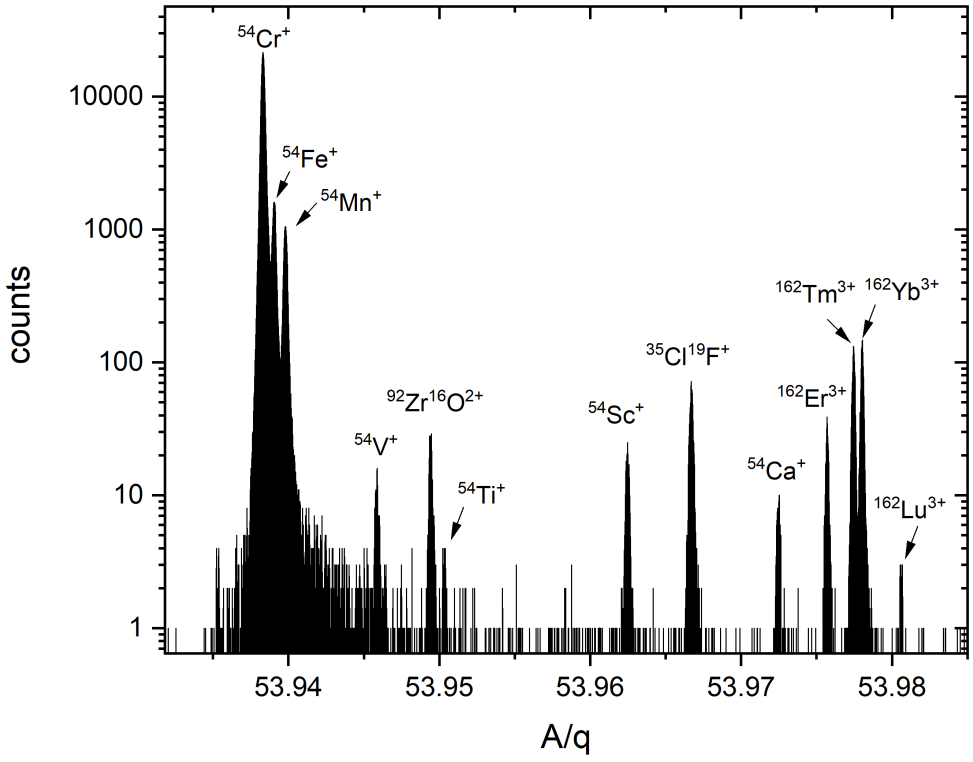

Figure 5.4: TITAN MR-TOF-MS spectrum at A/q = 54 where ions underwent 520 isochronous turns within the mass analyser. The most dominant species in the spectra are Cr^{+}, Mn^{+}, and Fe^{+}. The isotopes of interest V^{+}, Ti^{+}, Sc^{+} and Ca^{+}, have well separated but smaller peaks. Molecules of ZrO^{2+} and ClF^{+} are present in this beam, as well as Er^{3+}, Tm^{3+}, Yb^{3+} and Lu^{3+}. Resolving power was 210,000.

pressure to break-up molecular contaminants. The molecule fragments have different A/q ratios and can be separated. Finally, the technique of retrapping, described in section 3.5, selectively traps the IOI and is especially useful in cases where the IOI peak is close in mass to a dominant neighbour. This increases the probability to be selected for the IOI. The retrapping method was used for A/q = 55,56.

5.3 Data analysis procedure

Following the measurements, analysis of TITAN MR-TOF-MS spectra was done in various steps. The first is a time resolved calibration (TRC) to account for temperature drifts and fluctuations in the power supplies throughout the data collection. Peaks in the TOF distribution are considered Gaussian with asymmetric tails, due to energy spread of the ion bunches. The specific tail shape can depend on the tune of the analyser and hence the voltages applied. The centre of the peaks of interest were fitted with a Gaussian function, as shown in figure

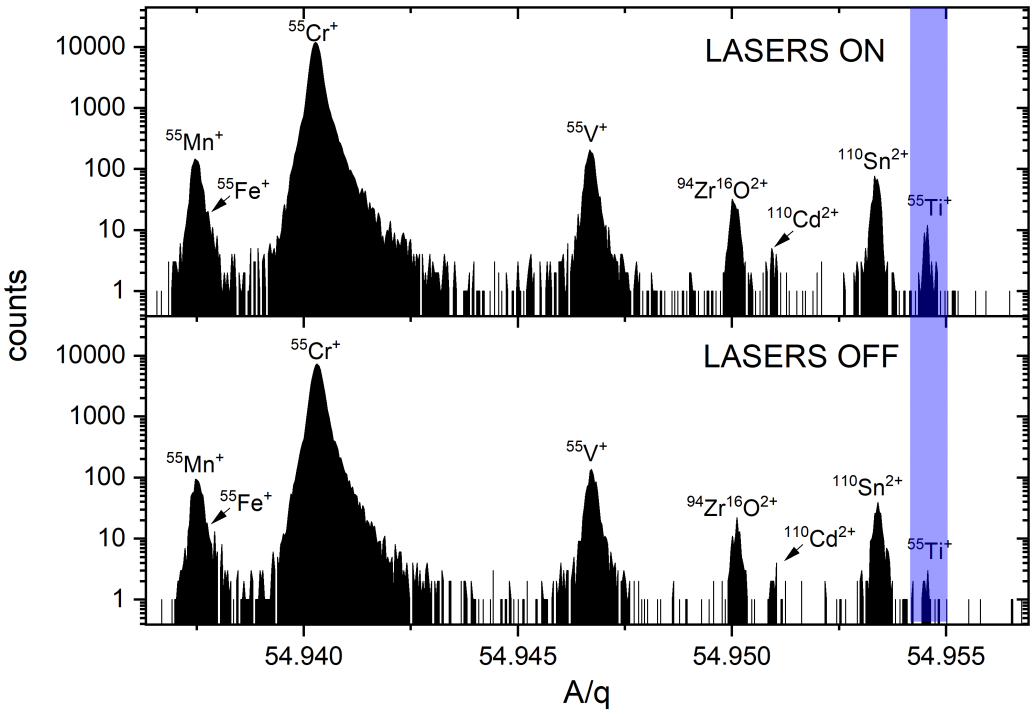

Figure 5.5: TITAN MR-TOF-MS spectra at A/q = 55 where ions underwent 350 isochronous turns within the mass analyser. Top panel shows a spectrum with active laser ionisation (lasers on), bottom panel shows with surface ionisation only (lasers off). A sizeable increase in the ^{55}Ti^{+} peak can be seen. Resolving power was 210,000.

5.6, and the centroid was identified. This allowed for a mass-calibration with a well-known calibrant ion, for example, in this work Cr^{+} for all mass units, except 58u where Fe^{+} was the calibrant.

The error on each mass value was calculated from a combination of the fit and statistical uncertainty (of a Gaussian), uncertainty from the mass calibration (including the fit and statistical uncertainty of the chosen calibrant, and the uncertainty in the literature mass value of the calibrant mass), and the relative systematic uncertainty contribution, detailed in chapter 4, of 1.9×10^{-7}. In table 5.1, the uncertainty from the IOI fit, IOI statistical uncertainty, uncertainty from the mass calibration, and the systematic uncertainty contribution are listed for each isotope measured. The uncertainties were added following error-propagation, resulting in uncertainties of 66 keV or less, as seen as the uncertainties in table 5.2.

All peaks in the spectra have been identified. To identify peaks, first, mass markers for all species with q=1 of the mass window under study are taken from AME2016 data. The remaining unidentified peaks can be tested with q=2^{+} or 3^{+} mass markers, or likely molecular contaminants. Molecular contaminants are first trialled with a combination of the stable isotope of the ion of interest, or neighbouring elements, plus H^{+}, O^{+}, C^{+}, F^{+}, OH^{+}, etc. Research prior to the experiment into the AME value and previous measurement methods of isotopes is performed to ensure the range for the mass peak is covered by the study.

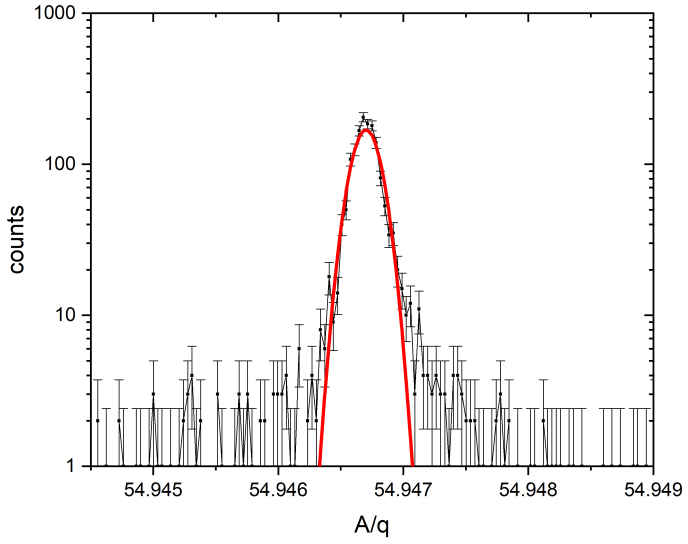

Figure 5.6: Example of a TOF spectrum fit with a Gaussian function (red) for ^{55}V, where ions underwent 350 isochronous turns and resolving power was 210,000.

Table 5.1: Error values (in keV) from each contributing factor for each isotope measured by the TITAN MR-TOF-MS in this work.

Species	Fit error	Statistical error	Mass calibrant error	Systematic error	Total
^{54}Ca	12.87	11.31	0.46	9.55	20
^{54}Sc	7.40	6.02	0.45	9.55	14
^{55}Sc	56.54	24.59	0.81	9.69	62
^{54}Ti	31.07	17.85	0.45	9.55	37
^{55}Ti	13.04	18.63	0.57	9.69	25
^{56}Ti	13.71	21.37	4.14	9.90	28
^{54}V	11.49	9.69	0.46	9.55	18
^{55}V	1.54	2.93	0.57	9.72	10
^{56}V	2.95	8.25	3.44	9.90	14
^{57}V	2.79	6.29	1.89	10.08	12
^{58}V	54.88	35.57	1.21	10.26	66

5.4 Mass measurements of ^{54}Ca, $^{54-55}$Sc, $^{54-56}$Ti, and $^{54-58}$V

Table 5.2 summarises the mass measurement results of the experiment and compares them to recent literature values. These include the latest AME2016 measurements, prior TITAN measurements [30, 31], and the difference between AME2016 and this work. The AME evaluation procedure combines all measurements of a particular nucleus (direct and indirect) and produces a recommended mass value based on the evaluated information. This process has been done in regular intervals and is published [8, 121–125]. Here, the AME from 2016 is used to indicate the most recent publication. Results are given in terms of the

mass excess (ME), defined by equation 4.4. All individual spectra used for this analysis are presented in the Appendix. Here, a short summary of the individual mass units is given.

A/q = 54

This first time TITAN observation of ^{54}Ca is in agreement with the AME2016 value, within uncertainty, -30.6 keV different from the AME result. The AME value is based entirely on the only previous direct measurement of ^{54}Ca from ISOLTRAP [4] via MR-TOF mass spectrometry, as shown in figure 5.7. The TITAN value agrees very well within uncertainty and has a reduced error bar.

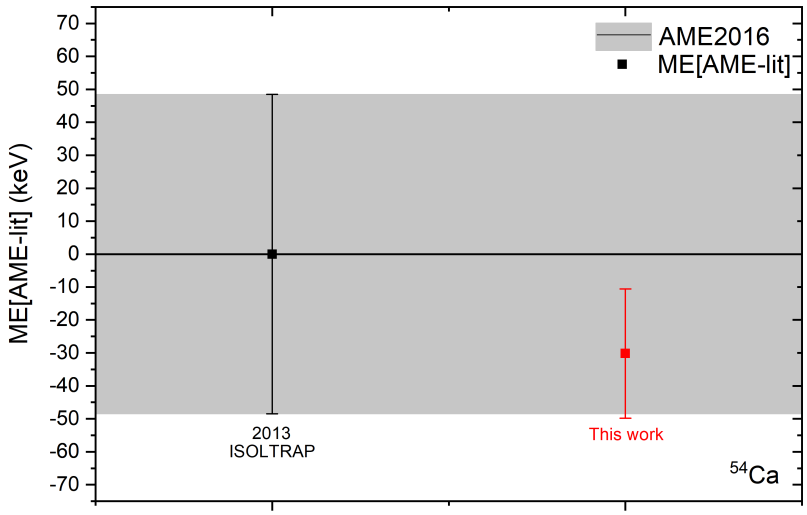

Figure 5.7: Comparison of ^{54}Ca ME values with the AME2016, from ISOLTRAP [4]. AME uncertainty is shown as a grey band. This work is shown in red.

The observation of ^{54}Sc is a first-time measurement of this isotope for TITAN. The AME combines results from Los Alamos measured using the TOFI method [10–12], a GSI TOF measurement [126], two NSCL TOF measurements [127, 128], and a CSRe result [129]. The weighting of these values in the AME evaluation is not even and the numerous measurements of ^{54}Sc are contradicting, see figure 5.8. Since the AME2016, there have been an updated value from CSRe [130] and NSCL [131].

Most of the measurements for the mass excess of ^{54}Sc seem to fall into two regions: one approximately -140-300 keV from the AME, and another 540-760 keV from the AME. The three results from Los Alamos vary around the AME value, with the GSI measurement agreeing with the two later studies. The 2011 and 2015 NSCL results agree with the first Los Alamos study, though the error bars do also reach into agreement with other data points. The 2020 re-evaluated result from NSCL takes their input closer to heavier ME measurements. The two CSRe results are close to the GSI and later Los Alamos results, and uncertainties overlap with the NSCL 2020 updated result. The 1998 TOFI and 2004 GSI measurements

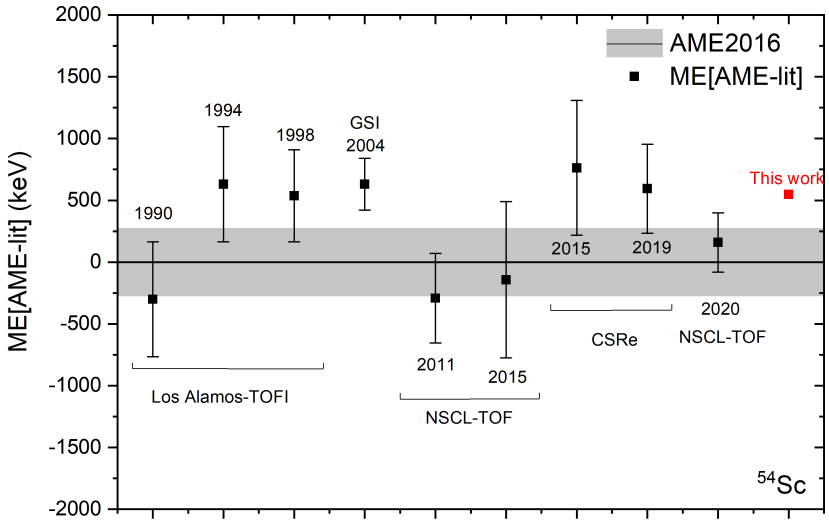

Figure 5.8: Measurements of the mass excess of ^{54}Sc compared with the AME2016 (uncertainty shown as grey band). Previous measurements from Los Alamos [10–12], GSI [126], NSCL [127, 128, 131], and CSRe [129, 130]. The result from this study is in red.

are of significantly lower weighting in the AME2016. Updated results from CSRe and NSCL, and the new result from TITAN, suggest the AME of ^{54}Sc may need reviewing.

The masses of ^{54}Sc from the 2011 and 2015 NSCL studies are heavier than other measurements included in the the AME2016. All 15 other masses published in the 2011 NSCL publication are systematically lighter than their corresponding AME values, except ^{54}Sc which is heavier than its corresponding AME value. The ^{53}Sc measurement from this paper is highlighted in the AME as disagreeing with other literature values. The 2015 NSCL study agrees with the previous measurement of ^{54}Sc from the same facility, but this time the other masses in the study are all systematically heavier than the AME2016. Additionally, the AME2016 places an extremely low weighting of the mass measurements of ^{52,53}Sc from this source. The 2020 re-evaluation of the ^{54}Sc is 400 keV different. The paper includes updated results for the other Sc isotopes which differ from the groups original values by up to 830 keV. Uncertainties from these papers, using this TOF technique, are 210 - 990 keV.

The TITAN measurement of ^{54}Sc is 547 keV from the AME2016 value, in agreement with CSRe, GSI, and the majority of the early TOFI measurements, outside of the uncertainty of the NSCL measurements. This new TITAN measurement supports the scepticism of the AME in the NSCL Sc data, and a diplomatic averaging of all measured values for future mass evaluations.

The numerous studies obtaining a value for the ME of ^{54}Ti are shown in figure 5.9. ^{54}Ti was also measured at TITAN in 2017, the difference between the two TITAN values is -8.89 keV: 113 keV different from the AME2016 value but in close agreement with each other. Previous measurements which are combined to form the AME value are time-of-flight isochronous (TOFI) spectrometer measurements from the 1990s at Los Alamos [10–

12], and an Isochronous Mass Spectrometry (IMS) measurement taken at the cooler storage ring (CSRe) in Lanzhou in 2015 [129]. Since the AME2016, there have been some revised results from the CSRe study, including ^{54}Ti [130]. There is also a β-decay measurement result [132]. The updated CSRe value is closer to the TITAN values than the initial result, both agree within uncertainty. The two TITAN MR-TOF-MS measurements, though lighter than previous measurements, are in close agreement, with the previous measurement having a lower uncertainty probably from statistics due the rate of Ti from the target. The new TITAN results agree within uncertainty with all prior measurements, with a reduced error bar, and an averaging of the current AME and TITAN results would be recommended for the mass evaluation of ^{54}Ti.

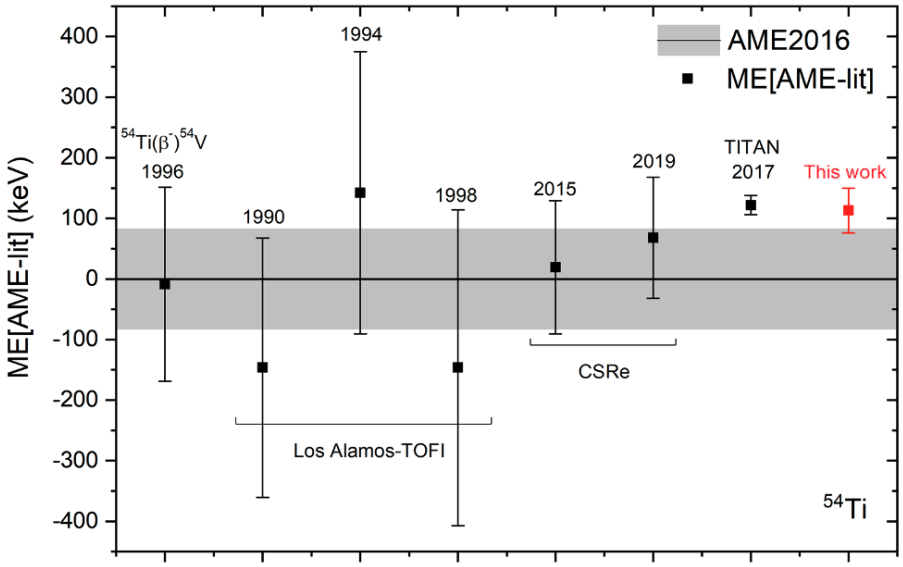

Figure 5.9: Comparison of all previous ^{54}Ti ME measurements, from decay studies [132], TOFI measurements [10–12], CSRe results [129, 130], the previous TITAN result [30], and this study (red). Measurements are shown as their deviation from the AME2016 value (uncertainty of which is demonstrated by the grey band).

^{54}V has only been directly measured once before, at TITAN [31]. All previous measurements are documented in figure 5.10. The two TITAN mass values measured in 2017 and 2019 agree within uncertainty with a difference between the measurements of only -7.7 keV. Prior to the 2017 TITAN measurement, the mass of ^{54}V was only measured indirectly [132–134]. The AME2016 value is weighted mostly on the 1977 measurement. The new measurement agrees very well with the AME2016 within uncertainty, the difference is a mere 3.11 keV. There is not much impact from this measurement except installing confidence in the measurements of the device. Given that the two TITAN data points are the only direct measurements and are in close agreement with one another, their weighting could be significant to a new mass evaluation of ^{54}V.

54u is a rich spectrum as retrapping was switched off and so all species in the 54u mass range are seen. The peaks of interest are all isolated in the spectrum reducing the uncertainty in the fit. The abundance of Ca^+, Sc^+ and V^+ are sufficient to have a confident fit. The

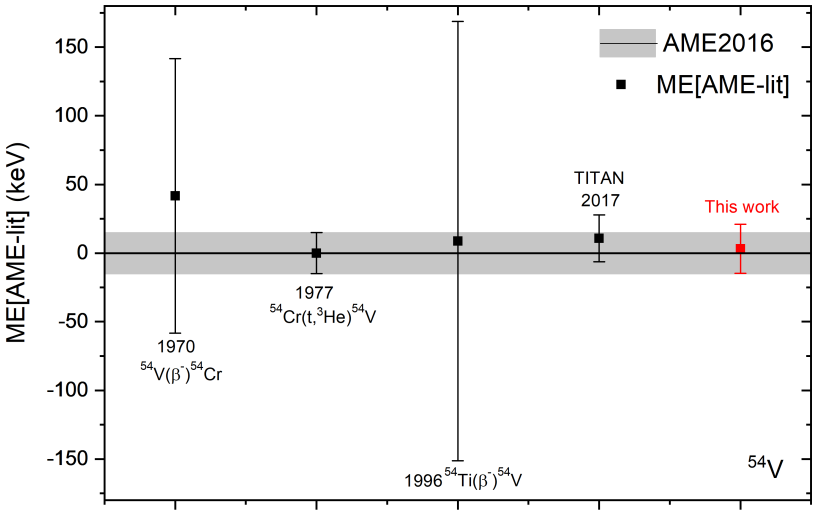

Figure 5.10: Comparison of ^{54}V mass excess (ME) values with AME2016. Previous indirect measurements [132–134], the previous TITAN measurement [31], the measurement from this study (shown in red), and AME2016 uncertainty shown in the grey band.

counts of ^{54}Ti are lower, but despite this the mass value agrees with the previous TITAN study.

A/q = 55

^{55}Sc was measured for the first time at TITAN. Previous mass measurements of ^{55}Sc which contribute to the AME value were obtained at Los Alamos via TOFI in the 1990s [10, 12], and more recently at NSCL [127, 128]. A re-evaluated figure recently came out from NSCL [131] which is not accounted for in the AME value. The TITAN value is 683 keV lighter than the AME value, but is in agreement with the 2020 NSCL data [131], and is within the error bars of the two other previous NSCL measurements [127, 128], shown in figure 5.11.

^{55}Ti and ^{55}V were measured at TITAN in 2017. In the cases of both ^{55}Ti and ^{55}V, the TITAN measurements agree within uncertainty. The uncertainties are reduced from the 2017 TITAN experiment. The TITAN 2019 measurement of ^{55}Ti is -11.9 keV different from the previous TITAN value and 152 keV from the AME2016 value. Previous ^{55}Ti mass measurements averaged for the AME value were performed via TOFI at Los Alamos in the 1990s [10–12]. There was also a β-decay measurement for ^{55}Ti [132]. As with ^{54}Ti, the TITAN values are lighter than the AME values, shown in figure 5.12, but are in close agreement with one another, and the recent NSCL measurement. Due to the close agreement between the recent and direct measurements, an average of these 3 values would be a good new evaluation of the mass of ^{55}Ti.

The mass difference from the previous TITAN value of ^{55}V is 5.1 keV, the first direct measurement of this isotope, and -14.46 keV from the AME2016 value. Previous ^{55}V ME

values are from decay measurements [132, 135], as shown in figure 5.13. All measurements agree within uncertainty, with the TITAN values significantly reducing error bars, and an averaging of all values would be appropriate.

The data taken at 55u shows multiple isolated peaks. Retrapping was switched on and thus reduces contaminants in the spectra.

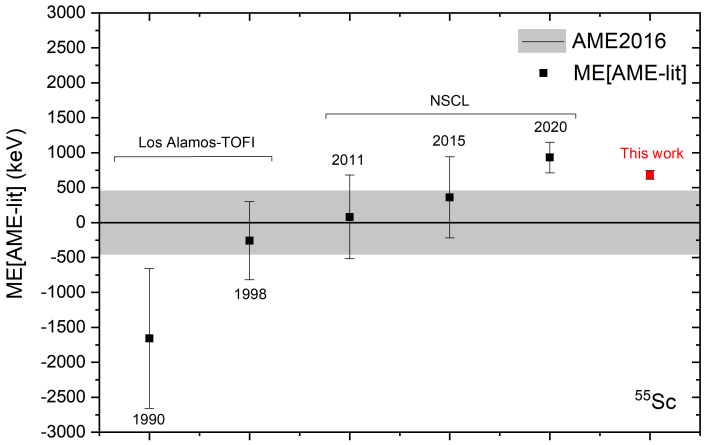

Figure 5.11: Comparison of ^{55}Sc mass excess measurements with the AME2016. Uncertainty of the AME2016 is shown in the grey band. Previous measurements are from TOFI [10, 12], and NSCL [127, 128, 131]. This work is shown in red.

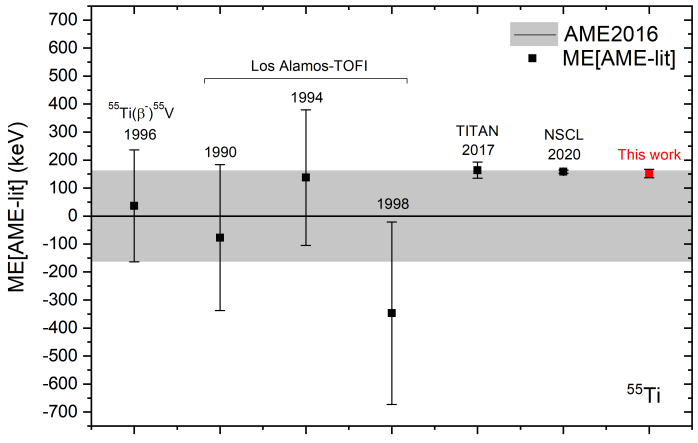

Figure 5.12: Mass excess value of ^{55}Ti compared with AME2016 (uncertainty displayed as grey band). Decay measurement [132], TOFI [10–12], a previous TITAN measurement [30], and a recent NSCL value are shown to compare with the value in this study (shown in red).

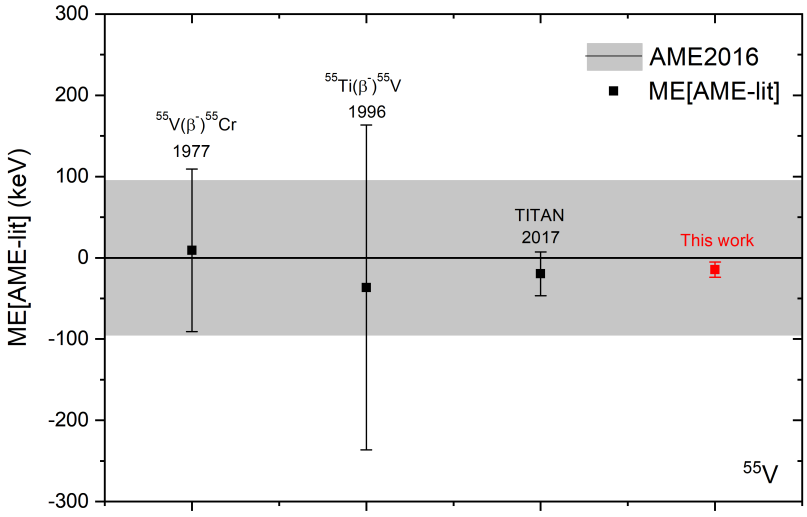

Figure 5.13: Measurement of the ^{55}V mass excess compared with the AME2016. Uncertainty of the AME2016 is shown in the grey band. Previous measurements are from decay spectroscopy studies [132, 135], and a previous TITAN measurement [31]. This work is shown in red.

A/q = 56

Mass 56 posed a challenge to obtain a measurement of ^{56}Ti due to it's extremely close proximity to CaO. The technique of collision induced dissociation (CID) [100] was used in an attempt to breakup some of the molecules in the system. A small distinguished peak of 22 counts of ^{56}Ti was used to obtain a mass value. The mass measurement obtained closely agrees with the AME2016 value, with 27.55 keV difference. The AME value is an average of the three Los Alamos TOFI papers [10–12], a TOF measurement taken at GSI [126], and a measurement from CSRe [129]. Since the AME2016, the CSRe has published updated results for ^{56}Ti [130], and a new measurement from NSCL has been published [131]. See figure 5.14 for all previous measurements, including an additional indirect measurement [132]. CSRe results from these studies are consistently lighter than the AME2016 and in this case lie outside the uncertainty band of both the AME and TITAN measurements. The TITAN measurement agrees with the AME, including the later TOFI and GSI 2004 measurements, within uncertainty and has significantly reduced error. The TITAN result should be included in future mass evaluations of the species.

^{56}V has never before been measured at TITAN. The AME value is an average of the three Los Alamos TOFI papers [10–12]. There is an additional previous measurement from decay studies [132]. The new mass value agrees with the AME2016 within uncertainty. The difference from the TITAN ME value to the AME value is 110.98 keV and with significantly decreased uncertainty, see figure 5.15. The recent NSCL measurement agrees with this study within uncertainty. The new measurement can be added to the averaging for determination of the mass of ^{56}V.

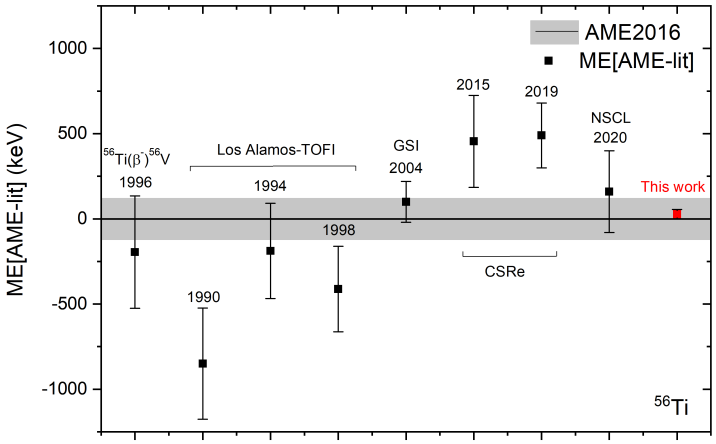

Figure 5.14: Comparison of ^{56}Ti measurements. AME2016 uncertainty is shown as the grey band. Previous measurements shown include decay spectroscopy [132], TOFI [10–12], a GSI measurement [126], CSRe values [129, 130], and an NSCL measurement [131]. The TITAN measurement is shown in red.

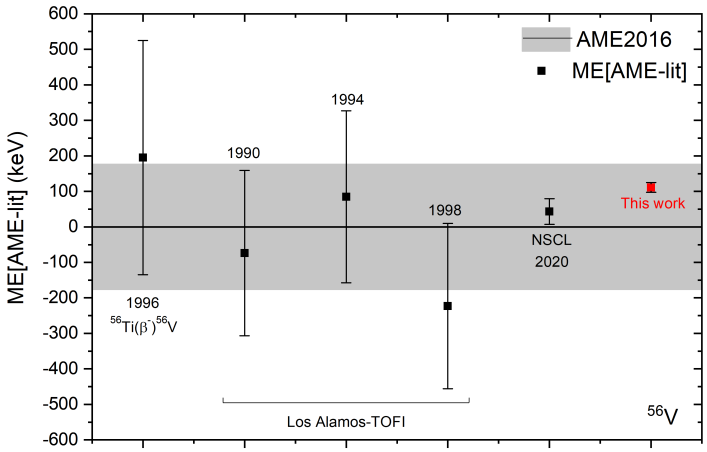

Figure 5.15: Comparison of ^{56}V mass excess values with AME2016 values. Uncertainty of the AME value is displayed as the grey band. This study is in red. Previous measurements are via decay [132] and TOFI [10–12]. There is an additional measurement from NSCL.

A/q = 57

This is the first time ^{57}V has been measured at TITAN. The AME value is a combination of three Los Alamos TOFI measurements [10–12] and a more recent CSRe experiment [129], see figure 5.16. There is very little weighting from the 1990 measurement in the AME2016, more from the others. There is also β-decay data from which a ME value is calculated [132], and a recent measurement from NSCL. The difference between the TITAN and AME values is -32.56 keV. These values are relatively close and this measurement has significantly reduced the uncertainty. ^{57}V is in the shoulder of the hugely abundant peak of Sn^{2+}, retrapping was used and sufficient separation was achieved. Due to the close agreement and low uncertainty of both the TITAN and NSCL measurements, an average of the these values is suggested.

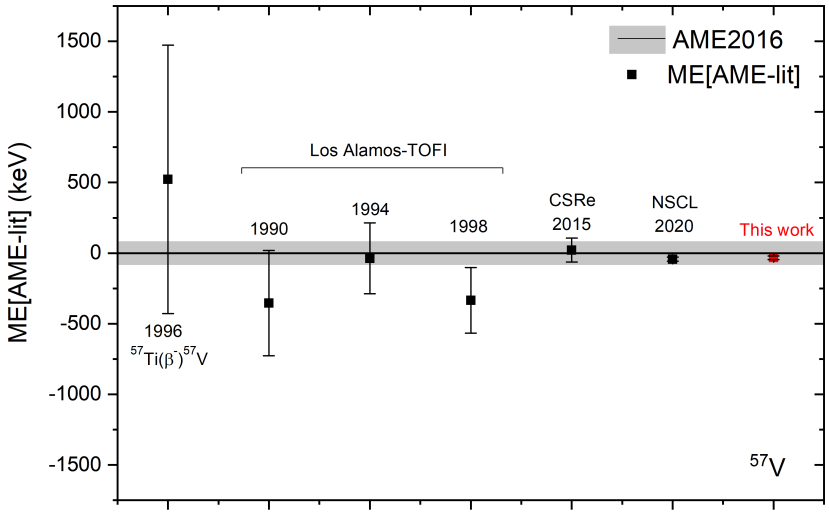

Figure 5.16: ^{57}V mass excess values compared with AME2016 (uncertainty shown as grey band) including a value from decay data [132], Los Alamos TOFI measurements [10–12], a CSRe measurement [129]. A recent NSCl measurement is included, as well as the current study (in red).

A/q = 58

9 counts of ^{58}V were observed by TITAN, these low statistics are reflected in the 66 keV error bar. The AME combines TOFI measurements taken at Los Alamos [10–12], a TOF measurement from GSI [126], and a CSRe result [129]. Figure 5.17 shows the previous measurements of ^{58}V and the TITAN 2019 measurement in red. Of the data taken at TITAN, the difference from the AME is -30 keV, with an uncertainty of 66 keV. 58u shows an isolated peak in a spectrum, but the rate of ^{58}V was extremely low. The TITAN mass of ^{58}V falls within the uncertainty of the AME2016.

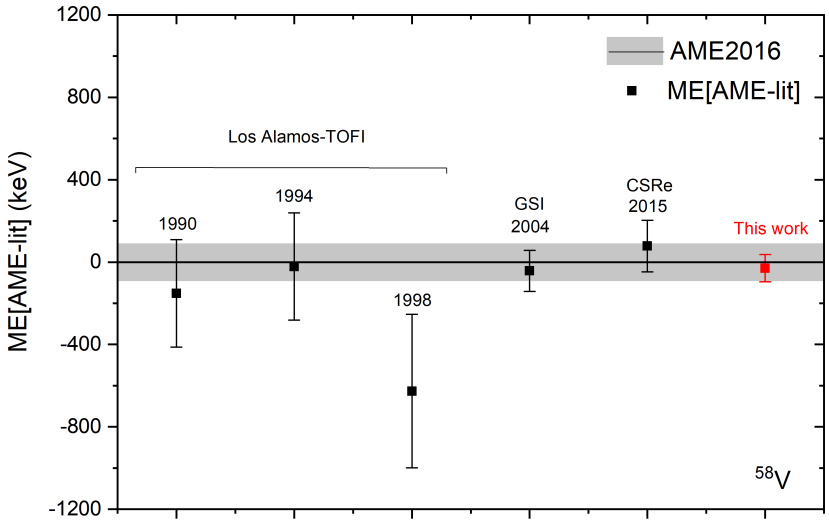

Figure 5.17: Comparison of ^{58}V mass excess results. AME2016 uncertainty is shown as grey band. Possibly mass excess value from the data in this thesis in red. Previous values from Los Alamos [10–12], GSI [126] and CSRe [129] are shown in black.

Summary

The TITAN measurement of ^{54}Ca is in agreement with the AME2016 value (based entirely on the only previous direct measurement of ^{54}Ca from ISOLTRAP [4]) with a greater than factor 2 reduced uncertainty of 20 keV. The TITAN measurement of ^{54}Sc is 547 keV lower than the AME2016 value. The AME evaluation of multiple experiments is not of even weighting and the numerous measurements of ^{54}Sc are contradicting. Since the AME2016, these results now have updated values from the Experimental Cooler-Storage Ring (CSRe) in Lanzhou [130] and the National Superconducting Cyclotron Laboratory (NSCL) at Michigan State University (MSU) [131]. For ^{54}Sc, the TITAN mass uncertainty was 14 keV, and hence much smaller than the previously reported uncertainties of 210-990 keV from all other studies. The TITAN measurement of ^{55}Sc is 683 keV lower than the AME2016 value. Since the AME2016, NSCL reevaluated their results [131] leading to a deviation of more than 200 keV from the previous values. The uncertainty for ^{55}Sc is 62 keV whereas uncertainties from other results are 220-1000 keV.

The measurements of ^{54,55}Ti are within one sigma of the previous TITAN measurements, and the AME2016 values, in agreement within uncertainty with all prior measurements and revised results from the CSRe [130] and NSCL [131]. The mass measurement of ^{56}Ti obtained is close to the AME2016 value and has significantly reduced error. The new measurements of ^{54,55}V agree very well with the previous TITAN measurements, and with the AME2016. ^{56,57}V mass values agrees with the AME2016 and the recent NSCL measurements [131] within uncertainty, with significantly decreased error. The mass measurement of ^{58}V falls within the uncertainty of the AME2016, though the rate of ^{58}V was extremely low.

Table 5.2: Mass excess values (in keV) for Ca, Sc, Ti and V isotopes measured by the TITAN MR-TOF-MS in this work, AME2016 values [8], previous TITAN measurements [30, 31], and the difference between the AME2016 and this work.

Species	$ME_{This\ work}$	$ME_{AME2016}$	$ME_{TITAN2018}$	$\Delta ME_{AME2016-This\ work}$
^{54}Ca	-25130(20)	-25161(48)		-31(51)
^{54}Sc	-34438(14)	-33891(273)		547(273)
^{55}Sc	-30842(62)	-30159(454)		683(458)
^{54}Ti	-45735(37)	-45622(82)	-45744(16)	113(90)
^{55}Ti	-41820(25)	-41668(162)	-41832(29)	152(163)
^{56}Ti	-39348(28)	-39320(121)		28(124)
^{54}V	-49896(18)	-49893(15)	-49904(17)	3(23)
^{55}V	-49130(10)	-49145(95)	-49125(27)	-15(96)
^{56}V	-46266(14)	-46155(177)		111(178)
^{57}V	-44381(12)	-44413(80)		-32(81)
^{58}V	-40372(66)	-40402(89)		-30(111)

5.5 Half-life measurements of $^{51-54}$Ti

Nuclear shell effects can manifest in nuclear observables other than mass, for example longer half-life, certain patterns in the excitation energies and nuclear charge radii [1]. Hence, another avenue to elucidate the N=32 subshell is via a detailed decay-spectroscopy study. Limited decay-spectroscopy of Ti isotopes was performed at the ISAC Yield Station [89]. The half-lives of the Ti isotopes were determined through β-counting and using the mscfit program [136], as shown in figure 5.18. A two-species fit method, where the abundance ratio is a floating parameter, was used for the analysis. Initial fit parameters for background, activity and half-life are inputs, which can be a value, range or free parameter. The half-life for ^{51}Sc (mother) and $^{52-54}$V (daughter) isotopes were taken from ENSDF [137], and the half-life and activity for Ti were fitted. All half-lives agreed with evaluated literature values [137], with the exception of ^{54}Ti; see table 5.3, a comparison is shown in figure 5.19.

Table 5.3: Half-live values (in s) of $^{51-54}$Ti isotopes measured by the ISAC Yield Station in this work, and literature values taken from ENSDF [137].

	$t_{1/2\ This\ work}$ (s)	$t_{1/2\ literature}$ (s)
^{51}Ti	337(45)	345.6(6)
^{52}Ti	102(11)	102(6)
^{53}Ti	32(3)	32.7(9)
^{54}Ti	9(1)	2.1(10)

The Evaluated Nuclear Structure Data File (ENSDF) [137] lists two half-lives for ^{54}Ti; 2.1(1.0) s [20] and 1.5(4) s [132]. Both deviate from the here presented measurement of 9(1) s by 6 sigma. The data collected at the Yield Station does not utilise γ-gating and uses a simple β-collection method so the observed 9(1) s lifetime cannot be unequivocally assigned to ^{54}Ti; however, circumstantial evidence supports the identification of the ^{54}Ti ground state. These include comparable yields measured at the Yield Station and the TITAN MR-TOF as well as

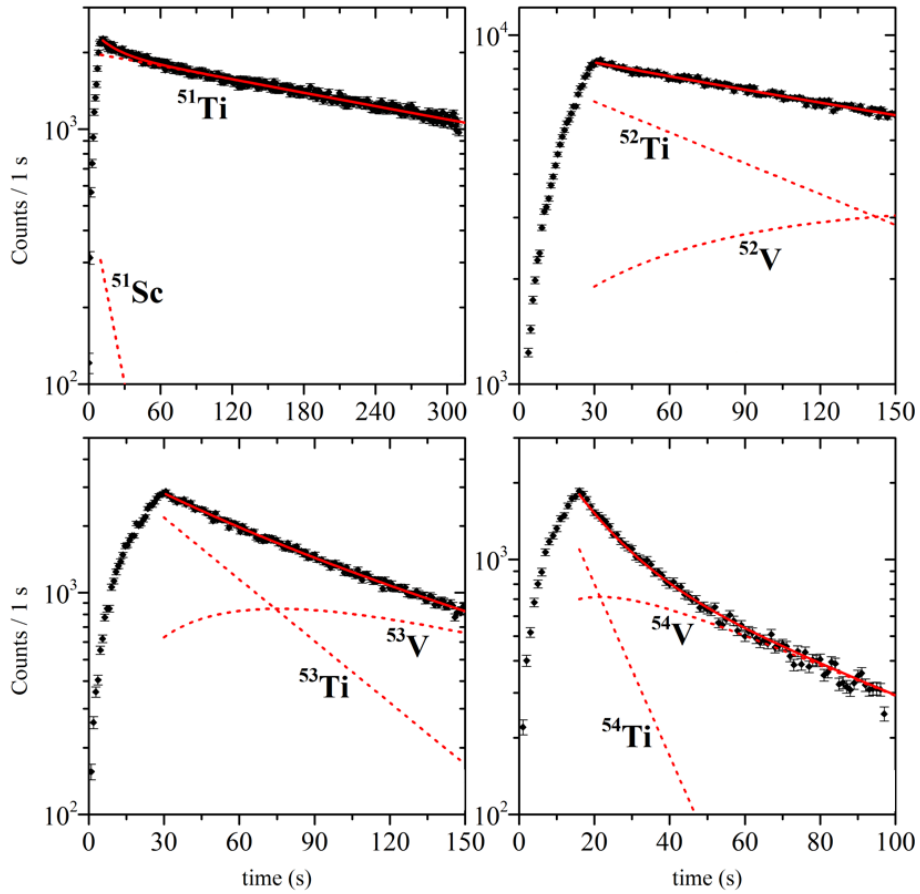

Figure 5.18: Example of decay spectroscopy data. Shown are fits of β-decay curves obtained using data from the ISAC yield station for $^{51-54}$Ti (black). The half-lives of ^{51}Sc and $^{52-54}$V are applied (red), and the fitting of ^{51}Ti was calculated from this decay information. All literature half-lives are taken from ENSDF [137]. All half-life values from the fitting procedure agree within error with published values with the exception of ^{54}Ti.

no other identified species possessing a half-life consistent with 9(1) s. Furthermore, a recent theoretical study into β-decay properties of Ca, Ti and Cr isotopes predicts the half-life of ^{54}Ti to be close to 10 seconds [138], in support of this work.

The half-lives (from ENDSF [137]) of isotopes in the region from N=28-37 are plotted for K, Ca, Sc, Ti, V and Cr in figure 5.20. Current published values of the Ti half-lives, and uncertainties, are shown in the blue band. A strong kink and large uncertainty is seen in the half-life of ^{54}Ti. The half-life value from this work, with significantly reduced uncertainty, supports the conclusions in [30] that Ti shows weak shell closure effects at N=32 from the longer half-life value. The disagreement not only draws scrutiny to the nuclide's half-life but also highlights the paucity of spectroscopic information in the region. A new, updated, and independent measurement could clarify the ^{54}Ti half-life and reduce uncertainty, contributing more data to the nature of N=32 in Ti isotopes, which could then be extended beyond N=32 and into other isotopes.

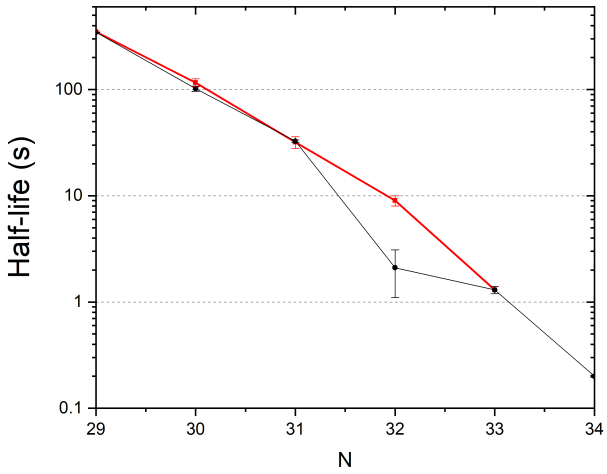

Figure 5.19: Half-lives of Ti isotopes as a function of neutron number (N). Literature [137] values are plotted in black, and this work is plotted in red. ^{54}Ti deviates from the literature values to form a smooth curve.

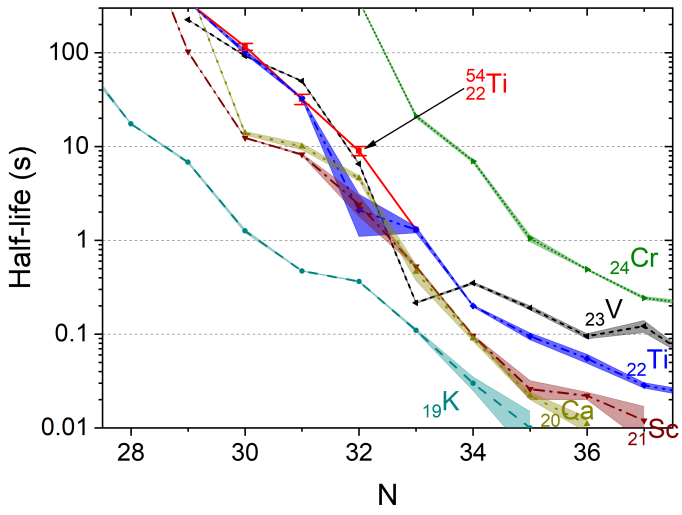

Figure 5.20: Half-lives as a function of neutron number (N) for K, Ca, Sc, Ti, V and Cr isotopes near the N = 32 shell closure. Uncertainties are shown as bands. Drastic differences in the literature values [137] (blue) and this work (red) of ^{54}Ti indicate more detailed studies are needed. Image modified from [31].

5.6 Magicity at N=32 & N=34

The mass values (or ME) in this work have uncertainties of 66 keV or less, significantly improving previous values by up to an order of magnitude. While most masses agree with the AME2016, deviations in the masses of ^{54,55}Sc ranged from 547-683 keV, which significantly impacts the interpretation of nuclear structure in this region around N=32. Alongside this work, mass measurements of $^{50-53}$Sc were recently performed at the LEBIT facility at NSCL [139].

The trends in two-neutron separation energy (S_{2N}), defined by equation 1.1, reveal interesting shell behaviour. For example, a drastic change in slope in S_{2N} values indicate a shell closure, while a flattening in S_{2N} points towards collective behaviour. The results of S_{2N} calculations performed on isotopes in this work are shown in a combined plot with neighbouring isotopic chains in 5.21, and separately in figure 5.22.

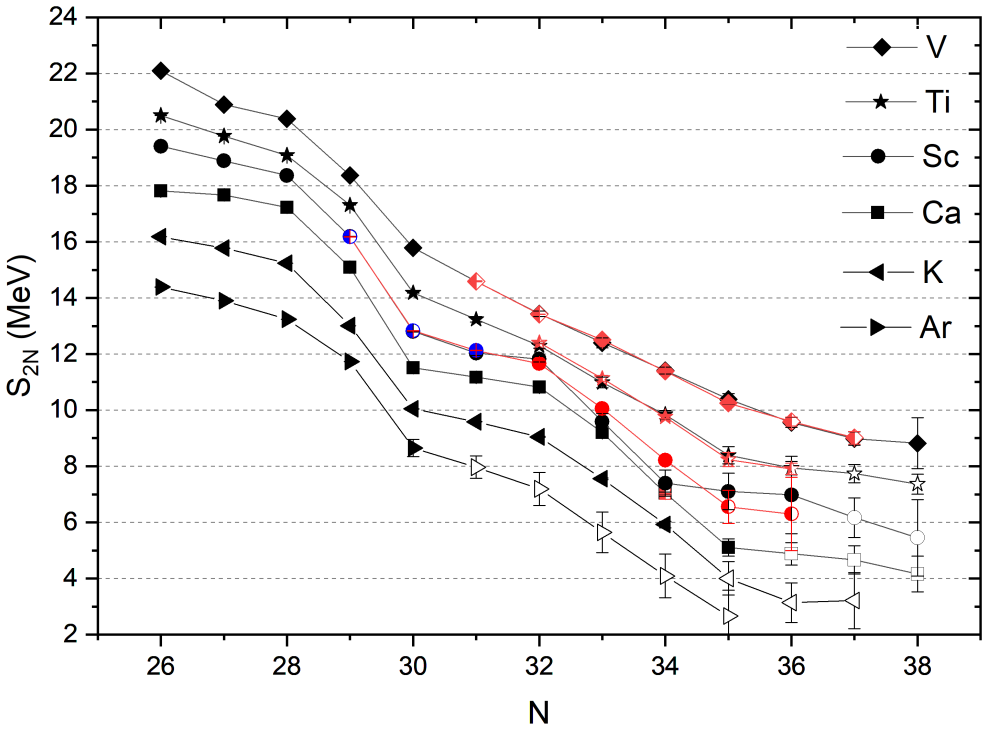

Figure 5.21: Summary plot of two-neutron separation energy (S_{2N}) of Ar, K, Ca, Sc, Ti and V isotopic chains plotted against neutron number (N). Data from AME2016 are in black, and data from this work are in red. Data from LEBIT [139] are in blue, experimentally measured values are in filled symbols, symbols which are half filled use a combination of AME and TITAN/LEBIT data, symbols which are entirely open are AME extrapolated values.

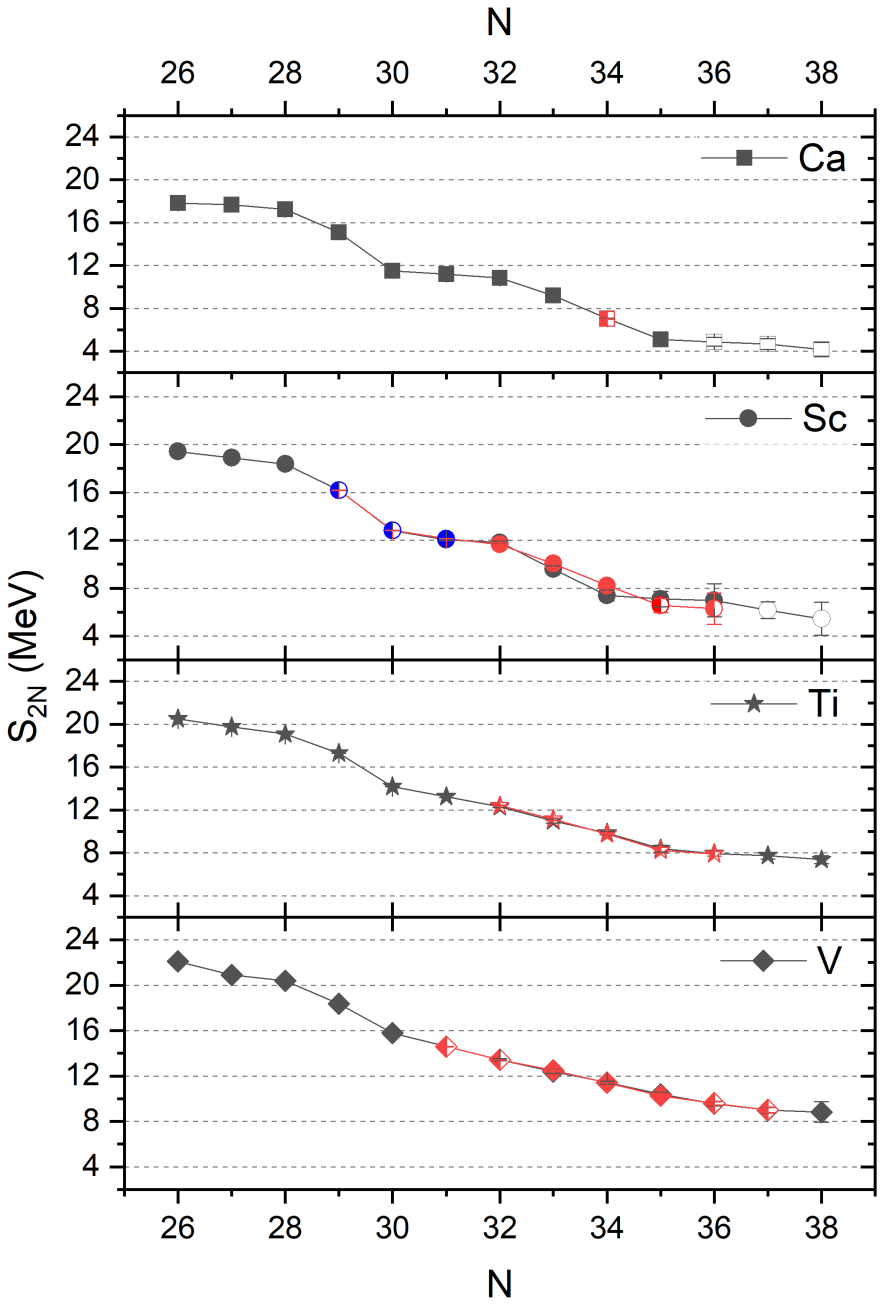

Figure 5.22: Two-neutron separation energy (S_{2N}) of Ca, Sc, Ti and V isotopic chains plotted against neutron number (N). Data from AME2016 are in black, and data from this work are in red. Data from LEBIT [139] are in blue, experimentally measured values are in filled symbols, symbols which are half filled use a combination of AME and TITAN/LEBIT data, symbols which are entirely open are AME extrapolated values.

Closed shell effects are revealed by a sudden change in the slope of two-neutron separation energy as shown for this region in figure 1.3. The well established closed shell effects at magic number N=28 can be seen as a downward slope after the shallow slope between N=20-28. Between N=30-32 the S_{2N} surface of Ca is flat once again, the abrupt change in slope of S_{2N} can be seen again at N=32 which flattens again around N=35.

As seen in figure 5.22, the S_{2N} for Ca isotopes after N=28 drops by approximately 2.1 MeV to N=29, and by 5.7 MeV to the next flat region at N=30. Similarly, after N=32 the change in S_{2N} is 1.6 MeV less to N=33 and 5.7 MeV to the next flat region at N=35. The N=28 and N=32 closed shells are of similar magnitude in Ca isotopes.

Sc, with one additional proton, shows remarkably similar neutron shell effects to Ca, both at N=28 and N=32 in figure 1.3 (data which is plotted in black in figures 5.22 and 5.21). The new data (in red) shows a significantly different S_{2N} surface than the AME2016 data in Sc isotopes at N=33,34. The deviations in S_{2N} values between the AME2016 and this work are 0.5-0.8 MeV for these two isotopes.

In this work, the S_{2N} of Sc isotopes from N=28 to N=29 decreases by 2.2 MeV, and to the plateau region at N=30 there a reduction of 5.5 MeV. From N=32 to N=33 the S_{2N} of Sc drops by 1.6 MeV, which is smaller than AME2016 data (2.2 MeV). From N=32 to the plateau region at N=35, there is a decrease in S_{2N} of 5.1 MeV, greater than the AME2016 (4.7 MeV). The N=32 subshell closure is of slightly smaller magnitude compared with the shell closure at N=28. The N=32 subshell closure from S_{2N} values is smaller in magnitude than in the AME2016. This indicates the effects are 'weaker' than previously thought. Compared with the Ca N=32 subshell closure, see figure 5.21, the change in S_{2N} is slightly less steep to the next plateau, supporting the argument of a slightly weaker subshell. The new data extends up to N=34 in Sc but more mass measurements of ^{56,57}Sc are needed.

The N=28 shell closure effects in Ti isotopes grow slightly weaker with the additional protons. S_{2N}, according to AME2016 data, decreases by 1.8 MeV from N=28-29, and 4.9 MeV N=28-30. The reduced shell effects are mirrored in the N=32 subshell closure, given by the reduction in S_{2N} of 1.3 MeV to N=33 (identical to the AME2016 value) and 4.1 MeV from N=32-35 (slightly greater than AME2016 value of 3.9 MeV). These changes in S_{2N} are smaller compared to Sc, and smaller still than Ca, indicating the doubly magic shell effects that are seen in Ca at N=28,32 weaken with greater Z.

The change in S_{2N} in V is similar to Ti from N=28-29 (2.0 MeV), though slightly smaller from N=28-30 (4.6 MeV). The changes in S_{2N} after N=32 are smaller in V than in Ti: a drop of 0.9 MeV to N=33 (similar to the AME2016 value of 1.0 MeV), and 3.2 MeV to N=35 (close to the AME2016 result of 3.0 MeV). The V S_{2N} surface demonstrates shell effects at traditional magic number N=28, but no such effect at N=32. The flat plateau region after N=35 seen in the data of Ca, Sc, and Ti is not seen in V isotopes, instead the gentle downwards slope continues. This could be an indication of a lack of N=32 subshell closure in V isotopes, or some effects around N=34. The summary plot of the S_{2N} isotopic chains is shown in figure 5.21, which illustrates the overall landscape for the isotopes between N=26 and N=38.

A 'derivative' of the two-neutron separation energy is the empirical neutron-shell gap (Δ_{2N}), as calculated by equation 5.2, which is often used to identify the magnitude of shell effects. Δ_{2N} results of isotopes in this work combined with LEBIT data [139] are shown in figure 5.23.

$$\Delta_{2N} = S_{2N}(N, Z) - S_{2N}(N + 2, Z) \tag{5.2}$$

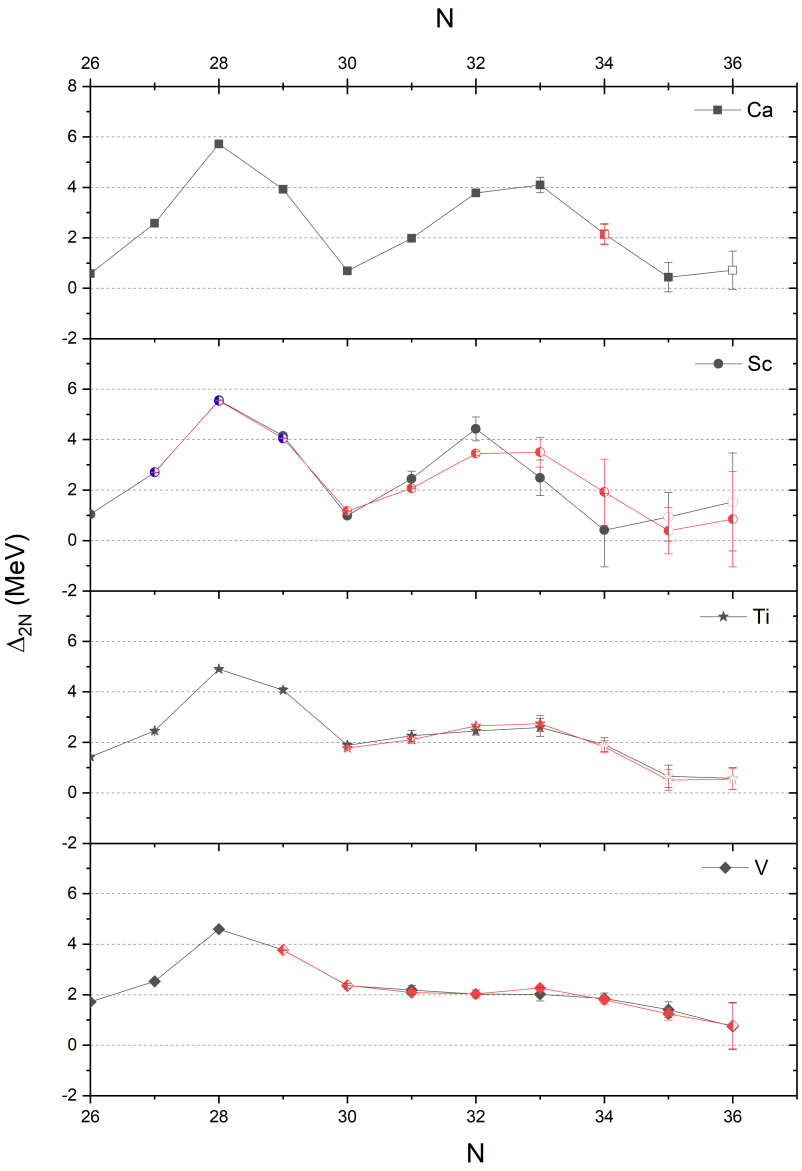

Figure 5.23: Empirical neutron-shell gap (Δ_{2N}) plotted against neutron number (N) for Ca, Sc, Ti and V isotopic chains. Data from AME2016 are in black, and data from this work are in red. Data from LEBIT [139] are in blue, experimentally measured values are in filled symbols, symbols which are half filled use a combination of AME and TITAN/LEBIT data, symbols which are entirely open are AME extrapolated values.

Strong shell effects at the classic magic number N=28 are seen in all isotopes in figure 5.23. In Ca, the Δ_{2N} peak at N=28 is around 6 MeV, which drops close to zero at N=26 and N=30. Another peak is seen at N=32 up to 4 MeV. Closed shell behaviour is clearly seen at N=28 and N=32 in Ca isotopes.

Closed shell effects in Sc are seen as peaks at N=28 and N=32 but they are slightly smaller (and therefore indicate slightly weaker shell effects) than in Ca. Δ_{2N} at N=28 in Sc is approximately 5.5 MeV. The Δ_{2N} graph of AME2016 data around N=32 maps a sharp peak of approximately 4.4 MeV. The data of this work shows a smoother curve with a flattened top from N=32 to N=33 around 3.5 MeV, much smaller than at N=28. Figure 5.24 shows the difference between the Δ_{2N} values from the AME2016 and this work (combining TITAN and LEBIT data) for Sc isotopes, the dark blue line is the difference and the wider band is the uncertainties. From the data in this study, Δ_{2N} around N=32 increases monotonically through ^{53}Sc and peaks at ^{52}Ca, consistent with the latter being a doubly-magic nucleus.

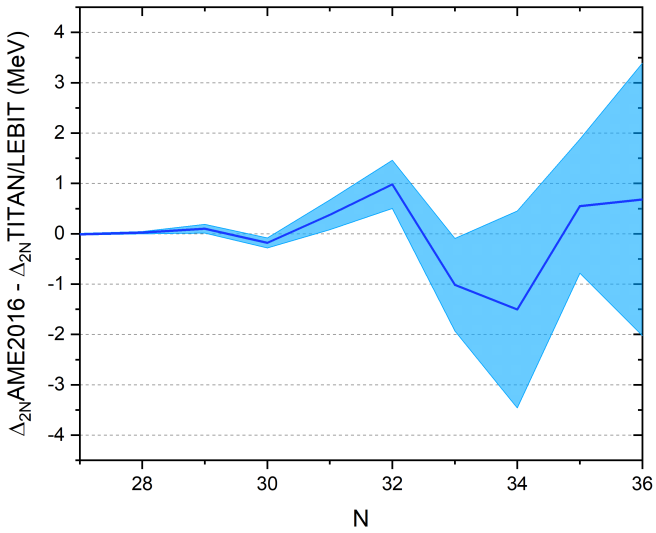

Figure 5.24: Difference between the empirical neutron-shell gap (Δ_{2N}) data of Sc isotopes from the AME2016 and a combination of this study and LEBIT [139] data, plotted against neutron number (N). The dark blue line is the difference between the two values, and the band is the uncertainties.

The Δ_{2N} at N=28 is approximately 5 MeV in both Ti and V. The Δ_{2N} around N=32 in Ti forms a curve similar to Sc isotopes, though the maximum is around 2.7 MeV. In V the curve around N=32 is even more shallow, about 2 MeV. The graphs of Δ_{2N} show the N=28 shell closure clearly in all elements, and the N=32 subshell disappear with increasing protons. The difference in behaviour of V isotopes after N=35 is again shown in figure 5.23 where, unlike the other elements, Δ_{2N} decreases rather than increases. This observation, as a result of the measurement of ^{58}V, suggests that shell effects have disappeared at N=32 in V isotopes or possible weak shell effects at N=34.

These mass measurement results provide a valuable test for theoretical models. Figure 5.25 shows the Δ_{2N} data compared to various ab initio (VS-IMSRG with 1.8/2.0(EM) [140]

and NN+3N(lnl) [141]) and phenomenological (KB3G [142] and the GX1A [17]) models [139]. The VS-IMSRG 1.8/2.0(EM) calculations correctly predict the trends of the data, but over-predicts the strength of effects at N=32 and N=34. The results from VS-IMSRG NN+3N(lnl) calculations are similar to VS-IMSRG 1.8/2.0(EM) but, in general, do not perform as well. The phenomenological models map the data well at N=28 and N=30, but after that point GX1A diverges. KB3G is reproduces the data the best of all models at N=32. The results of these calculations support the N=32 shell closure data, but do not form unanimous agreement in the N=34 region. Ab initio models have been applied to TITAN data in this region previously [30]. In this work the mass measurement results cover the N=32 and N=34 region, providing data for comparison of these models. The results indicate the models successfully map the trends at N=32, but need additional development at N=34. In the future, ab initio calculations will also be applied to V isotopes from this work.

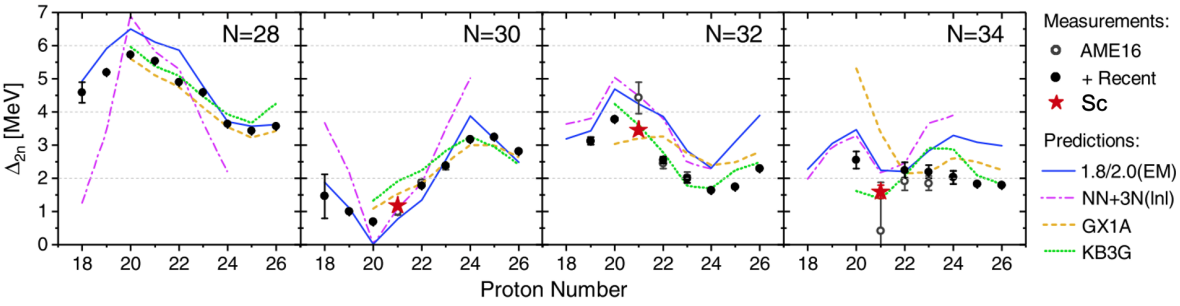

Figure 5.25: Measurements (points) and predictions (lines) of the empirical neutron-shell gap (Δ_{2N}) data for isotones with N=28,30,32,34. For more details see text. Figure from [139].

Investigations presented in this work in the Z≥20 region dramatically alter the role of Sc in the N=32 shell closure. The N=32 shell displays a smooth evolution above Z=20; it develops between ^{55}V and ^{54}Ti, increasing in strength through ^{53}Sc, and peaks in Ca, supporting ^{52}Ca as a doubly-magic nucleus. The new V measurements extend beyond N=34 and question the existence of a N=34 subshell closure. High-resolution mass measurements beyond N=34 in Sc isotopes are required to form a complete conclusion. Decay spectroscopy data in this region would provide valuable insight. High-resolution mass measurements of isotopes in the Z≤20 would be of great value to investigate the evolution of N=32,34 shells in isotopes 'south' of Ca.

Chapter 6

Conclusions & Outlook

Nuclear magic numbers are an anchor of nuclear physics. Since their discovery in stable nuclei they have been confirmed and are considered to be robust indicators for the underlying nuclear structure. However, in nuclei far from the valley of stability, with a great imbalance of protons to neutrons, 'new' magic numbers appear, which has been a rife area of research in recent years. There seems to be a strong indicator that some of the theoretical assumptions made for the stable nuclei do not hold for those further from stability. These most exotic nuclei have the shortest half-lives which makes studying them a technical challenge, due to the limited observation time available to deliver the ions from production to experimental facility before their decay. In addition, they are produced with low rates and a high level of contamination. With the advancement of RIB facilities and high-sensitivity mass spectrometry, the study of these nuclides to a high-precision has been unlocked, and with it the ability to explore the evolution of shell behaviour. Thus, providing ideal conditions to test and possibly improve model assumptions, and ultimately 'stress test' the applied theoretical framework.

The TITAN facility, coupled to the TRIUMF-ISAC RIB facility, has a world-wide unique combination of ion traps including an EBIT for charge breeding, a high-precision measurement Penning trap, and a recently installed MR-TOF-MS. This high-sensitivity device, capable of precisions comparable to Penning trap measurement methods, can be used to investigate short-lived radionuclides in regions of interest. The novel design of the TITAN MR-TOF-MS provides unique features, such as mass-selective retrapping, and it has successfully operated in many experiments at TRIUMF since its commissioning in 2017, establishing it as a trusted mass measurement device. The TITAN MR-TOF-MS can detect ions with production rates under 1 pps, measure species with lifetimes as short as 5 ms, and achieve precisions of $\delta m/m = 1 \times 10^{-7}$.

The TITAN MR-TOF-MS was employed in this thesis to perform high-precision mass measurements of ^{54}Ca, ^{54,55}Sc, $^{54-56}$Ti, and $^{54-58}$V around the N=32,34 region. Neutron-rich calcium, scandium, titanium and vanadium isotopes were produced by the ISOL method at the TRIUMF-ISAC facility. The ions were mass separated and transported to the TITAN MR-TOF-MS, where the atomic masses of ^{54}Ca, ^{54,55}Sc, $^{54-56}$Ti, and $^{54-58}$V were measured to precisions of 66 keV and under. The uncertainty of all masses measured is reduced compared with the AME2016, and the first ever direct mass measurement of ^{58}V is recorded. The uncertainties of ^{54}Ca, ^{54}Sc, ^{55}Ti and $^{54-57}$V are all equal to or below 20 keV. Of note is ^{55}V with an uncertainty of 10 keV, and the uncertainty of ^{55}Sc which is reduced by greater than a

factor of seven. Mass measurements of ^{54,55}Sc were on the order of 500-700 keV different than previous measurements, which dramatically alters the S_{2N} surface of the N=32 shell closure in this region.

The results presented in this thesis show a gradual decrease in strength of the N=32 shell closure across isotones with Z≥20, revealing a dramatic change in the role of Sc isotopes in this evolution compared to previous literature values. The measurements confirm the double-magicity of ^{54}Ca, as reported by [4], with increased precision and confirms that the effects are at their maximum in Ca amongst local isotope chains, and not in Sc, as previously documented. The N=32 shell closure is at its maximum in ^{52}Ca, is slightly weaker in ^{53}Sc, and the effects vanish somewhere between ^{55}V and ^{54}Ti, as established in the previous TITAN campaign [30, 31]. These new precise measurements of V isotopes reach beyond N=34 and aberrations are seen in the S_{2N} and Δ_{2N} plots in this region. The effects are smaller than those seen at N=32 in other isotope chains, but may be caused by shell effects at N=34. High-resolution mass measurements beyond N=34 in other isotope chains, as well as developments in theory calculations and decay-spectroscopy studies, is required to further understand this phenomena. These mass measurement results can be used to improve theoretical studies of nuclear structure and the observations around N=34 in V isotopes could inspire decay spectroscopy studies in the region.

There may be more 'new' nuclear magic numbers to discover in nuclei with an extreme Z=N imbalance. The combination of the novel technologies of MR-TOF mass spectrometers and world-class RIB development enables the study of these exotic species with low production rates and short half-lives. The TITAN MR-TOF-MS is only recently installed, but it is established as a trusted mass measurement device from comparisons with the TITAN measurement Penning trap, and now with another MR-TOF mass spectrometry facility. The measurement of ^{54}Ca, for which the uncertainty is more than halved, serves as a direct critical cross-check between MR-TOF mass spectrometry at different facilities around the globe. The agreement between this study and the prior ISOLTRAP result [4] confirms the robustness and reliability of this measurement technique, even in very exotic species. In the initial years of Penning trap mass spectrometry, general scepticism persisted, but today it is considered the gold standard of high-precision mass measurement. The future of the TITAN MR-TOF-MS is to utilise the device as an isobar separator to feed pure beams to the measurement Penning trap, and eventually include the EBIT for charge breeding too, while also providing complimentary access to direct mass measurements. These scientific and technical advances will enable higher sensitivity, precision, and resolution studies to elucidate more remote areas of the nuclear chart and further our understanding of the more complex nuclear structure that exists there.

Appendix

A Mass Results

Mass 54

The dominant species at mass 54 were $^{54}Cr^{+}$, $^{54}Fe^{+}$ and $^{54}Mn^{+}$. The chosen calibrant ion was $^{54}Cr^{+}$. In post-analysis of the data, a total of 97 counts of $^{54}Ca^{+}$, 344 counts of ^{54}Sc, 39 counts of $^{54}Ti^{+}$, and 132 counts of $^{54}V^{+}$ were observed. An example spectrum for mass 54 is shown in figure A.1.

Table A.1: Mass excess (ME) of the species of interest at 54u as measured by the TITAN MR-TOF-MS. The half-life ($t_{1/2}$) of ^{54}Ti is the value measured in this work.

Species	$t_{1/2}$ (ms)	Calibrant	ME (keV)
^{54}Ca	90(6)	^{54}Cr	-25130(20)
^{54}Sc	526(15)	^{54}Cr	-34438(14)
^{54}Ti	9000(1000)	^{54}Cr	-45735(37)
^{54}V	49800(500)	^{54}Cr	-49896(18)

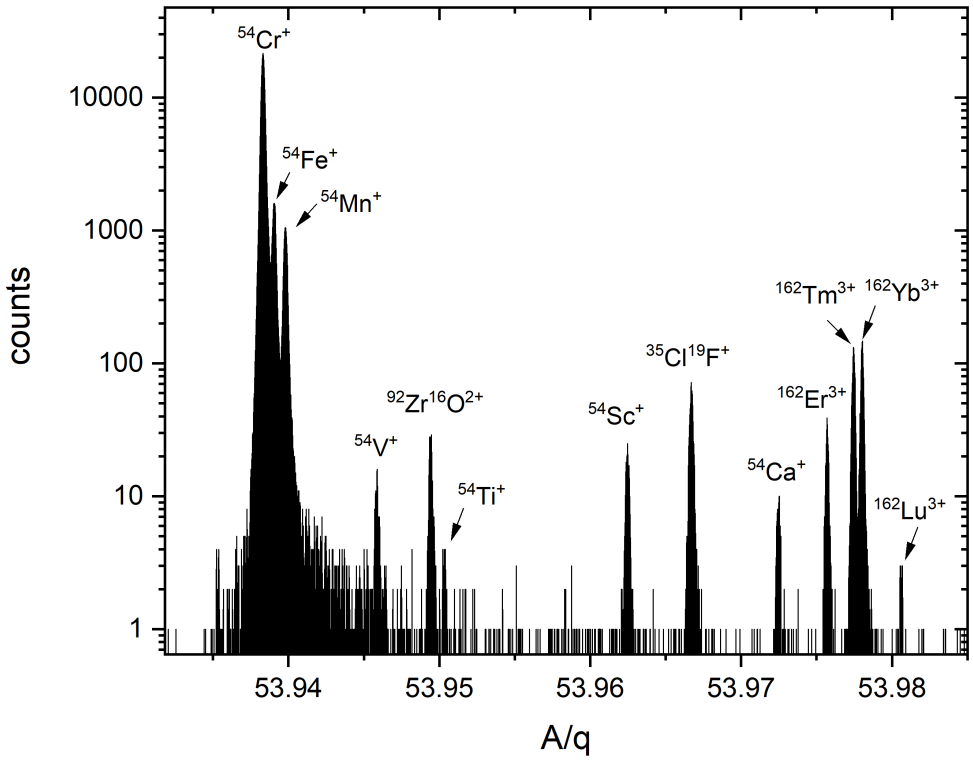

Figure A.1: TITAN MR-TOF-MS spectrum at A/q = 54 taken with 520 isochronous turns (IT). The achieved resolving power was over 200,000.

Mass 55

At 55u, $^{55}Cr^{+}$ is the most abundant species, as seen in figures A.2 and A.3, and is employed as the calibrant ion. Species of interest are $^{55}Sc^{+}$ (13 counts), $^{55}Ti^{+}$ (37 counts) and $^{55}V^{+}$ (21489 counts).

Table A.2: Mass excess (ME) of the species of interest at 55u as measured by the TITAN MR-TOF-MS.

Species	$t_{1/2}$ (ms)	Calibrant	ME (keV)
^{55}Sc	105(6)	^{55}Cr	-30842(62)
^{55}Ti	1300(100)	^{55}Cr	-41820(25)
^{55}V	6540(150)	^{55}Cr	-49130(10)

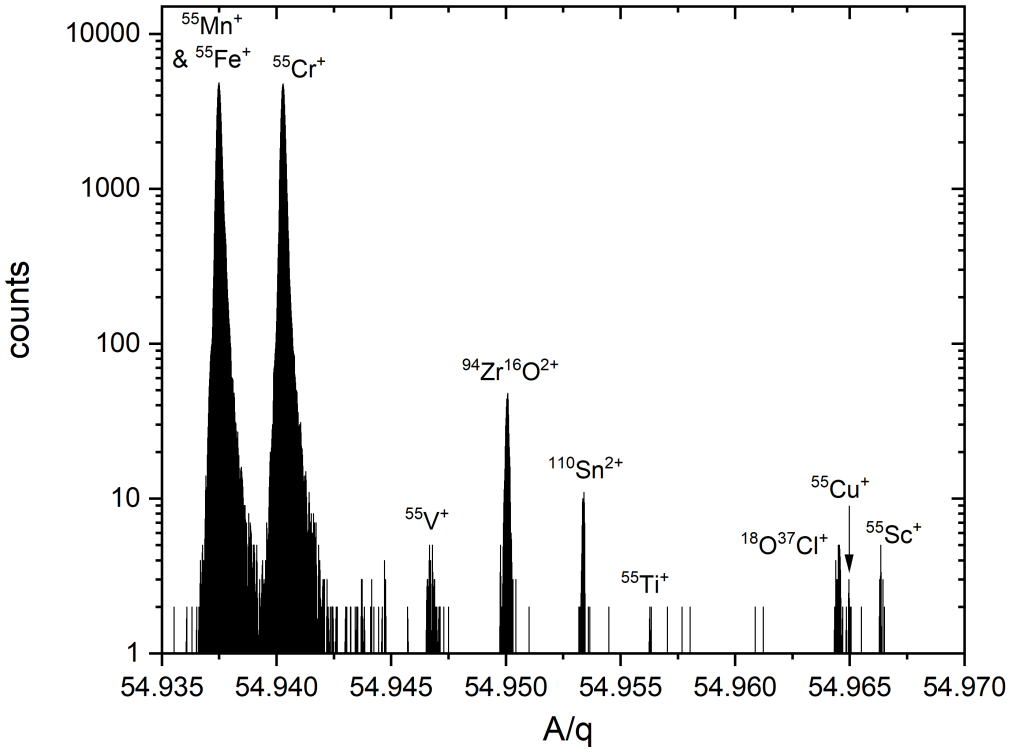

Figure A.2: TITAN MR-TOF-MS spectrum at A/q = 55 taken with 350 IT. The achieved resolving power was over 200,000.

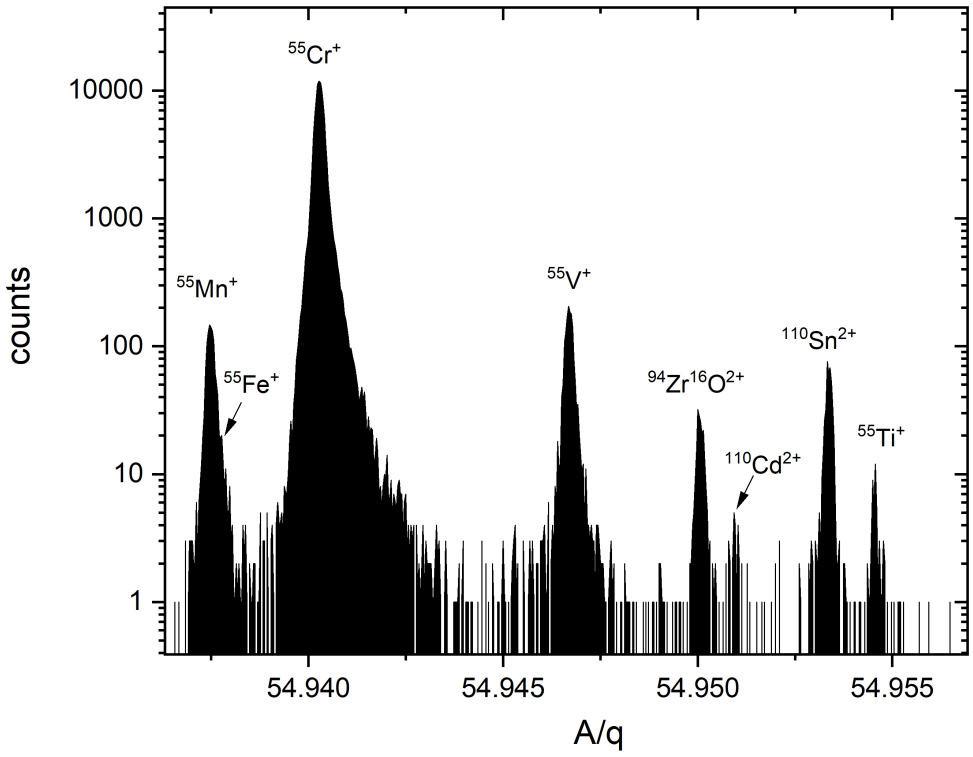

Figure A.3: TITAN MR-TOF-MS spectrum at A/q = 55 taken with 350 IT. The achieved resolving power was over 200,000.

Mass 56

$^{112}Sn^{2+}$ is the most abundant species at 56u, with other well identified peaks of $^{56}Cr^{+}$, $^{56}Fe^{+}$ and $^{56}Mn^{+}$ visible in the spectrum. $^{56}Cr^{+}$ was used for calibration. A spectrum of mass 56 is shown in figure A.4. The $^{56}V^{+}$ is isolated in the spectrum, and 152 counts were obtained. $^{56}Ti^{+}$ is to the right of the indicated CaO peak. A spectrum was obtained where the ^{56}Ti peak is separate, containing 22 counts, which enabled a mass measurement to be made.

Table A.3: Mass excess (ME) of the species of interest at 56u as measured by the TITAN MR-TOF-MS.

Species	$t_{1/2}$ (ms)	Calibrant	ME (keV)
^{56}Ti	200(5)	^{56}Cr	-39348(28)
^{56}V	216(4)	^{56}Cr	-46266(14)

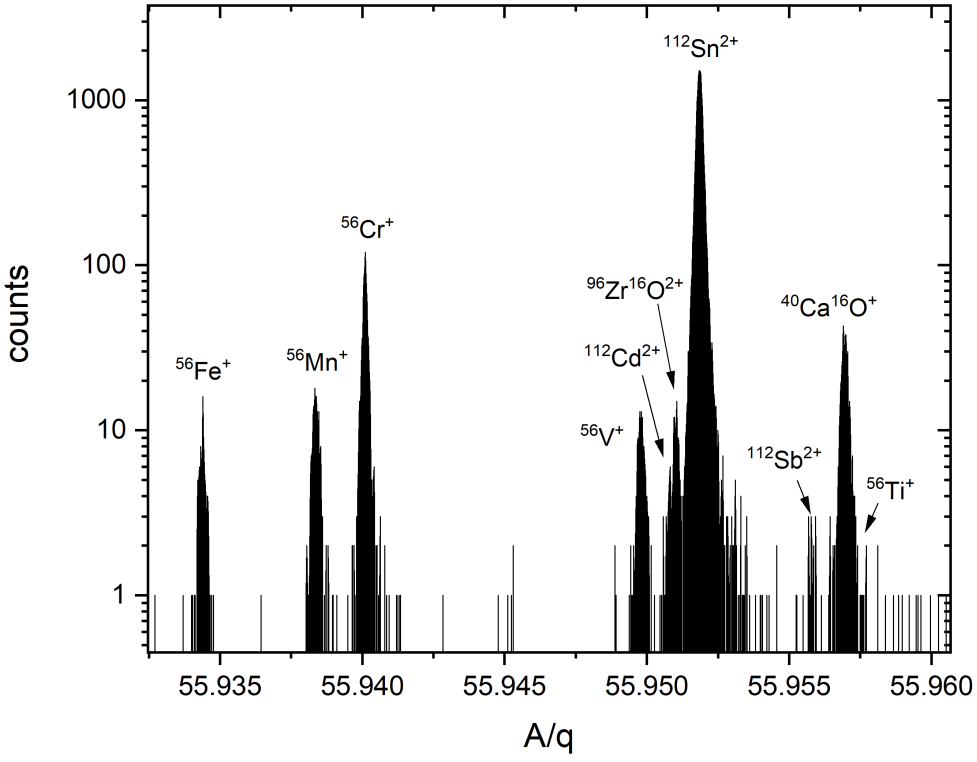

Figure A.4: TITAN MR-TOF-MS spectrum at A/q = 56 taken with 550 IT. The achieved resolving power was over 180,000.

Mass 57

At 57u $^{114}Sn^{2+}$ is the dominant species. A significant peak of $^{57}Cr^{+}$ is used as the calibrant. The mass excess of ^{57}V ($t_{1/2} = 350(10)$ ms) measured by the TITAN MR-TOF-MS is -44381(12) keV. There are 174 counts of $^{57}V^{+}$, which is to the right of the $^{114}Sn^{2+}$ peak. A spectrum of mass 57 can be seen in figure A.5.

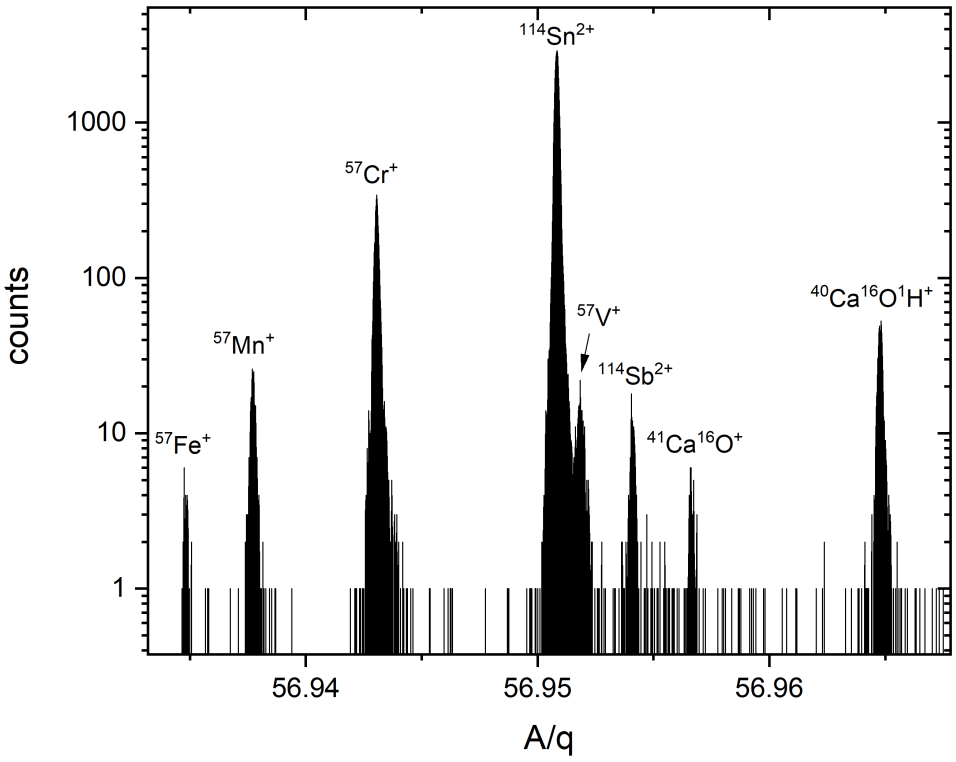

Figure A.5: TITAN MR-TOF-MS spectrum at A/q = 57 taken with 528 IT. The achieved resolving power was over 200,000.

Mass 58

At 58u the dominant species are $^{58}Fe^{+}$, $^{58}Ni^{+}$, $^{58}Co^{+}$, $^{58}Mn^{+}$, $^{58}Cr^{+}$ as well as $^{116}Sn^{2+}$, see figure A.6. 9 counts of $^{58}V^{+}$ were detected. From this data, using $^{58}Fe^{+}$ as the calibrant, the mass excess of ^{58}V ($t_{1/2}$ = 191(10) ms) is measured by the TITAN MR-TOF-MS to be -40372(66) keV.

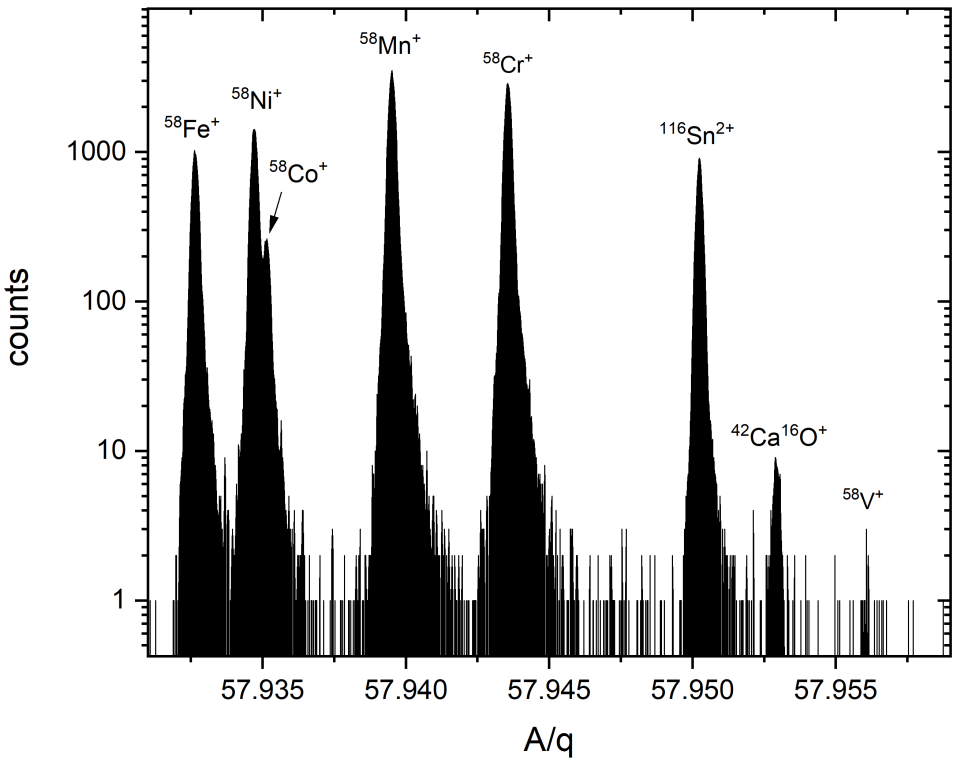

Figure A.6: TITAN MR-TOF-MS spectrum at A/q = 58 taken with 520 IT. There are six detected counts in the $^{58}V^{+}$ peak. The achieved resolving power was over 200,000.

B Comparison with literature values

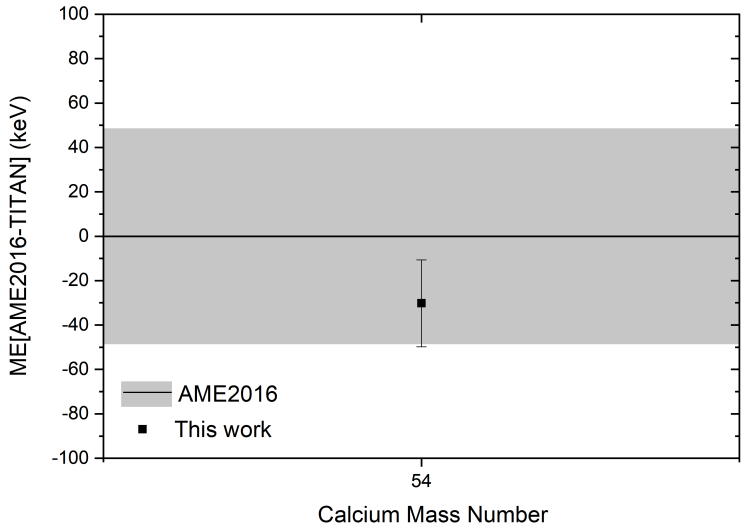

Figure B.1: Comparison of mass excess (ME) measurements of calcium isotopes between the AME2016 and this work (TITAN). AME2016 uncertainty is shown as the grey bands.

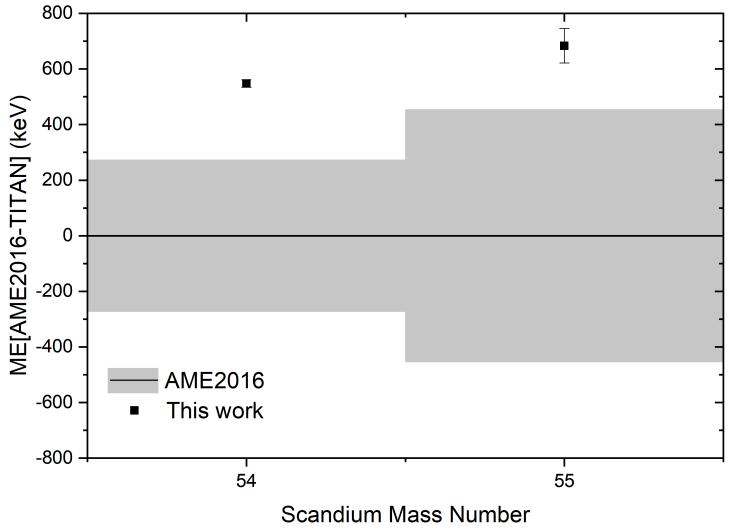

Figure B.2: Comparison of mass excess (ME) measurements of scandium isotopes between the AME2016 and this work (TITAN). AME2016 uncertainty is shown as the grey bands.

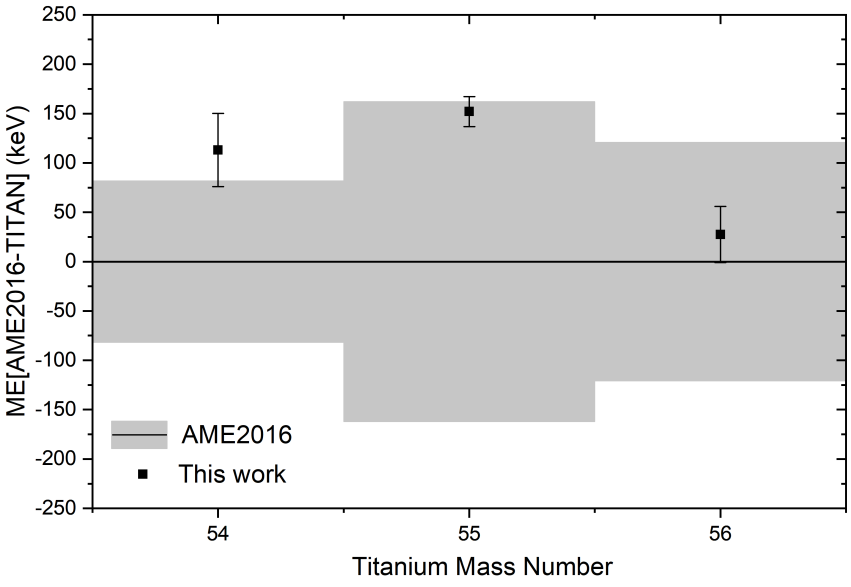

Figure B.3: Comparison of mass excess (ME) measurements of titanium isotopes between the AME2016 and this work (TITAN). AME2016 uncertainty is shown as the grey bands.

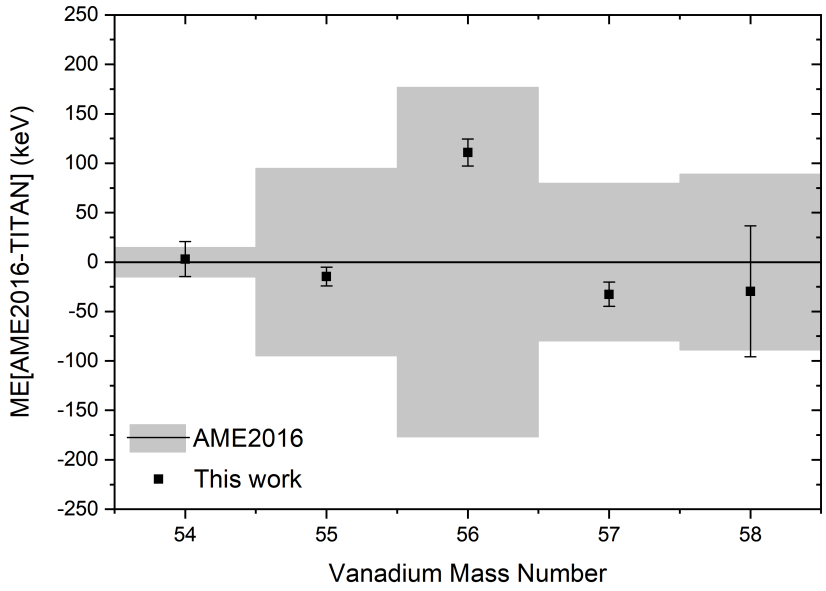

Figure B.4: Comparison of mass excess (ME) measurements of vanadium isotopes between the AME2016 and this work (TITAN). AME2016 uncertainty is shown as the grey bands.

Bibliography

[1] I. Bentley et al. "Shell structure from nuclear observables". In: *Physical Review C* 93.4 (2016). ISSN: 24699993. DOI: 10.1103/PhysRevC.93.044337. arXiv: 1604.08143.

[2] M. Goeppert Mayer. "On Closed Shells in Nuclei. II". In: *Phys. Rev.* 75 (12 June 1949), pp. 1969–1970. DOI: 10.1103/PhysRev.75.1969. URL: https://link.aps.org/doi/10.1103/PhysRev.75.1969.

[3] A. T. Gallant et al. "New Precision Mass Measurements of Neutron-Rich Calcium and Potassium Isotopes and Three-Nucleon Forces". In: *Phys. Rev. Lett.* 109 (3 July 2012), p. 032506. DOI: 10.1103/PhysRevLett.109.032506. URL: https://link.aps.org/doi/10.1103/PhysRevLett.109.032506.

[4] F. Wienholtz et al. "Masses of exotic calcium isotopes pin down nuclear forces". In: *Nature* 498 (June 2013), 346 EP -. URL: http://dx.doi.org/10.1038/nature12226.

[5] T. Otsuka et al. "Evolution of shell structure in exotic nuclei". In: *Reviews of Modern Physics* 92.1 (2020), p. 15002. ISSN: 15390756. DOI: 10.1103/RevModPhys.92.015002. arXiv: 1805.06501. URL: https://doi.org/10.1103/RevModPhys.92.015002.

[6] P. Campbell, I. D. Moore, and M. R. Pearson. "Laser spectroscopy for nuclear structure physics". In: *Progress in Particle and Nuclear Physics* 86 (Jan. 2016), pp. 127–180. DOI: 10.1016/j.ppnp.2015.09.003.

[7] K. Blaum, J. Dilling, and W. Nörtershäuser. "Precision atomic physics techniques for nuclear physics with radioactive beams". In: *Physica Scripta* T152 (2013). ISSN: 00318949. DOI: 10.1088/0031-8949/2013/T152/014017. arXiv: 1210.4045.

[8] M. Wang et al. "The AME2016 atomic mass evaluation (II). Tables, graphs and references". In: *Chinese Physics C* 41.3 (Mar. 2017), p. 030003. DOI: 10.1088/1674-1137/41/3/030003.

[9] A. Huck et al. "Beta decay of the new isotopes ^{52}K, ^{52}Ca, and ^{52}Sc; a test of the shell model far from stability". In: *Phys. Rev. C* 31 (6 June 1985), pp. 2226–2237. DOI: 10.1103/PhysRevC.31.2226. URL: https://link.aps.org/doi/10.1103/PhysRevC.31.2226.

[10] X. L. Tu et al. "Direct mass measurements of the neutron-rich isotopes of chlorine through iron". In: *Zeitschrift für Physik A Atomic Nuclei* 337.4 (1990), pp. 361–366. ISSN: 09301151. DOI: 10.1007/BF01294971.

[11] H. L. Seifert et al. "Mass measurement of neutron-rich isotopes from ^{51}Ca to ^{72}Ni". In: *Zeitschrift für Physik A Atomic Nuclei* (), pp. 25–32.

[12] Y. Bai et al. "Mass measurement in the fp-shell using the TOFI spectrometer". In: 90 (1998), pp. 90–93. DOI: 10.1063/1.57312.

[13] J. I. Prisciandaro et al. "New evidence for a subshell gap at N=32". In: *Physics Letters B* 510.1 (2001), pp. 17–23. ISSN: 0370-2693. DOI: https://doi.org/10.1016/S0370-2693(01)00565-2. URL: http://www.sciencedirect.com/science/article/pii/S0370269301005652.

[14] P. F. Mantica et al. "β decay studies of the neutron-rich $^{56--58}$V isotopes". In: *Phys. Rev. C* 67 (1 Jan. 2003), p. 014311. DOI: 10.1103/PhysRevC.67.014311. URL: https://link.aps.org/doi/10.1103/PhysRevC.67.014311.

[15] P. F. Mantica et al. "β-decay properties of ^{55,56}Ti". In: *Phys. Rev. C* 68 (4 Oct. 2003), p. 044311. DOI: 10.1103/PhysRevC.68.044311. URL: https://link.aps.org/doi/10.1103/PhysRevC.68.044311.

[16] S. N. Liddick et al. "Development of shell closures at N= 32, 34. I. decay of neutron-rich Sc isotopes". In: *Phys. Rev. C* 70 (Dec. 2004). DOI: 10.1103/PhysRevC.70.064303.

[17] M. Honma et al. "New effective interaction for pf-shell nuclei and its implications for the stability of the $N = Z = 28$ closed core". In: *Phys. Rev. C* 69 (3 Mar. 2004), p. 034335. DOI: 10.1103/PhysRevC.69.034335. URL: https://link.aps.org/doi/10.1103/PhysRevC.69.034335.

[18] C. Guenaut et al. "Mass measurements of 56-57 Cr and the question of shell reincarnation at N = 32". In: *Journal of Physics G: Nuclear and Particle Physics* 31.10 (2005), S1765. URL: http://stacks.iop.org/0954-3899/31/i=10/a=069.

[19] P. F. Mantica et al. "β decay of neutron-rich $^{53-56}$Ca". In: *Phys. Rev. C* 77 (1 Jan. 2008), p. 014313. DOI: 10.1103/PhysRevC.77.014313. URL: https://link.aps.org/doi/10.1103/PhysRevC.77.014313.

[20] H. L. Crawford et al. "β decay and isomeric properties of neutron-rich Ca and Sc isotopes". In: *Phys. Rev. C* 82 (1 July 2010), p. 014311. DOI: 10.1103/PhysRevC.82.014311. URL: https://link.aps.org/doi/10.1103/PhysRevC.82.014311.

[21] M. Rejmund et al. "Shell evolution and the $N = 34$ "magic number"". In: *Phys. Rev. C* 76 (2 Aug. 2007), p. 021304. DOI: 10.1103/PhysRevC.76.021304. URL: https://link.aps.org/doi/10.1103/PhysRevC.76.021304.

[22] S. Zhu et al. "High-lying, non-yrast shell structure in Ti 52". In: *Physical Review C - Nuclear Physics* 80.2 (2009). ISSN: 1089490X. DOI: 10.1103/PhysRevC.80.024318.

[23] D. Steppenbeck et al. "Evidence for a new nuclear 'magic number' from the level structure of 54Ca". In: *Nature* 502 (Oct. 2013), 207 EP -. URL: http://dx.doi.org/10.1038/nature12522.

[24] S. Michimasa et al. "Magic Nature of Neutrons in Ca 54: First Mass Measurements of Ca 55-57". In: *Physical Review Letters* 121.2 (2018), p. 22506. ISSN: 10797114. DOI: 10.1103/PhysRevLett.121.022506. URL: https://doi.org/10.1103/PhysRevLett.121.022506.

[25] M. Rosenbusch et al. "Probing the $N = 32$ Shell Closure below the Magic Proton Number $Z = 20$: Mass Measurements of the Exotic Isotopes ^{52,53}K". In: *Phys. Rev. Lett.* 114 (20 May 2015), p. 202501. DOI: 10.1103/PhysRevLett.114.202501. URL: https://link.aps.org/doi/10.1103/PhysRevLett.114.202501.

[26] Xu Xing et al. "Direct mass measurements of neutron-rich 86 Kr projectile fragments and the persistence of neutron magic number N =32 in Sc isotopes". In: *Chinese Physics C* 39.10 (2015), p. 104001. URL: http://stacks.iop.org/1674-1137/39/i=10/a=104001.

[27] D. Steppenbeck et al. "Low-Lying Structure of ^{50}Ar and the $N = 32$ Subshell Closure". In: *Phys. Rev. Lett.* 114 (25 June 2015), p. 252501. DOI: 10.1103/PhysRevLett.114.252501. URL: https://link.aps.org/doi/10.1103/PhysRevLett.114.252501.

[28] D. Steppenbeck et al. "Structure of 55Sc and development of the N=34 subshell closure". In: *Physical Review C* 96 (Oct. 2017). DOI: 10.1103/PhysRevC.96.064310.

[29] R. F. Garcia Ruiz et al. "Unexpectedly large charge radii of neutron-rich calcium isotopes". In: *Nature Physics* 12.6 (2016), pp. 594–598. ISSN: 17452481. DOI: 10.1038/nphys3645. arXiv: 1602.07906.

[30] E. Leistenschneider et al. "Dawning of the $N = 32$ Shell Closure Seen through Precision Mass Measurements of Neutron-Rich Titanium Isotopes". In: *Phys. Rev. Lett.* 120 (6 Feb. 2018), p. 062503. DOI: 10.1103/PhysRevLett.120.062503. URL: https://link.aps.org/doi/10.1103/PhysRevLett.120.062503.

[31] M. P. Reiter et al. "Quenching of the $N = 32$ neutron shell closure studied via precision mass measurements of neutron-rich vanadium isotopes". In: *Phys. Rev. C* 98 (2 Aug. 2018), p. 024310. DOI: 10.1103/PhysRevC.98.024310. URL: https://link.aps.org/doi/10.1103/PhysRevC.98.024310.

[32] Y. Blumenfeld, T. Nilsson, and P. Van Duppen. "Facilities and methods for radioactive ion beam production". In: *Physica Scripta* T152 (Jan. 2013), p. 014023. DOI: 10.1088/0031-8949/2013/t152/014023. URL: https://doi.org/10.1088/0031-8949/2013/t152/014023.

[33] C. Jesch. "The multiple-reflection time-of-flight isobar separator for TITAN and direct mass measurements at the FRS Ion Catcher". eng. PhD Thesis. Otto-Behaghel-Str. 8, 35394 Gießen: Justus-Liebig-Universität, 2016. URL: http://geb.uni-giessen.de/geb/volltexte/2016/12096.

[34] B. Jacquot et al. "GANIL Status report". In: (Mar. 2005).

[35] H. Geissel et al. "The GSI projectile fragment separator (FRS): a versatile magnetic system for relativistic heavy ions". In: *Nuclear Instruments and Methods in Physics Research Section B: Beam Interactions with Materials and Atoms* 70.1 (1992), pp. 286–297. ISSN: 0168-583X. DOI: https://doi.org/10.1016/0168-583X(92)95944-M. URL: https://www.sciencedirect.com/science/article/pii/0168583X9295944M.

[36] A. Gade and B. M. Sherrill. "NSCL and FRIB at Michigan State University: Nuclear science at the limits of stability". In: *Physica Scripta* 91.5 (2016). ISSN: 14024896. DOI: 10.1088/0031-8949/91/5/053003.

[37] T. Kubo. "In-flight RI beam separator BigRIPS at RIKEN and elsewhere in Japan". In: *Nuclear Instruments and Methods in Physics Research Section B: Beam Interactions with Materials and Atoms* 204 (2003). 14th International Conference on Electromagnetic Isotope Separators and Techniques Related to their Applications, pp. 97–113. ISSN: 0168-583X. DOI: https://doi.org/10.1016/S0168-583X(02)01896-7. URL: https://www.sciencedirect.com/science/article/pii/S0168583X02018967.

[38] X. Zhou. "The Heavy Ion Research Facility in Lanzhou". In: *Nuclear Physics News* 26.2 (2016), pp. 4–9. DOI: 10.1080/10619127.2016.1177330. eprint: https://doi.org/10.1080/10619127.2016.1177330. URL: https://doi.org/10.1080/10619127.2016.1177330.

[39] G. Rosner. "Future Facility: FAIR at GSI". In: *Nuclear Physics B - Proceedings Supplements* 167 (2007). Proceedings of the 7th International Conference on Hyperons, Charm and Beauty Hadrons, pp. 77–81. ISSN: 0920-5632. DOI: https://doi.org/10.1016/j.nuclphysbps.2006.12.089. URL: https://www.sciencedirect.com/science/article/pii/S0920563206010516.

[40] T. Nilsson. "The ISOLDE facility at CERN". In: *Exotic Nuclei and Atomic Masses*. Ed. by Juha Äystö et al. Berlin, Heidelberg: Springer Berlin Heidelberg, 2003, pp. 469–472. ISBN: 978-3-642-55560-2.

[41] M.J.G. Borge. "Highlights of the ISOLDE facility and the HIE-ISOLDE project". In: *Nuclear Instruments and Methods in Physics Research Section B: Beam Interactions with Materials and Atoms* 376 (2016). Proceedings of the XVIIth International Conference on Electromagnetic Isotope Separators and Related Topics (EMIS2015), Grand Rapids, MI, U.S.A., 11-15 May 2015, pp. 408–412. ISSN: 0168-583X. DOI: https://doi.org/10.1016/j.nimb.2015.12.048. URL: https://www.sciencedirect.com/science/article/pii/S0168583X16000057.

[42] A.C.C. Villari. "The accelerated ISOL technique and the SPIRAL project". In: *Nuclear Physics A* 693.1 (2001). Radioactive Nuclear Beams, pp. 465–476. ISSN: 0375-9474. DOI: https://doi.org/10.1016/S0375-9474(01)01107-1. URL: https://www.sciencedirect.com/science/article/pii/S0375947401011071.

[43] J. Dilling, R. Krücken, and L. Merminga. *ISAC and ARIEL: The TRIUMF radioactive beam facilities and the scientific program*. Jan. 2014, pp. 1–284. DOI: 10.1007/978-94-007-7963-1.

[44] J. Aysto et al. *Three decades of research using IGISOL technique at the University of Jyväskylä: A Portrait of the Ion Guide Isotope Separator On-Line Facility in Jyväskylä*. Jan. 2014. ISBN: 978-94-007-5554-3. DOI: 10.1007/978-94-007-5555-0.

[45] S. Essabaa et al. "The radioactive beam facility ALTO". In: *Nuclear Instruments and Methods in Physics Research Section B: Beam Interactions with Materials and Atoms* 317 (2013). XVIth International Conference on ElectroMagnetic Isotope Separators and Techniques Related to their Applications, December 2–7, 2012 at Matsue, Japan, pp. 218–222. ISSN: 0168-583X. DOI: https://doi.org/10.1016/j.nimb.2013.06.029. URL: https://www.sciencedirect.com/science/article/pii/S0168583X13007003.

[46] S. Gales. "GANIL-SPIRAL2: a new era". In: *Journal of Physics: Conference Series* 267 (Jan. 2011), p. 012009. DOI: 10.1088/1742-6596/267/1/012009. URL: https://doi.org/10.1088/1742-6596/267/1/012009.

[47] J. Bagger et al. "ARIEL at TRIUMF: Science and Technology". In: *9th International Particle Accelerator Conference*. 2018, MOXGB2. DOI: 10.18429/JACoW-IPAC2018-MOXGB2.

[48] J. Dilling et al. "Penning-Trap Mass Measurements in Atomic and Nuclear Physics". In: *Annual Review of Nuclear and Particle Science* 68.1 (2018), pp. 45–74. ISSN: 0163-8998. DOI: 10.1146/annurev-nucl-102711-094939.

[49] P. A. Butler et al. "TSR: A storage ring for HIE-ISOLDE". In: *Acta Physica Polonica B* 47.3 (2016), pp. 627–636. ISSN: 15095770. DOI: 10.5506/APhysPolB.47.627.

[50] F. Bosch. "Measurement of Mass and Beta-Lifetime of Stored Exotic Nuclei". In: vol. 651. Aug. 2004, pp. 137–168. ISBN: 978-3-540-22399-3. DOI: 10.1007/978-3-540-44490-9_5.

[51] B. Franzke. "The heavy ion storage and cooler ring project ESR at GSI". In: *Nuclear Instruments and Methods in Physics Research Section B: Beam Interactions with Materials and Atoms* 24-25 (1987), pp. 18–25. ISSN: 0168-583X. DOI: https://doi.org/10.1016/0168-583X(87)90583-0. URL: https://www.sciencedirect.com/science/article/pii/0168583X87905830.

[52] J.W. Xia et al. "The heavy ion cooler-storage-ring project (HIRFL-CSR) at Lanzhou". In: *Nuclear Instruments and Methods in Physics Research Section A: Accelerators, Spectrometers, Detectors and Associated Equipment* 488.1 (2002), pp. 11–25. ISSN: 0168-9002. DOI: https://doi.org/10.1016/S0168-9002(02)00475-8. URL: https://www.sciencedirect.com/science/article/pii/S0168900202004758.

[53] P. K. Ghosh. *Ion Traps*. Clarendon Press, 1995.

[54] M. König et al. "Quadrupole excitation of stored ion motion at the true cyclotron frequency". In: *International Journal of Mass Spectrometry and Ion Processes* 142.1 (1995), pp. 95–116. ISSN: 0168-1176. DOI: https://doi.org/10.1016/0168-1176(95)04146-C. URL: http://www.sciencedirect.com/science/article/pii/016811769504146C.

[55] A. G. Marshall and T. Chen. "40 years of Fourier transform ion cyclotron resonance mass spectrometry". In: *International Journal of Mass Spectrometry* 377 (2015). Special Issue: MS 1960 to Now, pp. 410–420. ISSN: 1387-3806. DOI: https://doi.org/10.1016/j.ijms.2014.06.034. URL: http://www.sciencedirect.com/science/article/pii/S1387380614002851.

[56] S. Eliseev et al. "Phase-Imaging Ion-Cyclotron-Resonance Measurements for Short-Lived Nuclides". In: *Phys. Rev. Lett.* 110 (8 Feb. 2013), p. 082501. DOI: 10.1103/PhysRevLett.110.082501. URL: https://link.aps.org/doi/10.1103/PhysRevLett.110.082501.

[57] H. Dehmelt. "Experiments with an isolated subatomic particle at rest". In: *Rev. Mod. Phys.* 62 (3 July 1990), pp. 525–530. DOI: 10.1103/RevModPhys.62.525. URL: https://link.aps.org/doi/10.1103/RevModPhys.62.525.

[58] G. Marx et al. "Status of the SHIPTRAP Project: A Capture and Storage Facility for Heavy Radionuclides from SHIP." In: *Atomic Physics at Accelerators: Mass Spectrometry.* (2001). URL: https://doi.org/10.1007/978-94-015-1270-1_50.

[59] J. Thompson, S. Rainville, and D. Pritchard. "Cyclotron frequency shifts arising from polarization forces." In: *Nature* 430 (2004), pp. 58–61. DOI: https://doi.org/10.1038/nature02682.

[60] E. G. Myers et al. "Atomic Masses of Tritium and Helium-3". In: *Phys. Rev. Lett.* 114 (1 Jan. 2015), p. 013003. DOI: 10.1103/PhysRevLett.114.013003. URL: https://link.aps.org/doi/10.1103/PhysRevLett.114.013003.

[61] S. Eliseev et al. "Direct Measurement of the Mass Difference of ^{163}Ho and ^{163}Dy Solves the Q-Value Puzzle for the Neutrino Mass Determination". In: *Phys. Rev. Lett.* 115 (6 Aug. 2015), p. 062501. DOI: 10.1103/PhysRevLett.115.062501. URL: https://link.aps.org/doi/10.1103/PhysRevLett.115.062501.

[62] M. Smith et al. "First penning-trap mass measurement of the exotic halo nucleus Li11". In: *Physical Review Letters* 101.20 (2008), pp. 1–4. ISSN: 00319007. DOI: 10.1103/PhysRevLett.101.202501.

[63] J. Dilling et al. "The proposed TITAN facility at ISAC for very precise mass measurements on highly charged short-lived isotopes". In: *Nuclear Instruments and Methods in Physics Research, Section B: Beam Interactions with Materials and Atoms*. 2003. DOI: 10.1016/S0168-583X(02)02118-3.

[64] M. Mukherjee et al. "ISOLTRAP: An on-line Penning trap for mass spectrometry on short-lived nuclides." In: *Eur. Phys. J. A* 35 (2008), pp. 1–29. URL: https://doi.org/10.1140/epja/i2007-10528-9.

[65] T. Eronen et al. "JYFLTRAP: a Penning trap for precision mass spectroscopy and isobaric purification". In: *The European Physical Journal A* 48.4 (2012), p. 46. DOI: 10.1140/epja/i2012-12046-1. URL: https://doi.org/10.1140/epja/i2012-12046-1.

[66] J. Ketelaer et al. "TRIGA-SPEC: A setup for mass spectrometry and laser spectroscopy at the research reactor TRIGA Mainz". In: *Nuclear Instruments and Methods in Physics Research Section A: Accelerators, Spectrometers, Detectors and Associated Equipment* 594.2 (2008), pp. 162–177. ISSN: 0168-9002. DOI: https://doi.org/10.1016/j.nima.2008.06.023. URL: https://www.sciencedirect.com/science/article/pii/S0168900208008693.

[67] S. Schwarz et al. "The LEBIT facility at MSU". In: *Hyperfine Interactions* 173.1 (2006), pp. 113–122. DOI: 10.1007/s10751-007-9549-9. URL: https://doi.org/10.1007/s10751-007-9549-9.

[68] G. Savard et al. "The Canadian Penning Trap Spectrometer at Argonne". In: *Atomic Physics at Accelerators: Mass Spectrometry.* (2001). URL: https://doi.org/10.1007/978-94-015-1270-1_18.

[69] W. R. Plaß, T. Dickel, and C. Scheidenberger. "Multiple-reflection time-of-flight mass spectrometry". In: *International Journal of Mass Spectrometry* 349-350.1 (2013), pp. 134–144. ISSN: 13873806. DOI: 10.1016/j.ijms.2013.06.005.

[70] H. Wollnik and M. Przewloka. "Time-of-flight mass spectrometers with multiply reflected ion trajectories". In: *International Journal of Mass Spectrometry and Ion Processes* (1990). ISSN: 01681176. DOI: 10.1016/0168-1176(90)85127-N.

[71] R. N. Wolf et al. "On-line separation of short-lived nuclei by a multi-reflection time-of-flight device". In: *Nuclear Instruments and Methods in Physics Research, Section A: Accelerators, Spectrometers, Detectors and Associated Equipment* 686 (2012), pp. 82–90. ISSN: 01689002. DOI: 10.1016/j.nima.2012.05.067.

[72] T. Dickel et al. "A high-performance multiple-reflection time-of-flight mass spectrometer and isobar separator for the research with exotic nuclei". In: *Nuclear Instruments and Methods in Physics Research, Section A: Accelerators, Spectrometers, Detectors and Associated Equipment* (2015). ISSN: 01689002. DOI: 10.1016/j.nima.2014.12.094.

[73] S. Ayet San Andrés et al. "High-resolution, accurate multiple-reflection time-of-flight mass spectrometry for short-lived, exotic nuclei of a few events in their ground and low-lying isomeric states". In: *Phys. Rev. C* 99 (6 June 2019), p. 064313. DOI: 10.1103/PhysRevC.99.064313.

[74] P. Schury et al. "A high-resolution multi-reflection time-of-flight mass spectrograph for precision mass measurements at RIKEN/SLOWRI". In: *Nuclear Instruments and Methods in Physics Research, Section B: Beam Interactions with Materials and Atoms* 335 (2014), pp. 39–53. ISSN: 0168583X. DOI: 10.1016/j.nimb.2014.05.016.

[75] T. Hirsh et al. "First operation and mass separation with the CARIBU MR-TOF". In: *Nuclear Instruments and Methods in Physics Research Section B: Beam Interactions with Materials and Atoms* 376 (Jan. 2015). DOI: 10.1016/j.nimb.2015.12.037.

[76] H. Penttilä et al. "Radioactive ion beam manipulation at the IGISOL-4 facility". In: *EPJ Web Conf.* 239 (2020), p. 17002. DOI: 10.1051/epjconf/202023917002. URL: https://doi.org/10.1051/epjconf/202023917002.

[77] P. Chauveau et al. "PILGRIM, a Multi-Reflection Time-of-Flight Mass Spectrometer for Spiral2-S^3 at GANIL". In: *Nucl. Instrum. Meth. B* 376 (2016). Ed. by G. Bollen et al., pp. 211–215. DOI: 10.1016/j.nimb.2016.01.025.

[78] C. Jesch et al. "The MR-TOF-MS isobar separator for the TITAN facility at TRIUMF". In: *Hyperfine Interactions* (May 2015). DOI: 10.1007/s10751-015-1184-2.

[79] G. C. Ball, G. Hackman, and R. Krücken. "The TRIUMF-ISAC facility: Two decades of discovery with rare isotope beams". In: *Physica Scripta* 91.9 (2016). ISSN: 14024896. DOI: 10.1088/0031-8949/91/9/093002.

[80] P. Bricault et al. "TRIUMF-ISAC target station and mass separator commissioning". In: *Nuclear Physics A* 701.1-4 (2002), pp. 49–53. ISSN: 03759474. DOI: 10.1016/S0375-9474(01)01546-9.

[81] J. Lassen et al. "Laser Ion Source Operation at the TRIUMF Radioactive Ion Beam Facility". In: *AIP Conference Proceedings*. AIP, 2009, pp. 9–15. DOI: 10.1063/1.3115616.

[82] R. Li et al. "Recent RILIS developments at the TRIUMF offline laser ion source test stand". In: *Hyperfine Interactions* 241.1 (2020), pp. 1–8. ISSN: 15729540. DOI: 10.1007/s10751-020-1694-4.

[83] S. Raeder et al. "An ion guide laser ion source for isobar-suppressed rare isotope beams". In: *Review of Scientific Instruments* 85.3 (2014). ISSN: 10897623. DOI: 10.1063/1.4868496.

[84] B. E. Schultz et al. "FEBIAD Ion Source Development At TRIUMF-ISAC". In: *9th International Particle Accelerator Conference (IPAC '18)* (2018), THPML041. DOI: 10.18429/JACoW-IPAC2018-THPML041.

[85] K. Jayamanna et al. "Off-line ion source terminal for ISAC at TRIUMF". In: *Review of Scientific Instruments* 79.2 (2008), pp. 2–6. ISSN: 00346748. DOI: 10.1063/1.2816928.

[86] K. Jayamanna et al. "Microwave-driven multipurpose ion source". In: *Review of Scientific Instruments* 67.3 (1996), pp. 1061–1063. ISSN: 10897623. DOI: 10.1063/1.1146758.

[87] K. Jayamanna et al. "A multicharge ion source (Supernanogan) for the OLIS facility at ISAC/TRIUMF". In: *Review of Scientific Instruments* 81.2 (2010). ISSN: 00346748. DOI: 10.1063/1.3303819.

[88] K. Jayamanna and C. Vockenhuber. "A hybrid surface arc discharge ion source to produce ultra pure Ca+2 beams for Ca40(,)Ti44 reaction studies at ISAC/TRIUMF". In: *Review of Scientific Instruments* 79.2 (2008), p. 02C712. DOI: 10.1063/1.2816939. eprint: https://aip.scitation.org/doi/pdf/10.1063/1.2816939. URL: https://aip.scitation.org/doi/abs/10.1063/1.2816939.

[89] P. Kunz et al. "Nuclear and in-source laser spectroscopy with the ISAC yield station". In: *Review of Scientific Instruments* 85.5 (2014). ISSN: 10897623. DOI: 10.1063/1.4878718. URL: http://dx.doi.org/10.1063/1.4878718.

[90] A. A. Kwiatkowski et al. "TITAN: An ion trap facility for on-line mass measurement experiments". In: *Hyperfine Interactions* 225.1-3 (2014), pp. 143–155. ISSN: 03043843. DOI: 10.1007/s10751-013-0892-8.

[91] M. Smith et al. "First tests of the TITAN digital RFQ beam cooler and buncher". In: *Hyperfine Interactions* 173 (Nov. 2006), pp. 171–180. DOI: 10.1007/s10751-007-9554-z.

[92] T. Brunner et al. "TITAN's digital RFQ ion beam cooler and buncher, operation and performance". In: *Nuclear Instruments and Methods in Physics Research Section A Accelerators Spectrometers Detectors and Associated Equipment* 676 (July 2011). DOI: 10.1016/j.nima.2012.02.004.

[93] A. Lapierre et al. "The TITAN EBIT charge breeder for mass measurements on highly charged short-lived isotopes—First online operation". In: *Nuclear Instruments and Methods in Physics Research Section A: Accelerators, Spectrometers, Detectors and Associated Equipment* 624 (Dec. 2010), pp. 54–64. DOI: 10.1016/j.nima.2010.09.030.

[94] K. G. Leach et al. "The TITAN in-trap decay spectroscopy facility at TRIUMF". In: *Nuclear Instruments and Methods in Physics Research, Section A: Accelerators, Spectrometers, Detectors and Associated Equipment* 780 (2015), pp. 91–99. ISSN: 01689002. DOI: 10.1016/j.nima.2014.12.118.

[95] M. Brodeur et al. "Verifying the accuracy of the TITAN Penning-trap mass spectrometer". In: *International Journal of Mass Spectrometry* 310 (Oct. 2011). DOI: 10.1016/j.ijms.2011.11.002.

[96] G. Bollen et al. "The accuracy of heavy-ion mass measurements using time of flight-ion cyclotron resonance in a Penning trap". In: *Journal of Applied Physics* 68.9 (1990), pp. 4355–4374. DOI: 10.1063/1.346185. eprint: https://doi.org/10.1063/1.346185. URL: https://doi.org/10.1063/1.346185.

[97] A. T. Gallant et al. "Highly charged ions in Penning traps: A new tool for resolving low-lying isomeric states". In: *Phys. Rev. C* 85 (4 Apr. 2012), p. 044311. DOI: 10.1103/PhysRevC.85.044311. URL: https://link.aps.org/doi/10.1103/PhysRevC.85.044311.

[98] A. A. Kwiatkowski et al. "Observation of a crossover of S2n in the island of inversion from precision mass spectrometry". In: *Physical Review C - Nuclear Physics* 92.6 (2015), pp. 1–5. ISSN: 1089490X. DOI: 10.1103/PhysRevC.92.061301.

[99] T. Dickel et al. "Isobar Separation in a Multiple-Reflection Time-of-Flight Mass Spectrometer by Mass-Selective Re-Trapping". In: *Journal of the American Society for Mass Spectrometry* 28.6 (2017). PMID: 28299713, pp. 1079–1090. DOI: 10.1021/jasms.8b05562.

[100] A. Jacobs. "Collision Induced Dissociation and Mass Spectrometry with the TITAN Multiple-Reflection Time-of-Flight Mass Spectrometer". MSc Thesis. 2019.

[101] et al. C. Izzo E. Dunling. "Mass measurements of neutron-rich indium isotopes for r-process studies". In: *Phys. Rev. C* 103 (2 Feb. 2021), p. 025811. DOI: 10.1103/PhysRevC.103.025811. URL: https://link.aps.org/doi/10.1103/PhysRevC.103.025811.

[102] W. R. Plaß et al. "Isobar separation by time-of-flight mass spectrometry for low-energy radioactive ion beam facilities". In: *Nuclear Instruments and Methods in Physics Research Section B: Beam Interactions with Materials and Atoms* 266.19 (2008). Proceedings of the XVth International Conference on Electromagnetic Isotope Separators and Techniques Related to their Applications, pp. 4560–4564. ISSN: 0168-583X. DOI: https://doi.org/10.1016/j.nimb.2008.05.079.

[103] W. R. Plaß et al. "High-performance multiple-reflection time-of-flight mass spectrometers for research with exotic nuclei and for analytical mass spectrometry". In: *Physica Scripta* 2015.T166 (2015). ISSN: 02811847. DOI: 10.1088/0031-8949/2015/T166/014069.

[104] M. Yavor et al. "Ion-optical design of a high-performance multiple-reflection time-of-flight mass spectrometer and isobar separator". In: *International Journal of Mass Spectrometry* 381-382 (Feb. 2015). DOI: 10.1016/j.ijms.2015.01.002.

[105] *ETP 500PS MAGNETOF -HV, RoHS MECHANICAL SPECIFICATION, 14DM572.* MSDM572. Rev. A. ETP electron multipliers. 21/10/2015. URL: http://a6e5e8fc1ad706fd1969-b6eded4adeadd283a6338023bbf1f6de.r62.cf4.rackcdn.com/eecf54836514652645e0c9909cd7324f18ee5597-14DM572MagneTOFPlusDatasheet.pdf.

[106] T. Dickel et al. "Dynamical time focus shift in multiple-reflection time-of-flight mass spectrometers". In: *International Journal of Mass Spectrometry* 412 (2017), pp. 1–7. ISSN: 1387-3806. DOI: https://doi.org/10.1016/j.ijms.2016.11.005.

[107] D. Short. "Nuclear Isobar Separation for Penning Trap Mass Measurements at TRIUMF". MSc Thesis. Simon Fraser University, 2018. URL: https://titan.triumf.ca/research/publications/Short_MSC_SFU_2017.pdf.

[108] P. Schury et al. "Beam purification techniques for low energy rare isotope beams from a gas cell". In: *TCP 2006 Conference paper, Springer, Berlin, Heidelberg* (2007), pp. 321–326. DOI: https://doi.org/10.1007/978-3-540-73466-6_39.

[109] J. Ebert. "Mass Measurements of U-Projectile Fragments for the First Time with a Multiple-Reflection Time-Of-Flight Mass Spectrometer". PhD Thesis. 2016.

[110] M. Rosenbusch et al. "Towards Systematic Investigations of Space-Charge Phenomena in Multi-Reflection Ion Traps". In: vol. 1521. Mar. 2013. DOI: 10.1063/1.4796061.

[111] D. Grinfeld et al. "Space-charge effects in an electrostatic multireflection ion trap". In: *European journal of mass spectrometry (Chichester, England)* 20 (June 2014), pp. 131–42. DOI: 10.1255/ejms.1265.

[112] C. Will. "TITAN's Multiple-Reflection Time-of-Flight Mass Spectrometer and Isobar Separator – Characterization and First Experiments". BSc Thesis. 2017.

[113] M. P. Reiter. *TITAN MR-TOF: alignment to TITAN Beam Line*. Tech. rep. Mar. 2017.

[114] T. Dickel et al. "Recent upgrades of the multiple-reflection time-of-flight mass spectrometer at TITAN, TRIUMF". In: *Hyperfine Interactions* 240.1 (2019), pp. 1–9. ISSN: 15729540. DOI: 10.1007/s10751-019-1610-y.

[115] M. Goeppert Mayer. "The Shell Model." In: *Science* 145 3636 (1964), pp. 999–1006.

[116] O. Sorlin and M.G. Porquet. "Nuclear magic numbers: New features far from stability". In: *Progress in Particle and Nuclear Physics* 61.2 (2008), pp. 602–673. ISSN: 0146-6410. DOI: https://doi.org/10.1016/j.ppnp.2008.05.001. URL: http://www.sciencedirect.com/science/article/pii/S0146641008000380.

[117] K. S. Krane. *Introductory nuclear physics*. New York, NY: Wiley, 1988.

[118] J. D. Holt et al. "Three-body forces and shell structure in calcium isotopes". In: *Journal of Physics G: Nuclear and Particle Physics* 39.8 (2012). ISSN: 09543899. DOI: 10.1088/0954-3899/39/8/085111. arXiv: 1009.5984.

[119] G. Hagen et al. "Evolution of shell structure in neutron-rich calcium isotopes". In: *Physical Review Letters* 109.3 (2012), pp. 1–5. ISSN: 00319007. DOI: 10.1103/PhysRevLett.109.032502. arXiv: 1204.3612.

[120] V. Somà et al. "Chiral two- and three-nucleon forces along medium-mass isotope chains". In: *Physical Review C - Nuclear Physics* 89.6 (2014), pp. 1–5. ISSN: 1089490X. DOI: 10.1103/PhysRevC.89.061301.

[121] A.H. Wapstra and K. Bos. "The 1977 atomic mass evaluation: in four parts part I. Atomic mass table". In: *Atomic Data and Nuclear Data Tables* 19.3 (1977), pp. 177–214. ISSN: 0092-640X. DOI: https://doi.org/10.1016/0092-640X(77)90020-1. URL: https://www.sciencedirect.com/science/article/pii/0092640X77900201.

[122] A.H. Wapstra and G. Audi. "The 1983 atomic mass evaluation: (I). Atomic mass table". In: *Nuclear Physics A* 432.1 (1985), pp. 1–54. ISSN: 0375-9474. DOI: https://doi.org/10.1016/0375-9474(85)90283-0. URL: https://www.sciencedirect.com/science/article/pii/0375947485902830.

[123] G. Audi and A.H. Wapstra. "The 1993 atomic mass evaluation: (I) Atomic mass table". In: *Nuclear Physics A* 565.1 (1993), pp. 1–65. ISSN: 0375-9474. DOI: https://doi.org/10.1016/0375-9474(93)90024-R. URL: https://www.sciencedirect.com/science/article/pii/037594749390024R.

[124] G. Audi, A.H. Wapstra, and C. Thibault. "The Ame2003 atomic mass evaluation: (II). Tables, graphs and references". In: *Nuclear Physics A* 729.1 (2003). The 2003 NUBASE and Atomic Mass Evaluations, pp. 337–676. ISSN: 0375-9474. DOI: https://doi.org/10.1016/j.nuclphysa.2003.11.003. URL: https://www.sciencedirect.com/science/article/pii/S0375947403018098.

[125] M. Wang et al. "The Ame2012 atomic mass evaluation". In: *Chinese Physics C* 36.12 (Dec. 2012), pp. 1603–2014. DOI: 10.1088/1674-1137/36/12/003. URL: https://doi.org/10.1088/1674-1137/36/12/003.

[126] M. Matoś. "Isochronous mass measurement of short-lived neutron rich nuclides at the FRS-ESR facilities". PhD thesis. Justus-Liebig-Universität Gießen, 2004.

[127] A. Estradé et al. "Time-of-flight mass measurements for nuclear processes in neutron star crusts". In: *Physical Review Letters* 107.17 (2011). ISSN: 00319007. DOI: 10.1103/PhysRevLett.107.172503. arXiv: 1109.5200.

[128] Z. Meisel et al. "Mass Measurement of Sc 56 Reveals a Small A=56 Odd-Even Mass Staggering, Implying a Cooler Accreted Neutron Star Crust". In: *Physical Review Letters* 115.16 (2015), pp. 1–6. ISSN: 10797114. DOI: 10.1103/PhysRevLett.115.162501.

[129] X. Xu et al. "Direct mass measurements of neutron-rich 86Kr projectile fragments and the persistence of neutron magic number N=32 in Sc isotopes". In: *Chinese Physics C* 39.10 (2015), pp. 0–5. ISSN: 16741137. DOI: 10.1088/1674-1137/39/10/104001.

[130] X. Xu et al. "Masses of neutron-rich Sc 52-54 and Ti 54,56 nuclides: The N=32 subshell closure in scandium". In: *Physical Review C* 99.6 (2019), pp. 1–6. ISSN: 24699993. DOI: 10.1103/PhysRevC.99.064303.

[131] Z. Meisel et al. "Nuclear mass measurements map the structure of atomic nuclei and accreting neutron stars". In: *Phys. Rev. C* 101 (5 May 2020), p. 052801. DOI: 10.1103/PhysRevC.101.052801. URL: https://link.aps.org/doi/10.1103/PhysRevC.101.052801.

[132] T. Dörfler et al. "Neutron-rich isotopes 54-57Ti". In: *Physical Review C - Nuclear Physics* 54.6 (1996), pp. 2894–2903. ISSN: 1089490X. DOI: 10.1103/PhysRevC.54.2894.

[133] P. H. Pile T. E. Ward and P. K Kuroda. "Decay of 54V". In: *Nuc phys A* 148.1 (1970), pp. 225–235.

[134] E. R. Flynn and J. W. Sunier. "States of 54V and 58Mn". In: *Phys Rev C* 15.3 (1977), pp. 879–882.

[135] A. M. Nathan et al. "Beta decay of 54-55V and the mass of 55V+". In: *Phys Rev C* 16.4 (1977), pp. 1566–1575. DOI: 10.1103/PhysRevC.16.1566. URL: https://link.aps.org/doi/10.1103/PhysRevC.16.1566.

[136] *Yield Station Fit Program for Beta decay spectra- mcsfit.* URL: http://isys02.triumf.ca:8080/yield/yield-station-1/software/yield-station-fit-program-for-beta-decay-spectra-mcsfit (visited on 02/10/2021).

[137] M.R. Bhat. *Evaluated Nuclear Structure Data File (ENSDF).* 1992.

[138] P. Sarriguren, A. Algora, and G. Kiss. "β-decay properties of neutron-rich Ca, Ti, and Cr isotopes". In: *Phys. Rev. C* 98 (2 Aug. 2018), p. 024311. DOI: 10.1103/PhysRevC.98.024311. URL: https://link.aps.org/doi/10.1103/PhysRevC.98.024311.

[139] E. Leistenschneider et al. "Precision Mass Measurements of Neutron-Rich Scandium Isotopes Refine the Evolution of $N = 32$ and $N = 34$ Shell Closures". In: *Phys. Rev. Lett.* 126 (4 Jan. 2021), p. 042501. DOI: 10.1103/PhysRevLett.126.042501. URL: https://link.aps.org/doi/10.1103/PhysRevLett.126.042501.

[140] J. Simonis et al. "Saturation with chiral interactions and consequences for finite nuclei". In: *Phys. Rev. C* 96 (1 July 2017), p. 014303. DOI: 10.1103/PhysRevC.96.014303. URL: https://link.aps.org/doi/10.1103/PhysRevC.96.014303.

[141] V. Somà et al. "Novel chiral Hamiltonian and observables in light and medium-mass nuclei". In: *Phys. Rev. C* 101 (1 Jan. 2020), p. 014318. DOI: 10.1103/PhysRevC.101.014318. URL: https://link.aps.org/doi/10.1103/PhysRevC.101.014318.

[142] A. Poves et al. "Shell model study of the isobaric chains A=50, A=51 and A=52". In: *Nuclear Physics A* 694.1 (2001), pp. 157–198. ISSN: 0375-9474. DOI: https://doi.org/10.1016/S0375-9474(01)00967-8. URL: https://www.sciencedirect.com/science/article/pii/S0375947401009678.